Physical Mechanisms of Cellular Injury in Electrical Trauma

by

Diane C. Gaylor

B.S.E.E. University of Arizona
(1984)
S.M.E.E. Massachusetts Institute of Technology
(1987)

Submitted to the Department of
Electrical Engineering and Computer Science
in Partial Fulfillment of the Requirements
for the Degree of

Doctor of Philosophy in Electrical Engineering

at the

Massachusetts Institute of Technology
September 1989

Signature of Author ______________________________
Department of Electrical Engineering
11 August 1989

Certified by ______________________________
Raphael C. Lee
Thesis Supervisor

Accepted by ______________________________
Arthur C. Smith
Chairman, Departmental Committee on Graduate Students

Physical Mechanisms of Cellular Injury in Electrical Trauma

by

Diane C. Gaylor

Submitted to the Department of Electrical Engineering and Computer Science
on 11 August 1989 in partial fulfillment of the requirements for the Degree of
Doctor of Philosophy in Electrical Engineering

ABSTRACT

Clinical evidence indicates that skeletal muscle cell membrane rupture occurs in electrical trauma. The pathogenic mechanisms of this damage have not been clearly identified. While it is clear that Joule heating causes part of the tissue destruction, particularly near the skin contact points, it does not appear to explain the pattern of tissue injury frequently observed at sites distant from the contacts.

In this thesis, the significance of the non-thermal mechanism of membrane electrical breakdown, often termed electroporation or electropermeabilization, is examined. The exposure thresholds for damage to skeletal muscle cells due to membrane electrical breakdown and to heating are determined experimentally. A cable model analysis is used to show that long skeletal muscle cells can experience transmembrane potentials large enough to cause membrane electrical breakdown in typical cases of electrical injury.

Experiments were performed using isolated cells harvested from the rat flexor digitorum brevis muscle. The transmembrane potentials induced in cells aligned parallel to a weak electric field were imaged using the membrane-incorporating potential-sensitive fluorescent dye di-4-ANEPPS. The cytomorphological responses to brief intense electric field pulses in the absence of significant heating and to elevated temperatures were monitored in separate experiments. Repeated application of electric field pulses of 50-300 V/cm magnitude and 0.1-4.0 msec duration caused irreversible contraction and eventual collapse of cells along their long axes, indicating alteration of the contractile proteins. Exposure to temperatures of 45°C and above also caused collapse of cells along their long axes.

To quantify changes in membrane permeability due to electrical and thermal stimuli, experiments were performed using cells loaded with the vital fluorescent dye carboxyfluorescein. To prevent contraction and collapse of the cells, they were bathed in hypertonic solutions of 3.0-times normal tonicity prepared with sucrose or mannitol. The fluorescence intensities of the cells were monitored during electrical and thermal exposures and changes in the cell membrane permeabilities were quantified using digital image processing techniques.

Experiments performed using di-4-ANEPPS demonstrated that the large transmembrane potentials induced in cells parallel to an applied electric field in isotonic solutions are nearly eliminated in cells bathed in hypertonic solutions. It was concluded that water loss from the cells in hypertonic solution causes the extensive internal membrane system to block the conduction path in places along the long axes of the cells. Thus, the transmembrane potential thresholds for electrical breakdown were obtained using cells aligned perpendicular to the field. Cells loaded with carboxyfluorescein were exposed to electric field pulses of 150-300 V/cm magnitude and 4 msec duration at room temperature. An increase in cell membrane permeability during and after the application of pulses of at least 200 V/cm was observed. This effect was quantified at field strengths of 250, 275, and 300 V/cm, which corresponded to induced maximum transmembrane potentials of 400-600 mV, a range consistent with other reported demonstrations of membrane electrical breakdown (Powell & Weaver, 1986; Zimmerman, 1986). At the high end of this range, the effect appeared to be at least partially reversed following the exposure. At the lower induced potentials, smaller permeability increases were observed which persisted over times as long as one hour. The cable model analysis predicts that transmembrane potentials in this range can be induced in isolated cells parallel to an applied field as weak as 10-25 V/cm, and in intact muscle in even weaker fields.

Cells loaded with carboxyfluorescein were elevated from room temperature to temperatures of 45, 50, 55 and 60°C. A delay preceded the onset of dye loss. Both the delay and rate of dye loss were temperature dependent. An Arrhenius relationship describes the membrane permeabilization with an activation energy of 58 kcal/mole, a value consistant with that describing other thermally-induced membrane alterations (Moussa et al., 1977).

By comparing the experimentally-determined damage thresholds to the electric field and temperature distribution in the human arm in a typical injury (Tropea, 1987), it was concluded that membrane electrical breakdown, along with Joule heating, is a mechanism of damage in many cases of electrical injury. The significance of the muscle damage caused by the two mechanisms depends on the strength and the duration of the electric fields in the tissues. Short duration contacts can result in membrane electrical breakdown in the absence of significant heating effects. For high field or long duration contacts, thermal damage can predominate, masking the occurrence of membrane electrical breakdown. The spatial arrangement of the tissues in the limb determines the induced electric field and Joule heating. Thus, it is expected that in a typical injury, tissues damaged by both mechanisms will be found scattered along the current path.

Thesis Supervisor: Raphael C. Lee, M.D., Sc.D.

Acknowledgements

It has been a great pleasure to work with and learn from Raphael Lee. The inspiration for this project was his, and he kept it going with dedication and enthusiasm. I greatly admire the many ways he has combined his medical and engineering talents in an effort to help victims of debilitating accidents.

I would like to thank James Melcher and Ernest Cravalho for their contributions to this thesis. Prof. Melcher introduced me to the world of continuum electromechanics. Prof. Cravalho generously provided me use of his laboratory for the thermal experiments. Their suggestions resulted in clear improvements to this document. Their encouragement is also appreciated.

The sponsors of the electrical burn project have done more than simply provide the funds for the work. Their interest and support have provided me many opportunities to meet and discuss my work with others in the engineering and medical communities. I gratefully acknowledge the support of The Boston Edison Company, Electric Power Research Institute, Empire State Electric Energy Research Corporation, EUA Service Corporation, Northeast Utilities Service Corporation, Pacific Gas & Electric Company, Pennsylvania Power & Light Company, The Public Service Company of Oklahoma, and the Public Service Electric and Gas Company. I would especially like to thank Derek Teare of the Energy Lab, who coordinated this project and helped out in so many ways.

I would like to thank the members of my exam committees, Abraham Bers, Robert Gallager, Roger Howe, Marcus Zahn, James Melcher, and William Peake. Their support allowed me to progress rapidly with my research and their encouragement is greatly appreciated.

Marilyn Pierce deserves many thanks for getting me out of so many scrapes. I'm not sure that I would have come this far without her help.

I cannot thank enough Mehmet Toner and Catherine Rocchio. The thermal experiments would not have been realized without them. Mehmet provided his laboratory set-up and an enormous amount of his own time and energy. Catherine's enthusiasm kept me going through many long days and nights of experiments and data reduction.

Several members of Raphael's research group contributed signficantly to this thesis. David Askey developed the image processing software that made the quantitative work in this thesis possible. He spent a considerable amount of time helping me to use and maintain the system, while trying to finish his own thesis. Deepak Bhatt spent a summer harvesting and shocking cells with me, and later moved on to other aspects of the electrical burn project. I learned a great amount from his work. Kwasi Prakah-Asante helped me to clarify my thoughts on the project during many long and illuminating discussions. Daniel Canaday designed and built the "Cell Killer" box used in the electrical experiments. David Israel developed many of the experimental protocols. Michelle Holguin kept me well-stocked with cells and also performed many

of the electrical experiments.

My office mates Philip von Guggenberg, David Lyon, and A.J. Morin were good company, and made the office fun. Philip, Ric Carreras, and Vanu Bose were always there when I needed help with the various computer systems and utilities. Vanu often provided a shoulder to cry on and a ride home late at night. The days Georgina Teare was in the office were a lot more fun than the days she wasn't.

The best part of the M.I.T. experience for me was the friends I made. They kept my spirits up and didn't forget me when I was working too hard to go out at night or away on the weekend. All the special times with Julio Escobar, Maurice Borgeaud, and Grace Chang will never be forgotten. The Ashdown 108 cooking group, led by Stephen Evangelides and including Julio, Maurice, and Jolene Kiolbassa, kept me well-fed and in high spirits following many hard days. Get-togethers with Mary Philips, Jim Smelt, and Karen Adler were always fun. Trips to Apo and Renan Sezginer's home in Connecticut came when I needed them most. Our annual Thanksgiving dinners together will remain one of my happiest M.I.T. memories. I can never thank all these people enough for all they have given me.

I thank my mother and father, who didn't get to see much of me during these past years, but who have always supported me in whatever I do.

My biggest thanks go to Julio Escobar. I would have never finished this thesis without his love and encouragement.

Contents

List of Figures

Chapter 1

Introduction

1.1 Background

Each year in this country several thousand victims are admitted to hospitals for treatment of electrical "burns". A significant number of these admissions are for severe injuries incurred by accidental contact with a high-voltage (greater than 1,000 volts) powerline. The typical victim is a young industrial worker or utility lineman. If a victim survives the initial cardiopulmonary insult, he then faces life-threatening sequelae from extensive skeletal muscle, neural and vascular tissue destruction far away from any obviously burned tissue. The massive muscle destruction releases proteins into the circulation which produce direct kidney damage, often leading to renal failure. Frequently, the victim will require multiple deep tissue debridements and sequentially higher level limb amputations, leading to permanent disability.

Clinical evidence suggests that skeletal muscle cell membrane rupture occurs in electrical trauma. This evidence includes the release of large quantities of myoglobin from the intracellular space (Baxter, 1970) and the elevated levels of arachidonic acid production, suggesting increased intracellular free calcium (Robson et al., 1984).

The pathogenic mechanisms of cell rupture following electrical injuries have not been clearly identified. Although Joule heating is commonly believed to mediate tissue injury, clinicians have observed substantial differences between the tissue response to thermal injury and electrical injury. While it is clear that Joule heating causes part of the tissue destruction, particularly near the skin contact points, it does not appear to explain the pattern of tissue injury frequently observed at sites distant from the contacts, which has been described as resembling a crush injury more than a thermal injury (Artz, 1974).

Long muscle and nerve cells are particularly susceptible to damage in an electrical injury, while adjacent small connective tissue cells can be relatively unharmed. Since the magnitude of Joule heating experienced is independent of cell size, it is unlikely that this mechanism of cellular injury is selective on the basis of cell size. However, for a given applied field, the magnitude of the induced transmembrane potential imposed by the field depends on the cell size and orientation in the field. Large elongated cells, oriented in the direction of the electric field, can experience transmembrane potentials large enough to lead to cell membrane rupture by electric breakdown (Gaylor et al., 1988, Lee & Kolodney, 1987), a process often termed electroporation (Powell & Weaver, 1986) or electropermeabilization (Zimmerman, 1986).

Cell membrane disruption by electrical stress is a well-documented phenomenon. Exposure of cells to brief intense electric field pulses has become a standard laboratory technique to produce cell fusion and to exchange genetic material between cells (Zimmerman, 1986). For artificial planar bilayer lipid membranes, rupture has been shown to occur when transmembrane potentials of 200–500 mV are applied for at least 100 microseconds (Benz et al., 1979; Abidor et al., 1979). A reversible electrical breakdown of both artificial and biological membranes has been shown to occur when transmembrane potentials exceeding 500 mV are applied for times on the order of nanoseconds to microseconds (Benz et al., 1979; Zimmerman et al., 1980; Zimmerman et al., 1981). Membrane electrical breakdown results in increased membrane permeability, which can lead to chemical imbalances in the cell. If not reversed, the effects can cause cell disfunction and death.

Cell membrane disruption can also be caused by exposure to supraphysiologic temperatures (Mixter et al., 1963; Moussa et al., 1977, 1979; Gershfeld & Murayama, 1988). The kinetics are temperature-dependent. At 45°C, hours are required to produce lysis of fibroblast and red blood cell membranes. However, only 100 seconds are required at 60°C. Other mechanisms of cellular damage caused by elevated temperatures include protein denaturation, enzyme inactivation, and membrane structural damage.

The kinetics of the two processes are quite different. Membrane rupture caused by temperatures of 45°C to 60°C occurs over minutes while rupture by electrical breakdown can occur in less than 100 microseconds. Thus, membrane electrical breakdown may occur long before Joule heating becomes significant. These separate processes may also act synergistically; heating appears to increase the probability of membrane electrical breakdown (Zimmerman, 1986).

1.2 Objectives

The principal objective of this thesis is to determine the primary mechanisms of muscle tissue destruction in major electrical injury. Toward this goal, the thresholds for damage of skeletal muscle cells from Joule heating and from membrane electrical breakdown will be quantified. The substantial evidence which suggests that the electrical effects are at least as important as the thermal effects has important clinical implications, since presently electrical injury cases are treated as burn injuries. It is hoped that this work will help improve treatment practices, resulting in fewer and less extensive limb amputations.

The remaining sections of this chapter describe the mechanisms of damage in an electrical injury, with emphasis on damage to the cell membrane. Of particular interest are the experimental demonstrations of membrane electrical breakdown and the theories and models that researchers have used to describe the phenomenon. Then, the current understanding of the electric field and temperature exposures experienced by tissues in an electrical injury will be discussed. Finally, the drop in the impedance of electrically damaged tissues that has been observed experimentally will be examined. Potentially, this indicator of damage could be exploited in the design of a device for locating damaged tissues hidden under healthy skin.

In Chapter 2, analytical models are developed which are used to predict the induced transmembrane potential in skeletal muscle cells in an applied electric field. Models for both isolated cells and cells in intact tissue are derived. These models were designed to illustrate the large potentials that can be induced in skeletal muscle cells due to their large size. The models have also provided insights into the distribution of damage in tissues following an electrical injury and have helped interpret the drop in muscle impedance which has been measured experimentally.

Because membrane disruption had not been studied in skeletal muscle cells, the exposure thresholds for damage due to pure electrical and thermal mechanisms for rat skeletal muscle cells were determined. These experimental studies are described in Chapters 3 and 4. Isolated cells harvested from the rat flexor digitorum brevis muscle were used in the experiments. The induced transmembrane potential in cells aligned parallel to a weak applied electric field was imaged using the membrane–incorporating potential–sensitive fluorescent dye di–4–ANEPPS. The cytomorphological responses to brief intense electric field pulses in the absence of significant heating and to elevated temperatures were observed in separate sets of experiments. To quantify changes in membrane permeability due to electrical and thermal stimuli, experiments were performed using cells loaded with the vital fluorescent dye carboxyfluorescein. In this way, the fluorescence intensity of a cell could be monitored during an exposure protocol and changes in the cell membrane permeability could be measured using digital image processing techniques. As will be seen in Chapter 4, these experiments resulted in the quantification of the cell membrane damage due to electrical and thermal stresses independently, the primary goal of this thesis.

In the final chapter, the experimentally–determined damage thresholds are compared to the electric field and temperature distributions in the human arm in typical cases of electrical injury. In this way, the significance of each mechanism is determined as a function of the induced electric fields in the tissues and the duration of the contact. As will be shown, the patterns of damage that occur in electrical injury can only be explained when both Joule heating and membrane electrical breakdown are considered.

1.3 Mechanisms of Cellular Damage in Electrical Trauma

1.3.1 Membrane Electrical Breakdown

Experimental Demonstrations

Two types of membrane breakdown due to applied electric fields have been experimentally demonstrated by others. A non–destructive reversible breakdown has been shown to occur in artificial planar bilayer lipid membranes (BLMs) and biological cells when transmembrane potentials exceeding 500 millivolts are applied for times on the order of nanoseconds to microseconds. (Benz et al., 1979; Zimmerman et al., 1980; Zimmerman et al., 1981). This type of breakdown manifests itself in a dramatic drop in the electrical resistance of the membrane, but the membrane survives. The value of the critical potential depends on the pulse width and the temperature. The breakdown phenomenon has been shown to occur in less than 10 nanoseconds (Benz & Zimmerman, 1980). It has been proposed that this process is analogous to dielectric breakdown in self–regenerating capacitors (Zimmerman et al., 1981).

Irreversible membrane breakdown (rupture) has been shown to occur in artificial planar BLMs when transmembrane potentials on the order of 200–500 millivolts are applied for times greater than about 100 microseconds. (Benz et al., 1979; Abidor et al., 1979). Thus, irreversible breakdown can occur at lower potentials than reversible breakdown, as long as much longer pulse widths are used. It has been proposed that this phenomenon is caused by pore formation in the membrane in response to the electric field (Abidor et al., 1979; Powell & Weaver, 1986).

Reversible and irreversible electrical breakdown were demonstrated by Benz et al. (1979) using artificial planar BLMs of oxidized cholesterol using a charge–pulse experimental technique, where a high voltage (a few hundred millivolts) was applied across a membrane in a few hundred nanoseconds. The discharge of membranes charged to voltages of 100–1200 mV is illustrated in Figure 1.1. Irreversible mechanical rupture was observed when a membrane was charged to voltages between 150 and 400 mV. In this case, the voltage decayed to zero over a few hundred microseconds. Reversible electrical breakdown was observed when the membrane was charged to voltages between 600 and 1200 mV. In this case, a decrease in the specific resistance of the membrane by 9 orders of magnitude occurred and the voltage decayed to zero over a couple of microseconds. It was not possible to charge the membrane higher than a critical voltage of about 1200 millivolts because the membrane started to discharge during the charging. At low voltages, the discharge was slow, and thus the membrane remained charged for a greater period of time than in the case of high voltage, where the reversible breakdown caused rapid discharge of the membrane. It is important to note that with membranes composed of other lipids, a mechanical rupture always followed the electrical breakdown; that is, reversible breakdown was not observed.

Benz and Zimmerman (1980) demonstrated that the critical voltage required for membrane electrical breakdown depends on the pulse width applied. This is illustrated in Figure 1.2. For both artificial BLMs and the giant algal cell *Valonia utricularis*, the critical voltage drops to about 500 mV as the pulse width increases beyond the microsecond range.

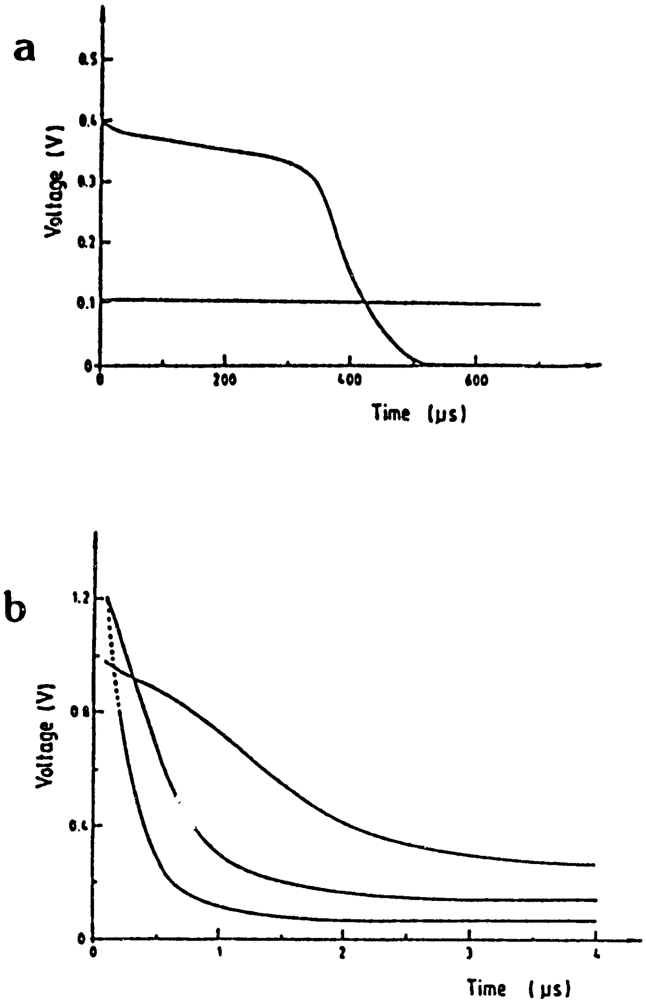

Figure 1.1: Reversible and irreversible electrical breakdown of artificial planar bilayer lipid membranes (taken from Zimmerman et al., 1981). In (a), a membrane charged to 100 mV in 500 nsec exhibits only a slow discharge, while a membrane charged to 400 mV suffers irreversible breakdown. In (b), membranes charged to over 800 mV exhibit the rapid discharge characteristic of reversible electrical breakdown.

The critical voltage required for membrane electrical breakdown is also strongly dependent on temperature. As illustrated in Figure 1.3 the critical voltage for both artificial BLMs and *Valonia utricularis* decreases with an increase in temperature. The data indicate that even with a pulse width on the order of a microsecond, the critical voltage drops to less than 1 volt at the physiologic temperature of 37°C.

Three effects of membrane electrical breakdown on biological cells have been described by Zimmerman et al. (1980). The first are the primary effects of the electric field on the membrane structure, leading to reversible or irreversible breakdown. Secondary effects result from the high current density in those membrane regions that have suffered electrical breakdown. These include heating and electrophoretic effects and may account for the irreversible breakdown observed when critical pulse widths and induced potentials for reversible breakdown are exceeded. Finally, there are the osmotic effects that result from the increased membrane permeability. These consequences of electrical breakdown have been examined experimentally using a variety of cell types.

Kinosita & Tsong (1977) exposed isotonic suspensions of human erythrocytes to single electric field pulses. An enhanced permeability state followed by hemolysis was observed at induced transmembrane potentials of about 1 volt or above applied for at least 20 μsec. The enhanced permeability of the pulse–treated erythrocytes to various substances was shown to decrease with increasing size of permeant molecule, reaching impermeability at a critical size. It was proposed that the applied electric field caused pores to form in the membrane which remained open after the removal of the field. The intracellular potassium therefore leaked out, and the extracellular sodium leaked in. To maintain osmotic balance, water entered with the sodium, and the cell swelled, leading to rupture and the release of hemoglobin. Based on the data, Kinosita and Tsong concluded that pores formed nearly instantaneously when the potential was above critical and that an increase in field intensity or pulse duration

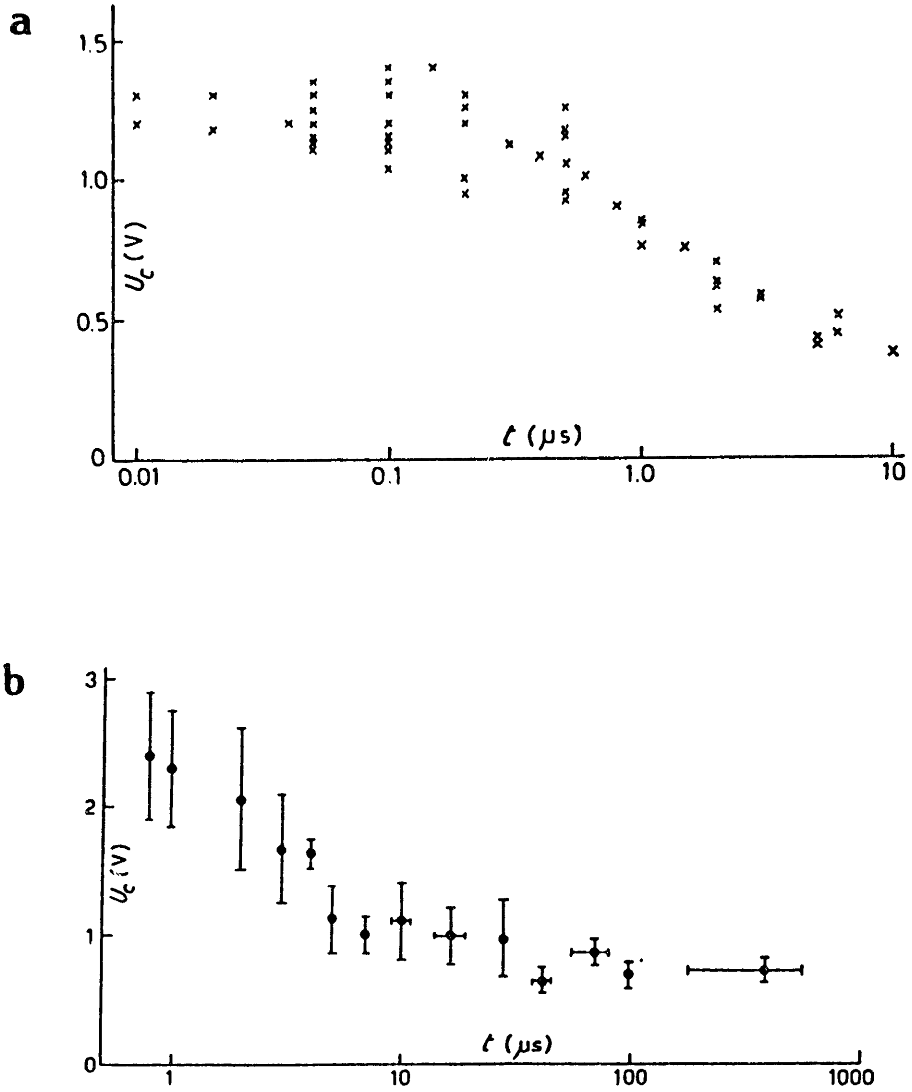

Figure 1.2: Membrane breakdown voltage U_c as a function of pulse width t for (a) artificial BLMs at 25°C (taken from Benz & Zimmerman, 1980) and for (b) the giant algal cell *Valonia utricularis* at 18°C (taken from Zimmerman & Benz, 1980).

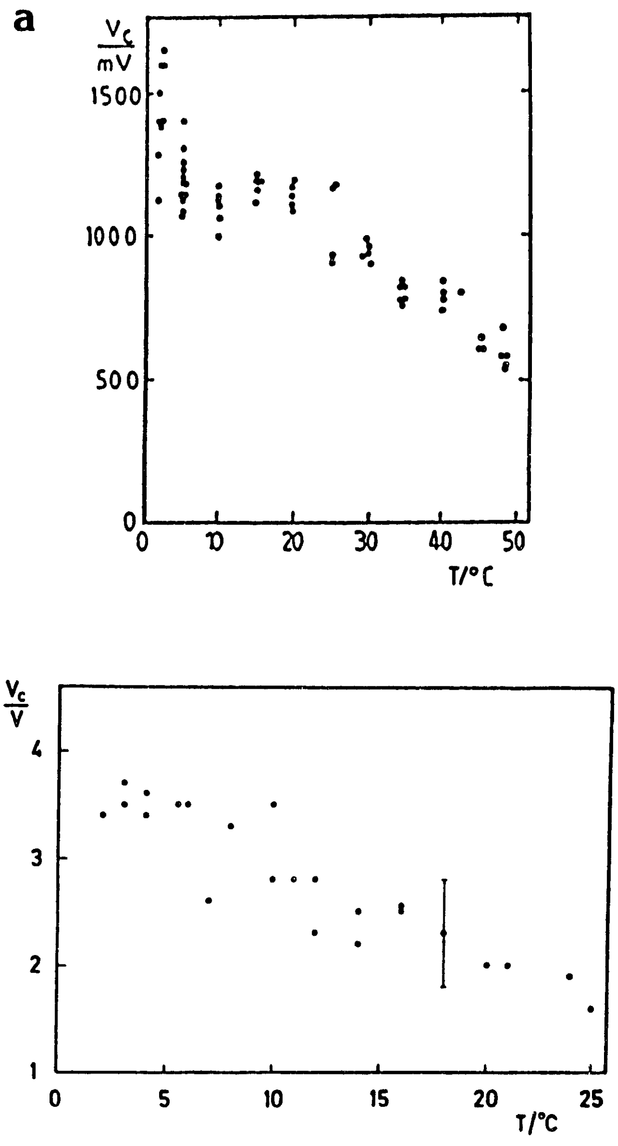

Figure 1.3: Membrane breakdown voltage V_c as a function of temperature T for (a) artificial BLMs with a pulse width of 0.4 μsec (taken from Zimmerman, 1986) and for (b) the giant algal cell *Valonia utricularis* with a pulse width of 1–2 μsec (taken from Zimmerman & Benz, 1980).

increased the rate of hemolysis, presumably by increasing the pore size. The induced transmembrane potential required for hemolysis is plotted as a function of field pulse duration in Figure 1.4.

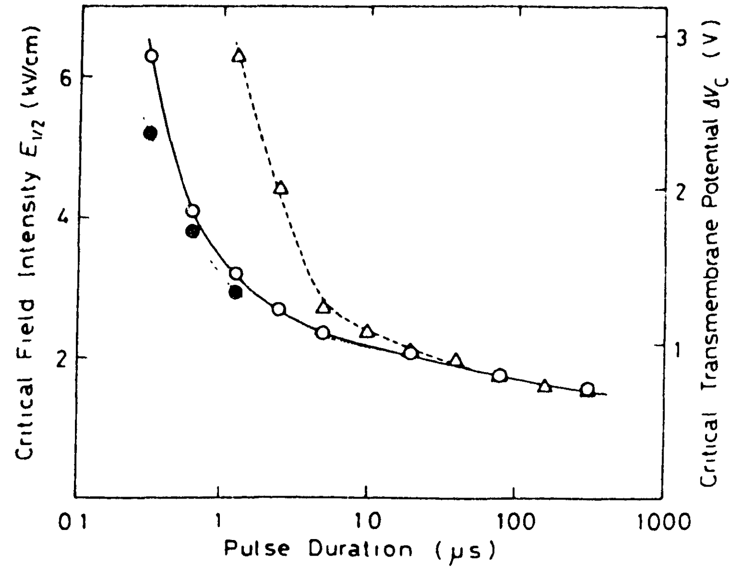

Figure 1.4: Induced transmembrane potential required for membrane electrical breakdown as a function of electric field pulse duration as determined by Kinosita and Tsong (1977). The critical field intensity is the applied field required for hemolysis of 50% of the cells and the critical transmembrane potential is the corresponding induced potential calculated by modelling the cells as oblate spheroids. Open triangles and circles refer to hemolysis and potassium release at room temperature respectively, while closed circles refer to potassium release at 4°C.

By performing their experiments in solutions of varying ionic strengths, Kinosita and Tsong were able to alter the current, and thus the heating, without changing the magnitude of the electric field. In this way, they were able to show that the cellular response correlated with the magnitude of the electric field and not with the temperature. Thus, they concluded that the increased permeability of the cell membrane and ensuing hemolysis were due to the effect of the electric field.

In a later paper, Teissie and Tsong (1980) proposed that transmembrane proteins in the erythrocyte membrane could be the site of voltage-induced pore formation. It had been shown previously (Kinosita and Tsong, 1977) that the pores could be very stable despite the rapid translational diffusion of lipid molecules in a bilayer. Teissie and Tsong showed that in low ionic medium, at least 35% of the pores was related to the opening of Na^+/K^+ ATPase channels. The increased membrane conductance induced by the applied electric field was partially blocked by the ATPase inhibitor ouabain.

Zimmerman et al. (1980) demonstrated a reversible increased membrane permeability state in mouse thymocytes when transmembrane potentials on the order of 1 volt were induced with a pulse width of 40 μsec at 4°C. The increased permeability was observed as a potassium and sodium exchange across the membrane. Electron micrographs of the permeabilized cells showed no morphological damage. However, when slightly higher potentials were induced, substantial membrane deformations were observed. When several volts were induced across the membrane using a pulse width of 0.5 μsec, uptake of eosin dye was observed, as illustrated in Figure 1.5. The resealing process was shown to be strongly temperature–dependent. The permeability increase persisted for up to an hour when the cells were kept at 4°C. When the temperature was raised to 37°, the cells resealed in a time on the order of seconds to minutes. However, even at 37°C, resealing occured much more slowly in the cell membranes than in artificial BLMs. It was proposed that this has to do with protein alterations and enzyme activity.

Theories and Models

Continuum Electromechanical Modelling of Biomembranes: The cell membrane has been conceptually viewed as a fluid mosaic (Singer & Nicholson, 1972), as illustrated in Figure 1.6. The mobility of the lipid molecules comprising the membrane is restricted to the plane of the membrane, leading to behavior as a two–dimensional fluid layer. The fluidity of the cell membrane is a key regulator of cell growth and vitality (Shinitzky, 1984). Experiments have indicated that membranes also exhibit

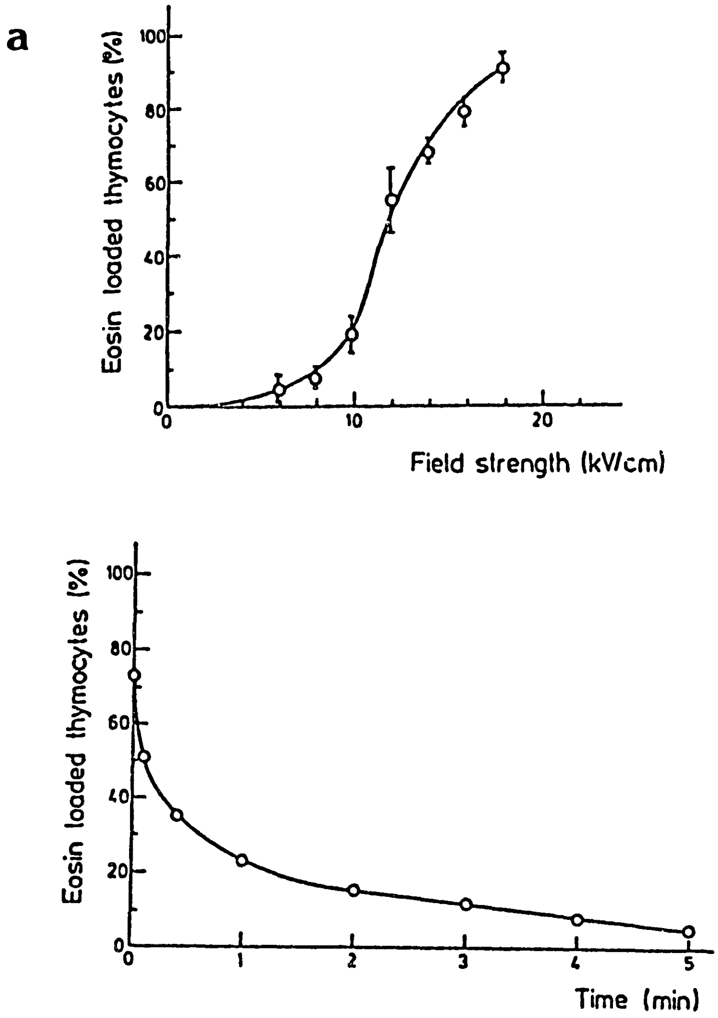

Figure 1.5: Reversible membrane electrical breakdown in mouse thymocytes. (a) Eosin uptake in thymocytes exposed to electric field pulses of 0.5 μsec at 4°C. An applied electric field strength of about 2 kV/cm corresponds to an induced transmembrane potential of about 1 volt for these cells. (b) Resealing of field-treated thymocytes after the temperature was elevated to 37°C as measured by the uptake of eosin. (Taken from Zimmerman et al., 1980).

the solid property of elasticity, attributed to the connections of proteins and other molecules associated with the membrane (Evans & Skalak, 1980).

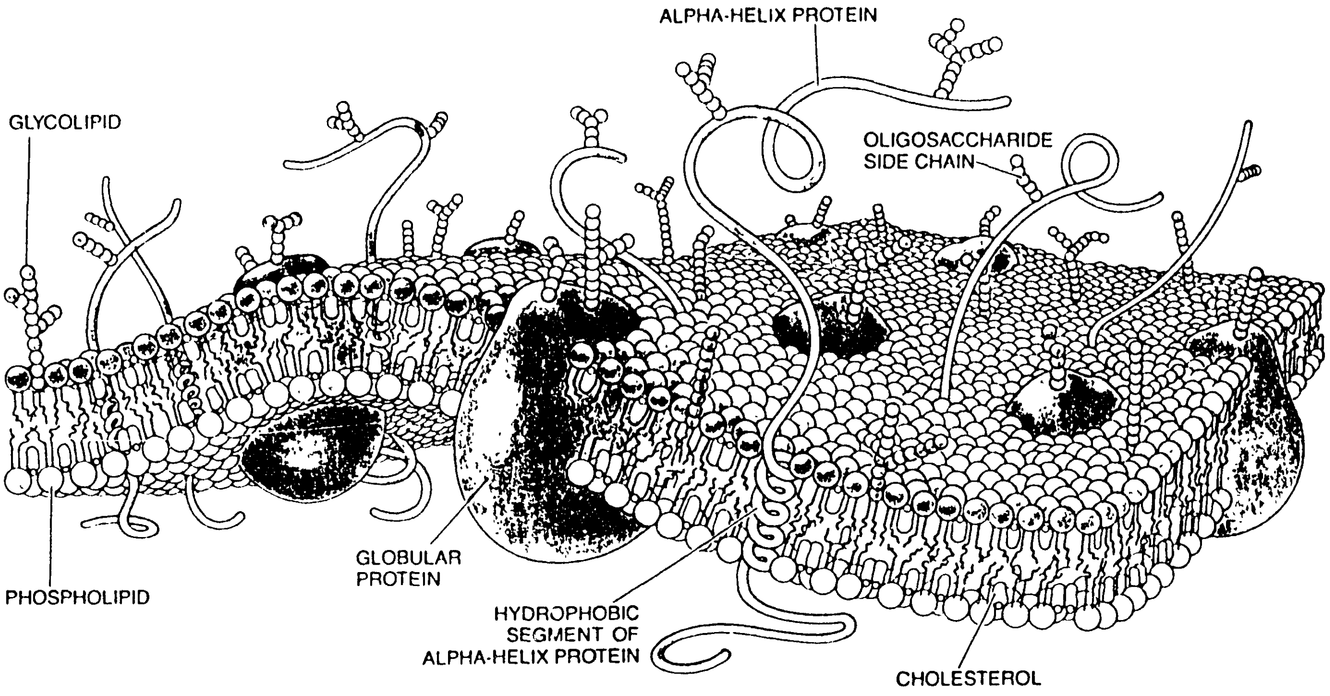

Figure 1.6: Fluid mosaic model of cell membranes, illustrating the fluid phospholipid bilayer and embedded proteins and cholesterol. (Taken from Bretscher, 1985.)

Ion fluxes across the ion–selective cell membrane lead to an electric field in the membrane. Most cell membranes at rest are predominantly permeable to potassium ions, making the inside of the membrane positive with repect to the outside. The transmembrane potential plays an important role in the regulation of many cellular processes.

Cell membranes have fixed surface charges, associated with certain phospholipids and proteins. These charges are usually negative and must be balanced by opposite charges in the aqueous phase adjacent to the membrane to preserve the electrical neutrality of the membrane system. This results in the formation of electrical double layers at each face of the membrane.

Many models of cell membranes describe the responses of membranes to electrical and mechanical stresses in terms of electromechanical parameters such as permittivity, viscosity, elasticity, and surface tension. By the use of properties usually ascribed to bulk fluids, the structure of the membrane is characterized as a continuum. This requires that the scale in space and time over which these properties are measured include a sufficient number of molecules such that fluctuations due to the behavior of individual molecules are small. For a biological membrane, the material can only be strictly considered as a continuum in the two dimensions of the membrane surface. In the third dimension of the thickness, the membrane exhibits molecular structure and discontinuity that preclude treatment as a continuous material in this direction. Thus, characterization of the electromechanical parameters is complicated by the microscopic, two-dimensional, anisotropic nature of the membrane. However, as will be seen, many electromechanical models of biomembranes successfully treat the membrane as a continuum in three dimensions in order to describe particular aspects of membrane behavior.

Electroporation: Many theories have been proposed regarding the mechanism by which cell membrane breakdown occurs. One of the most important proposes the mechanism of electroporation to explain electrical breakdown phenomenon. The theories of electroporation examine the mechanical, electrical, and chemical factors which cause pores in fluids and membranes (both artificial and biological) to form, and once formed, to expand or contract.

In a classic paper by Taylor and Michael (1973), it was suggested that axisymmetric holes in thin sheets of fluid where surface tension forces predominate will expand if their initial radii are larger than the thickness of the sheet, while holes with radii smaller than this thickness will close. This is due to the action of the interfacial tension, which acts to reduce surface area.

A similar approach was applied to bilayer lipid membranes by Weaver (Weaver & Mintzer, 1981; Powell & Weaver, 1986). His theory expands on the work of Litster (1975), who introduced the idea of the Brownian motion of molecules of the surrounding media causing pores to form in lipid bilayers, as illustrated in Figure 1.7. These pores are restrained by the mechanical forces at a pore's edge. The presence of a large population of small transient pores is consistent with the known electrical properties of membranes (Weaver et al., 1984).

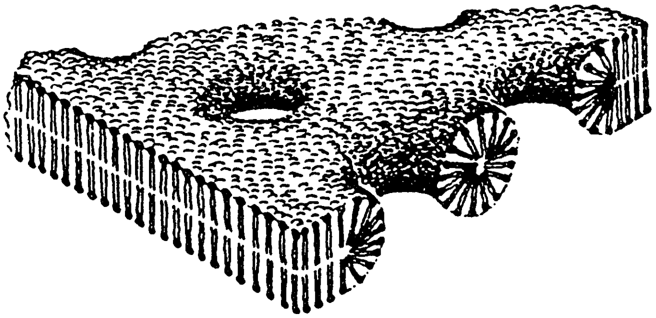

Figure 1.7: Hypothetical configuration of transient aqueous pores in a bilayer lipid membrane. (Taken from Weaver et al., 1984).

The energy ΔE needed to create a pore of radius r is the increase in energy associated with the creation of the edge of the pore less the energy of the eliminated surface area:

$$\Delta E = 2\pi\gamma r - \pi\Gamma r^2 \tag{1.1}$$

Γ is the bifacial energy per unit area of the membrane and γ is the strain energy per unit length of the membrane pore edge. Weaver added a term to this energy equation to include electrostatic energy effects which are associated with a transmembrane potential V_m:

$$\Delta E = 2\pi\gamma r - \pi r^2 \left(\gamma + \alpha V_m^2\right) \tag{1.2}$$

where α is a positive parameter dependent on the permittivities of the membrane and the intracellular and extracellular fluids and the membrane thickness δ_m. Thus, V_m tends to decrease the stability of the membrane against thermal fluctuations by decreasing the amount of energy required to form a pore. An applied V_m also lowers the critical pore radius beyond which mechanical forces at the pore's edge cannot restrain the pore from expanding until cell rupture.

Abidor et al. (1979) proposed that the formation of a pore is a two–step process where first a hydrophobic pore is formed which then can transform to a hydrophilic pore after surmounting a high energy barrier. This provides a second energy barrier between stability and rupture which could account for prolonged stressed states.

A statistical mechanical treatment of transient aqueous pores has been used by Weaver (Powell & Weaver, 1986) and Chizmadzhev et al. (1979) to describe a pore population as a function of applied transmembrane potential, which can be used to predict the conditions for reversible and irreversible breakdown. A stochastic model has also been developed (Sugar & Neumann, 1984). An enlarged pore population is expected to increase the conductivity of the cell membrane, thus lowering the transmembrane potential (Kinosita et al., 1988). Models of the conductance of pores (Levitt, 1985; Jordan, 1982), have been used in combination with models of electroporation to describe this phenomenon (Prakah–Asante, 1989).

Electrocompression: A mechanism for electrical breakdown of bilayer lipid membranes was proposed by Crowley (1973) in which rupture occurs as a consequence of electrostatic compression of the elastic membrane. The breakdown criterion derived seemed to furnish at least a rough estimate of measured breakdown voltages; however, it was later pointed out by Weaver & Minzter (1981) that with more accurate values for the mechanical properties of bilayers, the predicted breakdown voltage by Crowley's method becomes too high to explain the experimental results. Benz et al. (1979) discussed reversible electrical breakdown in terms of both membrane compression and ion movement through the membrane induced by the high electric field strength. It was proposed that thinning of the membrane by electric compressive forces leads to the energy of the ions reaching the Born energy required to cross the membrane.

Electromechanical Instabilities: Research on electromechanical instabilities in thin liquid films has led to biological membrane models. In one of the earliest relevant studies, Michael & O'Neill (1971) examined the stability of plane waves on a horizontal layer of insulating fluid bounded vertically by semi-infinite conducting fluids at different electrostatic potentials. It was shown that the marginal state between stable and unstable waves is a static one in which electrical and surface tensions are in balance at the interfaces.

Sanfeld et al. (1979) developed a hydrodynamic model describing interface surface motions induced by chemical, mechanical, and electrical stresses for interfaces between two bulk phases. Using linear stability analysis, the threshold conditions for the onset of longitudinal and transverse surface motion were studied for plane and spherical systems. New varieties of instabilities appeared due to the coupling between chemical, hydrodynamical, and electrical processes. The model was extended to include the finite thickness of biological membranes (Steinchen et al., 1982). The membrane was modelled as an incompressible, uncharged, isotropic, viscoelastic material sandwiched between identical Newtonian viscous fluids. The van der Waals attraction forces between the two faces of the membrane and Marangoni effects (lateral surface displacements) were taken into account. For the symmetric membrane system here, the two modes of wavy perturbations, the stretching modes and the squeezing modes, were uncoupled, and were used to explain cell deformation and membrane rupture, respectively.

Similar hydrodynamic models were developed by Maldarelli et al. (1980). Maldarelli and Jain (1982) modelled the membrane as a transversely isotropic, viscoelastic thin film. Nonionic and univalent ionic solutes were included in the system model; however, the membrane was considered to have no volume charge density. The membrane interfaces were considered tangentially immobile due to the presence of fixed surface charges on the membrane surfaces. Since cell membranes have been shown to highly resist compression, the membrane was constrained completely from changes in thickness. In this case, only the stretching modes of instability were exhibited. Using this model, Jain and Maldarelli (1983) were able to show the effects of induced transmembrane potential on the stability of a membrane as a function of other modelling parameters such as surface tension. Later Dimitrov (1984) used a simple viscoelastic model of a membrane to examine the dependence of breakdown potential on electric field pulse duration.

Dimitrov (1984) has proposed that the time course of electrical breakdown can be divided into three stages: (i) growth of membrane surface fluctuations, (ii) molecular rearrangements leading to membrane discontinuities, and (iii) expansion of pores, resulting in the mechanical breakdown of the membrane. The works of Jain, Maldarelli, and Dimitrov may help explain the first stage of this process, while the statistical models of Powell and Weaver (1986) and Chizmadzhev et al. (1979) and the stochastic model of Sugar and Neumann (1984) may help describe the last step. While various pictures of the molecular rearrangement involved in the second step have been suggested, this process has not been successfully modelled. It is thought to last on the order of nanoseconds.

1.3.2 Joule Heating

The changes induced thermally in a biological system depend on the duration of the exposure to an elevated temperature; that is, the process of damage is a rate process. Thus, thermal damage to cells and particularly to cell membranes can be modelled using a damage rate equation based on the concept of activation energy (Henriques, 1947). The activation energy E for a process is the critical amount of energy required in a system for the process to take place. Therefore, the rate of the process will be proportional to the fraction of the system constituents which have an energy at least equal to the activation energy. From the Maxwell-Boltzman energy distribution law, this fraction is $e^{-E/RT}$ where R is the gas constant and T is the temperature in degrees Kelvin. Thus, the rate of damage, denoted by an arbitray function Ω, can be written as an Arrhenius relation:

$$\frac{d\Omega}{dt} = P\, e^{-E/RT} . \tag{1.3}$$

The damage is completed when $\Omega = 1$. The Arrhenius relation can be used to predict the damage time t_d for arbitrary temperature elevations $T(t)$:

$$\int_0^{t_d} \frac{d\Omega}{dt} dt = \int_0^{t_d} F e^{-\frac{E}{RT(t)}} dt = 1 . \tag{1.4}$$

Many experimental studies have demonstrated that thermal damage accumulation in biological systems can be described by an Arrhenius equation. In one of the earliest studies, Moritz and Henriques (1947) performed experiments on pig skin by direct exposure of the surface of the skin to a rapidly flowing stream of hot liquid (water or oil) at temperatures ranging from 44°C to 100°C for durations of between 1 second and 7 hours. Exposures were designated as sub-threshold or supra-threshold based on whether they were sufficient or not to cause complete trans-epidermal necrosis. Similar exposures were made on human volunteers. The results indicated that there is little or no quantitative difference in the susceptibility of human and porcine skin to thermal injury, as illustrated in Figure 1.8. By fitting the experimental data to the Arrhenius equation, Henriques (1947) estimated the activation energy for damage to epithelium to be 150 kcal/mole. By comparing this value to the known activation energies of several biological processes, he concluded that the mechanism of damage was probably thermal alterations in proteins.

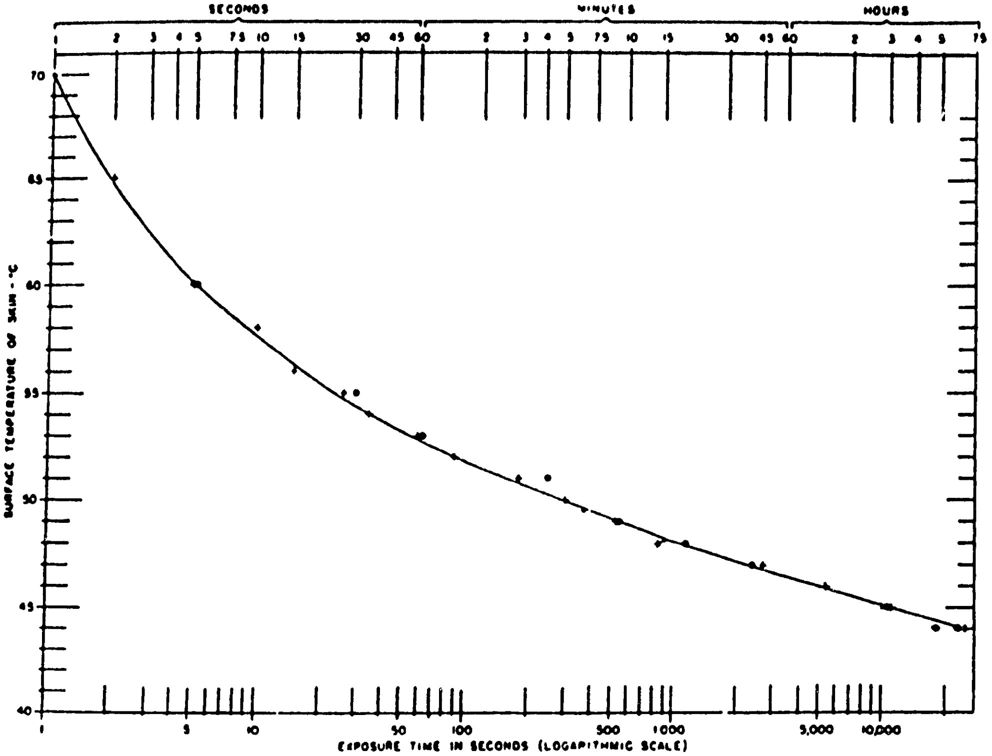

Figure 1.8: Time–temperature thresholds for epidermal necrosis (adapted from Moritz & Henriques, 1947). The crosses indicate the threshold at which necrosis of porcine skin occurs. The circles indicate the threshold for human skin.

Mixter et al. (1963) studied the effects of elevated temperature in the range of 45°C to 65°C on human fibroblasts. Cells bathed in a nutrient solution containing eosin Y stain were subjected to a prescribed temperature exposure. Since eosin Y stains necrotic cells, damage was quantified by a count of the stained cells. The time required for 50% cell death at a given temperature was fit to the Arrhenius equation, resulting in an activation energy for fibroblast necrosis of approximately 80 kcal/mole.

The effects of elevated temperature on human fibroblasts were studied again by

Moussa et al. (1977), this time using the appearance of irreversible morphological changes in the cells (blebs) as the indicator of damage. Using constant temperature protocols in the range of 44 to 68°C, the activation energy was determined to be 59.5 kcal/mole. For temperature protocols involving a linear rate of heating, it was shown that the damage time could be predicted using Equation 1.4. The results of Mixter and Moussa are compared in Figure 1.9.

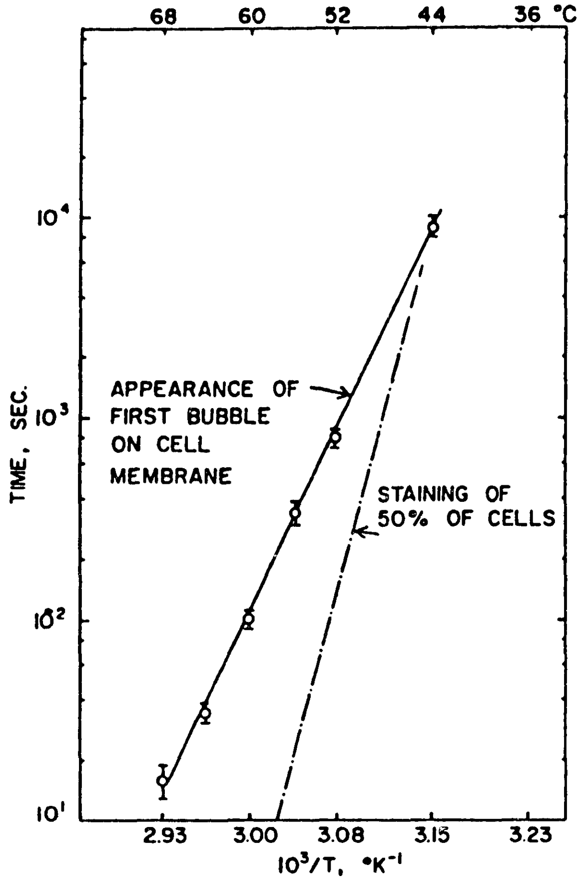

Figure 1.9: Time–temperature thresholds for damage to human fibroblasts (adapted from Moussa et al., 1977). Moussa et al. (1977) used the appearance of the first bubble on the cell membrane as the indicator of damage while Mixter et al. (1963) used staining of 50% of the cells with eosin Y, which stains necrotic cells.

More recent studies addressed the rate of hemolysis of red blood cells exposed to elevated temperatures. Moussa et al. (1979) performed experiments similar to the earlier fibroblast experiments using temperatures in the range of 44 to 60°C. Two models were used to examine the data. The first approach assumed that the damage kinetics involved two first-order processes, a reversible alteration and then irreversible damage. The first step was found to have an activation energy of 60 kcal/mole, and the second step of 31 kcal/mole. The second model was a statistical model where it was assumed that the number of cells damaged at any given time was normally distributed. The statistical model fit the data better, but the kinetic model provided more information about the damage process.

Gershfeld and Murayama (1988) have addressed the mechanism of hemolysis. Noting that hemolysis can occur at even slight temperature elevations above physiologic, as illustrated in Figure 1.10, they proposed that different mechanisms govern hemolysis at different temperatures since the processes commonly thought to be involved (denaturation of structural proteins and inactivation of enzymes, formation of lytic agents in plasma, and melting of membrane lipids) do not occur at low temperature elevations. Hemolysis occurring at temperatures below 45°C is proposed to occur due to a transformation of the membrane bilayer. Gershfeld (1968) has shown that membrane bilayer assembly occurs spontaneously only at a critical temperature, the growth temperature of the cell (in this case 37°C). The critical temperature is a function of the types of phospholipids forming the membrane and thus is different for membranes of different composition. At temperatures above the critical temperature, a certain amount of nonuniformity of the bilayer membrane is expected, including the formation of multibilayers. Assuming the size of a cell remains constant and that no lipid synthesis occurs, regions of the membrane will become deficient of lipids and become leaky. In the Gershfeld and Murayama study, hemolysis was studied for the temperature range of 4 to 50°C. At temperatures below 37°C, no significant hemolysis occurred. At temperatures above 45°C, hemolysis occurred with an activation energy of about 80 kcal/mole, which is consistent with activation energies for protein denaturation. At temperatures in the range of 38 to 45°C, hemolysis occurred with an activation energy of 29 kcal/mole, a value too low to be protein denaturation. However, this activation energy was shown analytically to be consistent with Gershfeld's theory of membrane transformation.

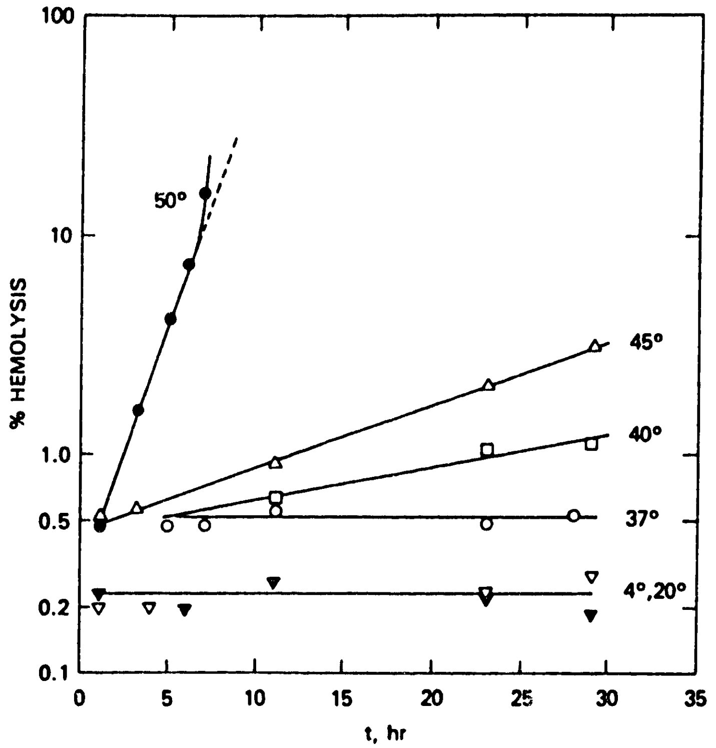

Figure 1.10: Hemolysis rate of human red blood cells as a function of temperature. (Taken from Gershfeld & Murayama, 1988.)

1.3.3 Mechanisms Particular to Skeletal Muscle Cells

Since skeletal muscle cells have been shown to be particularly susceptible to damage in electrical injury, this thesis focuses on the damaging effects of intense electric fields and elevated temperatures on skeletal muscle cells. Due to the complex physiology of skeletal muscle cells, there are many mechanisms of damage particular to this cell type.

Figure 1.11 illustrates the organization of skeletal muscle from the gross to the molecular level. Figure 1.12 shows the structure of the individual muscle cells. The skeletal muscle cell (fiber) is characterized by its long cylindrical shape and by the presence of numerous nuclei. The cells are grouped in parallel into fascicles, which associate in various patterns to form the whole muscle. The entire structure is invested by connective tissue. A capillary network surrounds each cell.

Each cell is enclosed in a membrane called the sarcolemma. The transverse striation, a characteristic feature of skeletal muscle cells, is not a property of the sarcolemma, but is due to the structure of the contractile mechanism of the cells, the myofibrils. The myofibrils are composed of two kinds of protein filament called actin and myosin. Each type of filament is organized in a cylindrical group, and groups of the two filaments alternate along the length of the cells. These filament groups have different refractility, leading to the appearance of the striations. Each unit of this repeating pattern is called a sarcomere. The cell contracts by a calcium–activated process of sliding filaments.

A continuous membrane system called the sarcoplasmic reticulum extends throughout the cytoplasm to form a network around each myofibril. At regular spacings, corresponding to the pattern of the sarcomeres, the sarcoplasmic reticulum forms a terminal cisternae which borders a transverse tubule (T tubule). This structure is illustrated in Figure 1.13. The purpose of this membrane network is to rapidly propogate an action potential received at the sarcolemma to all parts of the cell so that contraction of all myofibrils will be simultaneous. During rest, the sarcoplasmic reticulum accumulates calcium ions from the cytoplasm. When an action potential is propogated through the T tubules, this calcium is released back into the cytoplasm. In the presence of calcium, the actin and mysosin filaments slide against each other in the longitudinal direction, producing a contraction.

The complex physiology of skeletal muscle cells provides many mechanisms for damage. Their large size makes them more vulnerable to electroporation, since large transmembrane potentials can be induced. Increases in the permeability of the cell

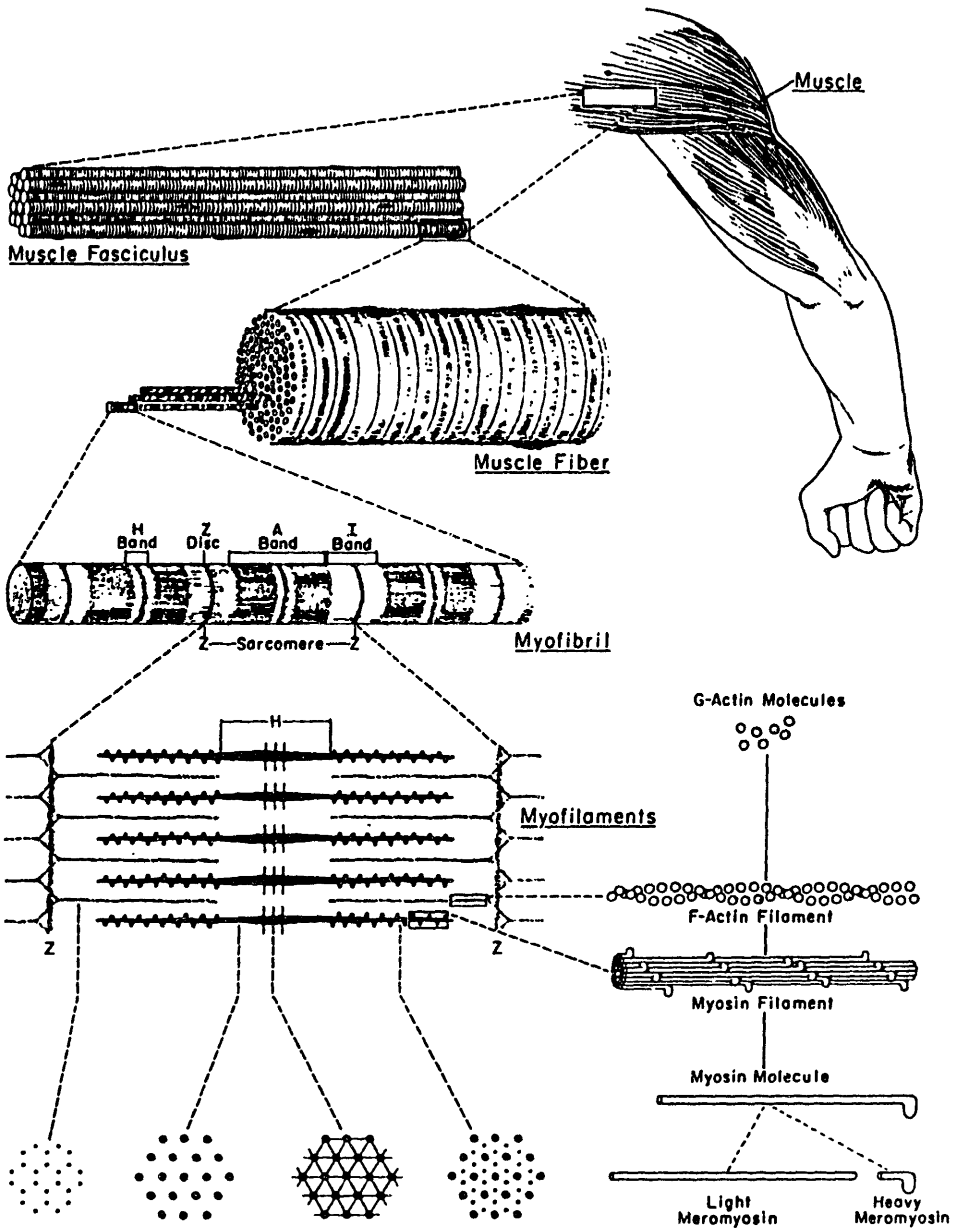

Figure 1.11: Organization of skeletal muscle from the gross to the molecular level. (Taken from Bloom & Fawcett, 1975.)

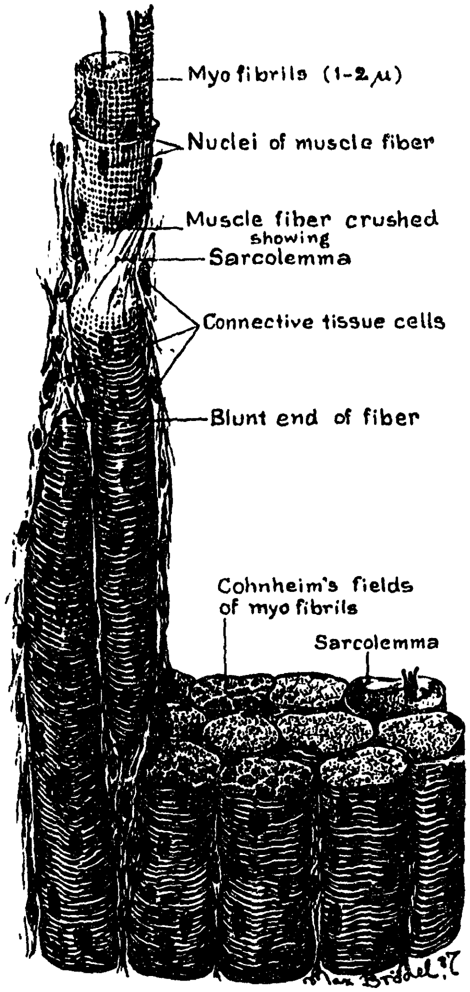

Figure 1.12: Structure of skeletal muscle. (Taken from Bloom & Fawcett, 1975.)

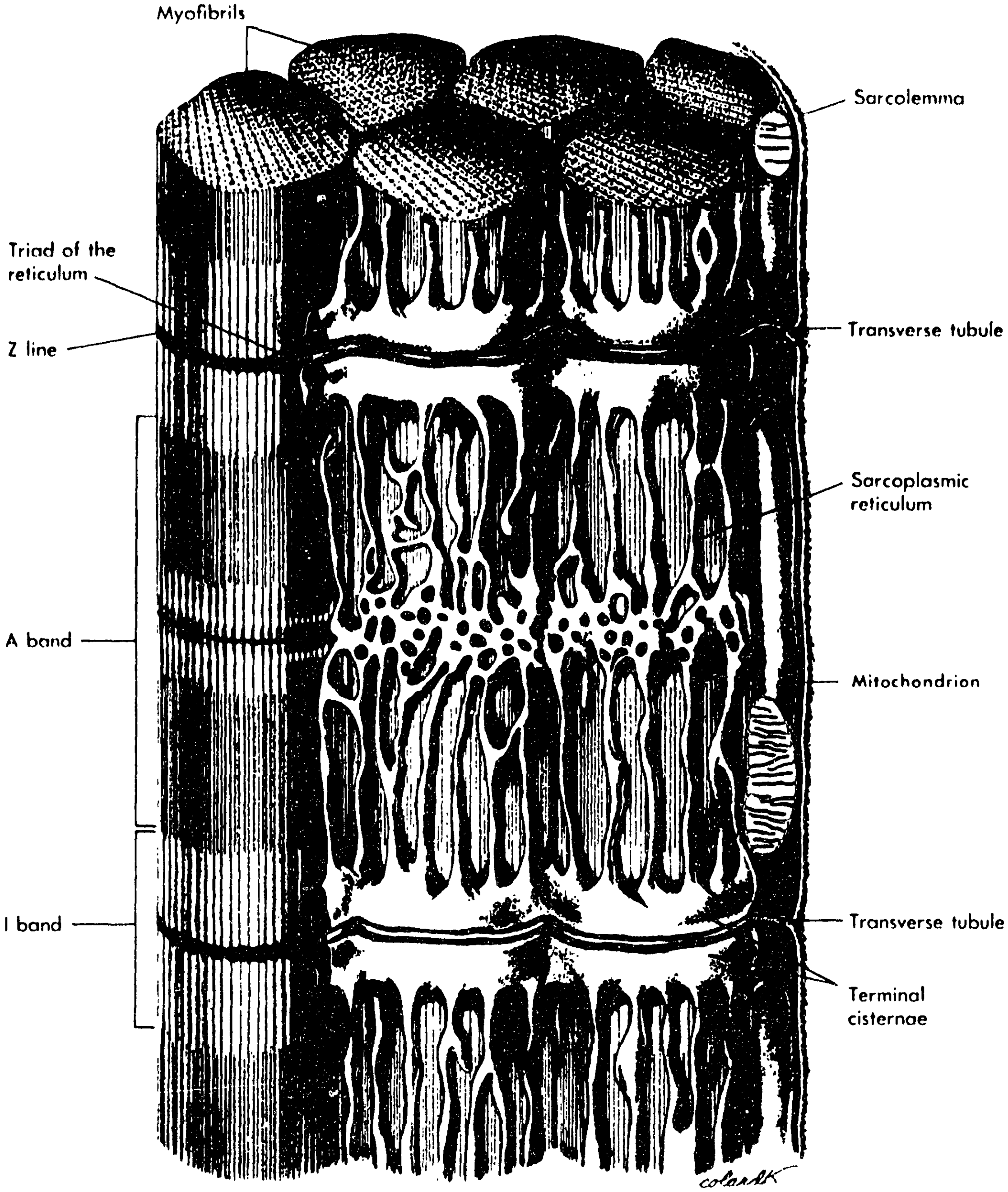

Figure 1.13: Distribution of the sarcoplasmic reticulum around the myofibrils of amphibian skeletal muscle. The location of the triads with respect to the bands varies from species to species. (Taken from Bloom & Fawcett, 1975.)

membrane or the sarcoplasmic reticulum to calcium ions lead to contraction, which is easily observed experimentally. In addition, any alteration in the actin–myosin complex, such as heat–induced denaturation of the proteins, leads to disfunction, although not necessarily membrane disruption. It is known that the actin–myosin complex is very sensitive to its ionic surroundings and that small changes can cause dissociation of the protein chains to a globular form (Laki, 1971; Tonomura, 1973; Lapanje, 1978).

1.4 Electrical and Thermal Exposures in Electrical Trauma

In order to weigh the relative importance of membrane electrical breakdown and Joule heating to the cellular damage occurring in electrical trauma, the magnitude and time–dependence of the electric field and temperature exposures must be known. Usually, only the voltage contacted by the victim is known accurately. Statistics from the Edison Electric Institute, illustrated in Figure 1.14, indicate that contacts in the range of 6000–10,000 volts are the most common cause of nonfatal injuries. The duration of the contact can usually only be guessed. The distribution of the electric field and the temperature attained in the affected tissues is too complicated to approximate even roughly. However, a small number of experimental and theoretical studies have been performed by others in an attempt to address these issues.

Relatively few experimental studies of electrical burn injury have been undertaken in the past. However, two research groups have presented data relevant to this thesis. The first group, from the Medical College of Wisconsin, performed experiments on hogs to determine the amount of current flowing in various tissues in a simulated electrical trauma (Scances et al., 1981, 1983). They determined that while the artery and nerve exhibit the largest current densities due to their high conductivity, it is the muscle that carries the highest percentage of current due to its large cross–sectional area. They also noted that bone passes the least amount of current due to its high

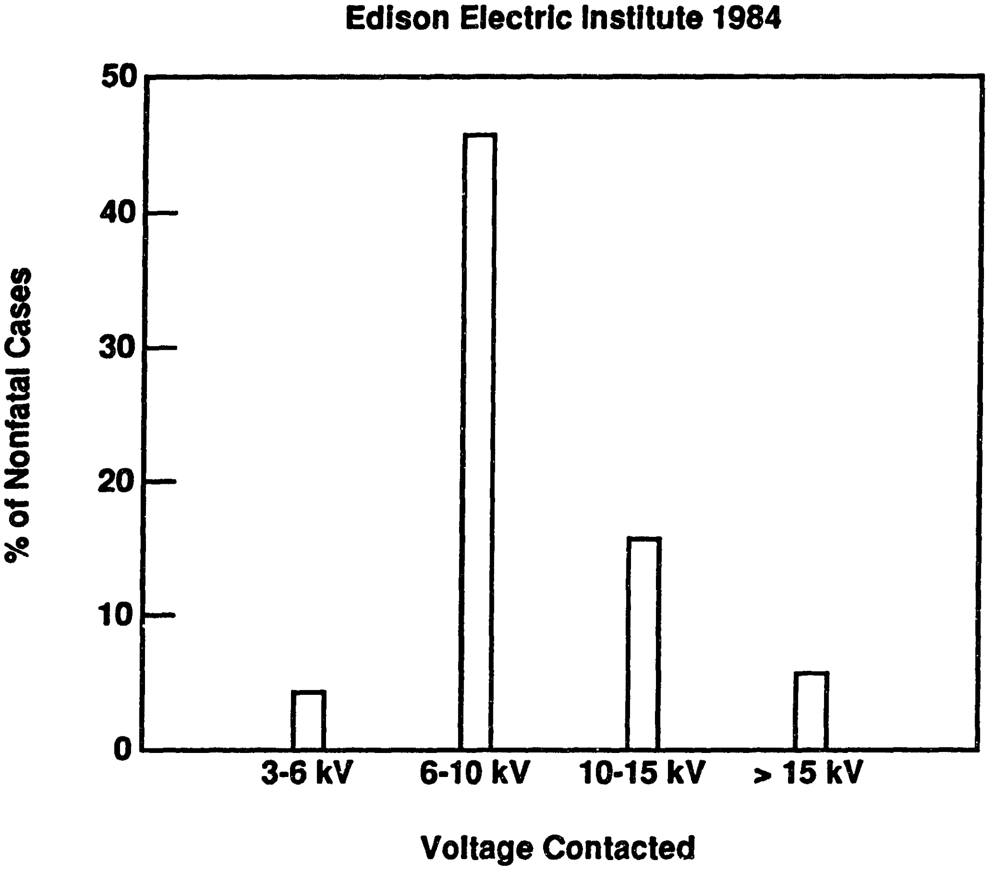

Figure 1.14: Voltages contacted in nonfatal electrical injuries. (Data provided by the Edison Electric Institute.)

resistivity.

A second research group, from the Microsurgical Research Laboratories of Royal Victoria Hospital in Montreal, developed a high-voltage electrical injury model using primates (Daniel et al., 1988; Zelt et al., 1986). A computer-controlled system applied a predetermined amount of energy hand-to-hand, and the temperature, current, and voltage drop were monitored at various locations throughout the arm. In agreement with Scances's results, this group of researchers found that the muscle carried the largest percentage of the current. However, they measured a significantly larger current in the bone than the Scances team. The highest temperatures were measured in the muscles of smallest cross-sectional area, and at the wrists and elbow, where highly-resistive bone predominates. Their data is well-summarized in Figure 1.15. Of particular note is Figure 1.15b, which provides the temperatures reached in various parts of the arm following injuries that would require amputation above and below the elbow. Also of interest was the observation (Zelt et al., 1986) of a "central core of damage" in the muscles, even though measured voltage drops varied little over the muscle cross-section (Daniel et al., 1988).

A three-dimensional finite element model of the human arm was developed by Tropea (1987,1989) to simulate the thermal response in an electrical trauma. The model included the geometries of the tissues (bone, muscle, fat, and skin), surrounding air convection, metabolism, Joule heating, and blood perfusion. Simulations were run for applied amperages of 5, 10, and 20 amps for durations of 0.2, 0.5, 1, and 5 seconds. These parameters were believed to cover the range of cases seen by clinicians. The thermal response of muscle, bone, fat, and skin in the mid-forearm to an exposure of 10 amps for 1 second is shown in Figure 1.16. As indicated, the muscle reaches the highest temperature. Thermal convection from the muscle to the other tissues leads to temperature increases in these tissues following the exposure.

The thermal response of muscle in the different regions of the arm to an exposure of

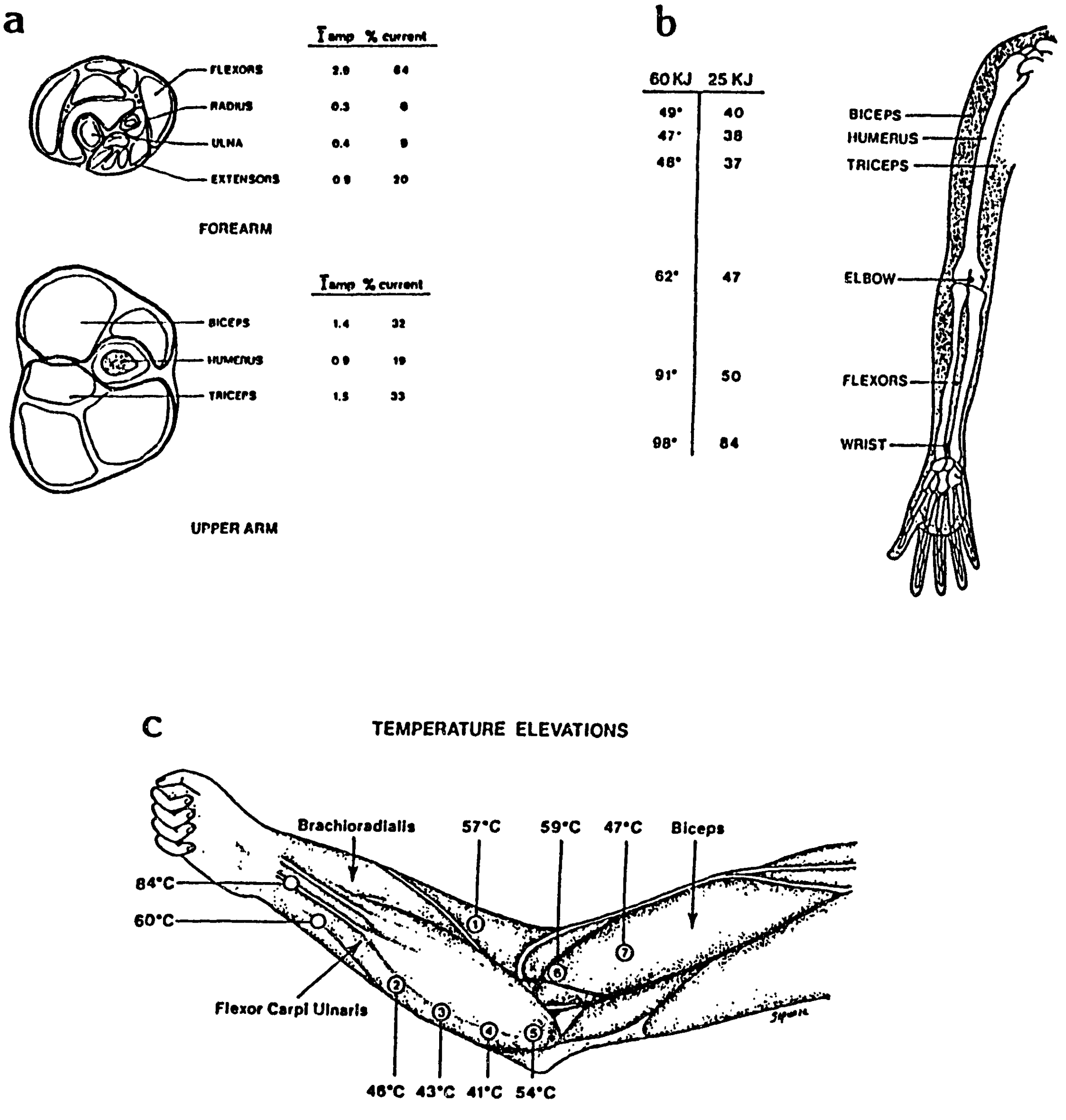

Figure 1.15: (a) Current distribution in the primate arm in trials of 40 kJ with total current passage of 4.5 A. (b) Peak temperatures in the primate arm in trials of 25 kJ and 60 kJ which produced injuries requiring amputation below and above the elbow respectively. (c) Temperature generated in the primate arm in trials of 40 KJ. (Taken from Daniel et al., 1988.)

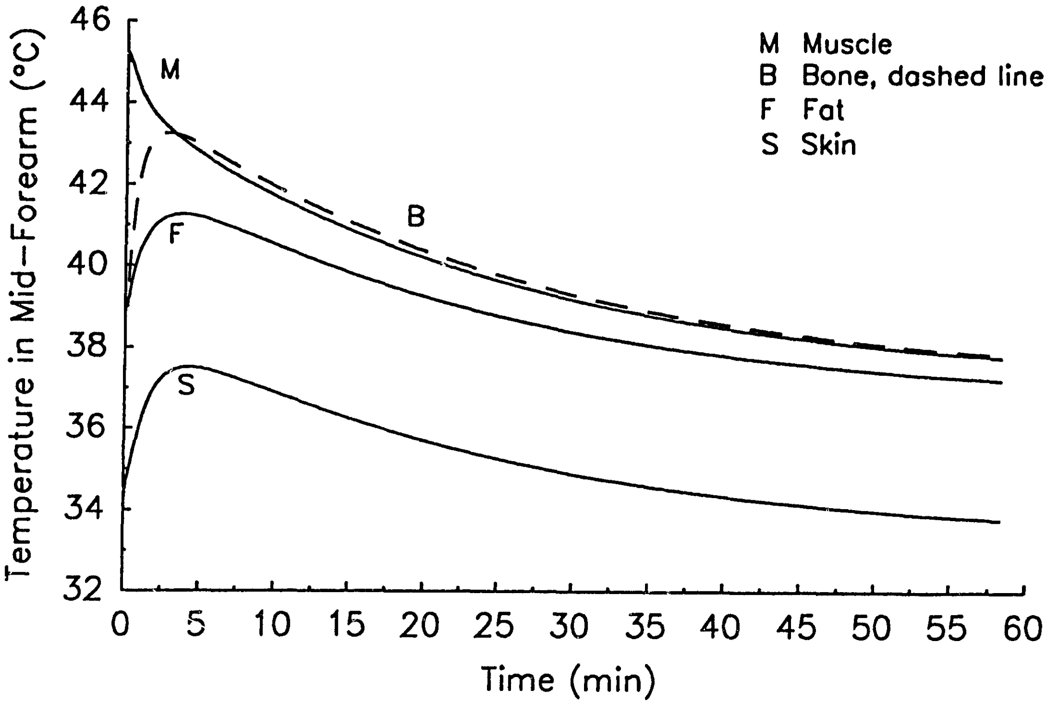

Figure 1.16: Thermal response of muscle, bone, fat, and skin in the human mid-forearm during an exposure of 10 amps for 1 second as predicted by the computer simulation of Tropea (1989).

10 amps for 1 second is shown in Figure 1.17. The temperature rise correlates roughly with the cross-sectional area of the arm in the region of interest. Thus, the distal forearm experiences the largest temperature due to its small cross-sectional area and large current density. The mid-arm experiences the smallest temperature increase. For the mid-forearm, the temperature rise for other exposures was calculated. The model predicted a temperature rise in the muscle of 2°C, 8°C, and 32°C for applied currents of 5, 10 and 20 A of 1 sec duration. For 10 A of current flow, the values for durations of 0.2 sec, 0.5 sec, and 5 sec were 1.7°C, 4°C, and 40.5°C, respectively. The cooling rates were shown to be highly dependent on the rate of blood perfusion.

Tropea determined the electric field distribution in the arm which occurs when a specified current flows through it. The cross-sectional areas and the distributions of the tissues within these cross-sections accounts for the variation in field strength along the arm. The predicted fields for an imposed current of 10 amps is illustrated in Figure 1.18. As shown, the electric field is highest in the distal forearm, which has a small cross-section, and in the elbow, where highly-resistive bone predominates.

1.5 Muscle Impedance Changes in Electrical Trauma

In a study by Chilbert et al. (1985), the relationship between tissue destruction and tissue resistivity was investigated. In these experiments, a current of 1 A at 60 Hz was passed between the hind legs of dogs until the temperature in the gracilis muscle reached 60°C. The time required for the temperature elevation was not reported. The changes in muscle resistivity correlated well with the severity of the damage inflicted by the applied current. Tissue exhibiting severe necrosis was shown to have a resistivity 70% lower than in controls. Tissue exhibiting minimal necrosis had a resistivity 20–40% lower than in controls. This study demonstrated that changes in resistivity can be used as an indicator of damage in electrical injury.

A more recent investigation by Bhatt et al. (1990) demonstrated that a drop in

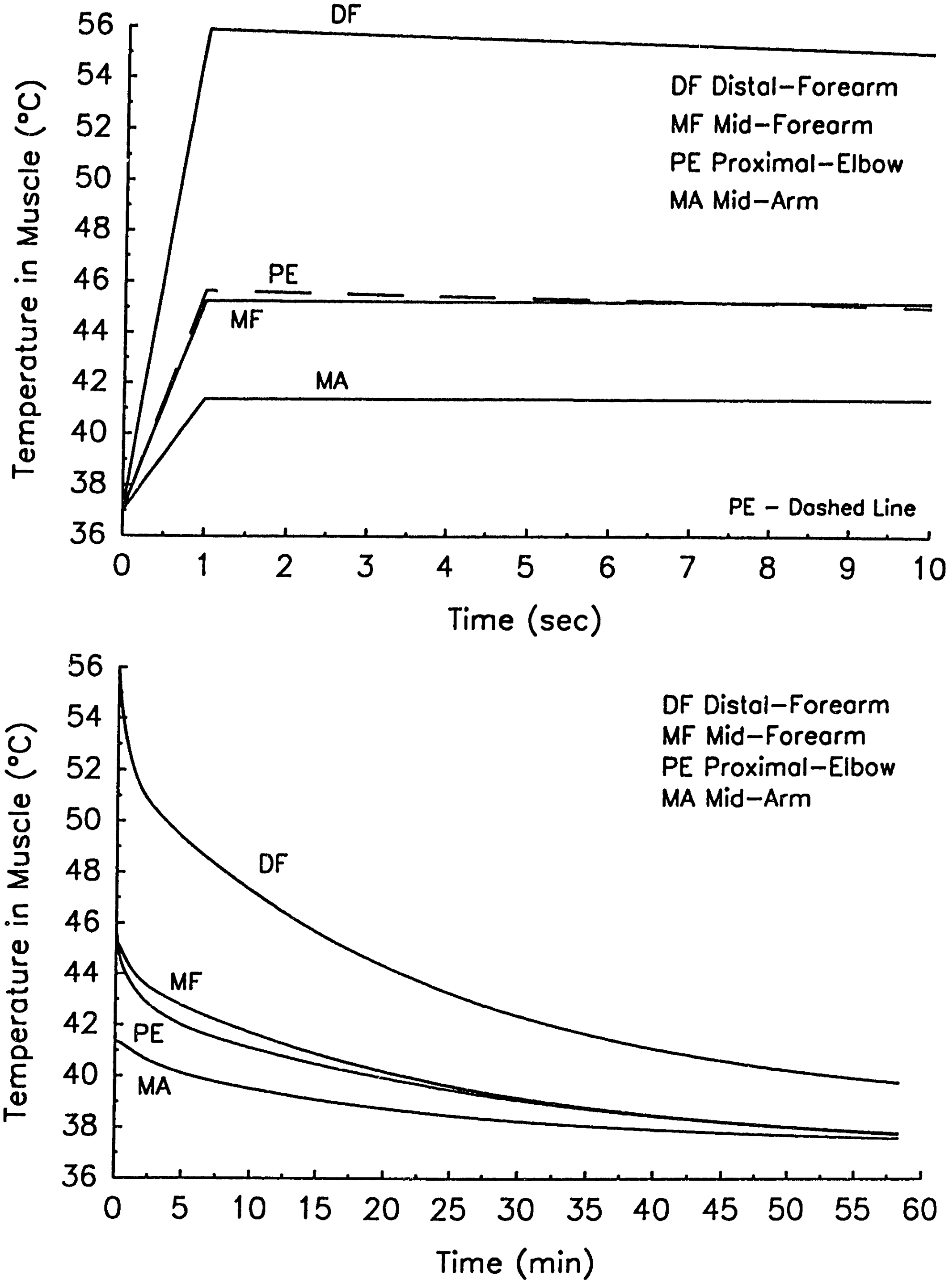

Figure 1.17: Thermal response of muscle regions in the human arm during an exposure of 10 amps for 1 second as predicted by the computer simulation of Tropea (1989).

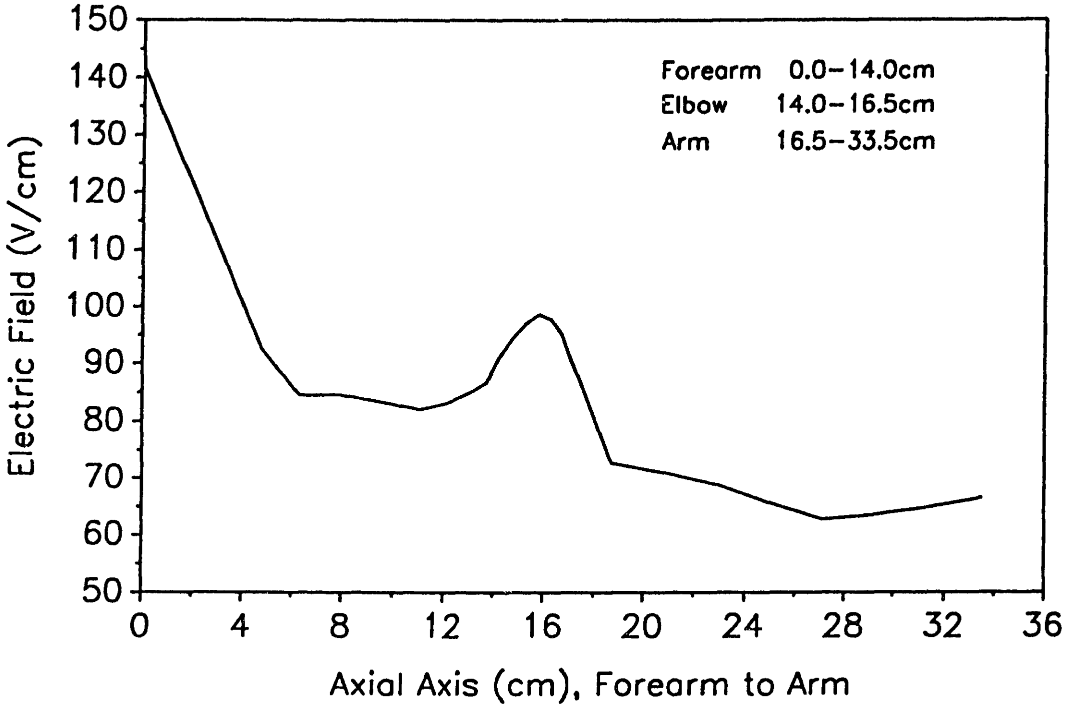

Figure 1.18: Electric field distribution in the human arm during a 10 amp exposure as predicted by the computer simulation of Tropea (1989).

impedance occurs when short-duration, high-intensity electric field pulses are applied to intact skeletal muscle explants in the absence of significant heating effects. In the experiments, the biceps femoris muscle was dissected from rats and trimmed to obtain a rectangular specimen. Impedance of the muscle explant was determined using a chamber designed for two-port impedance measurement at 10 Hz. For field exposure, the explants were transferred to a chamber filled with a physiologic saline solution. Electric field pulses were applied which ranged from 30 to 120 V/cm to cover the range of expected tissue exposure in electrical accidents. The pulses ranged in duration from 0.5 to 10.0 msec, short enough to prevent significant Joule heating. Pulses were always separated by 10 seconds to allow cooling. The impedance was measured within five minutes following the delivery of a total of 10, 30, and 60 pulses of a specified magnitude and duration. A decrease in impedance magnitude occurred following electric field pulses which exceeded threshold values of 60 V/cm in magnitude and 1.0 msec in duration. The field strength, pulse duration and number of pulses were all factors in determining the extent of the damage. The results are illustrated in Figure 1.19.

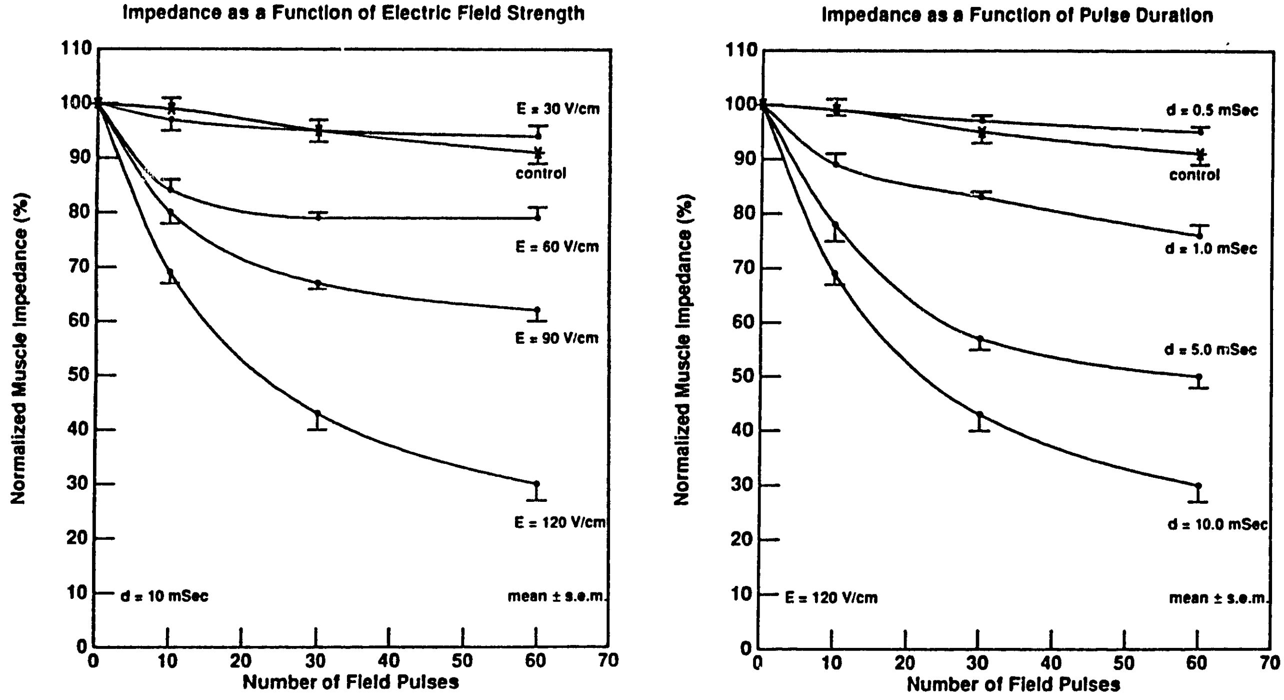

Impedance as a Function of Electric Field Strength

Impedance as a Function of Pulse Duration

Figure 1.19: Muscle impedance drop caused by exposure to short duration (*d*), high–intensity (*E*) electric field pulses. Pulses were separated by 10 seconds. Each point represents the mean and standard error of the mean for five muscle samples. (Taken from Bhatt et al., 1990.)

Chapter 2

Analytical Methods

2.1 Induced Transmembrane Potential

Major electrical trauma frequently involves the upper extremity, setting up current pathways as illustrated in Figure 2.1. In such instances, the long axes of most skeletal muscle cells are oriented roughly parallel to the direction of the electric field lines. Characteristically, at frequencies much less than 1 MHz, mammalian cell membranes are highly resistive compared with the intracellular and extracellular fluids. As a consequence, currents established by low-frequency fields in the extracellular space are shielded from the cytoplasm, leading to large induced transmembrane potentials. For a non-spherical cell in an electric field, the maximum induced transmembrane potential depends on the cell's orientation with respect to the electric field, reaching its greatest magnitude when the major axis of the cell is parallel to the average direction of the electric field. The case of cells parallel to the applied electric field is most relevant to the clinical problem, and will be treated first, using a cable model analysis. The case of cells perpendicular to the applied electric field is of interest in the interpretation of experimental results, and will also be discussed.

For both cases, a geometrically simple model of an elongated cell is analyzed. The cell membrane is modeled as a cylindrical boundary separating two electrical conductors, which represent the intracellular and extracellular fluids. The membrane

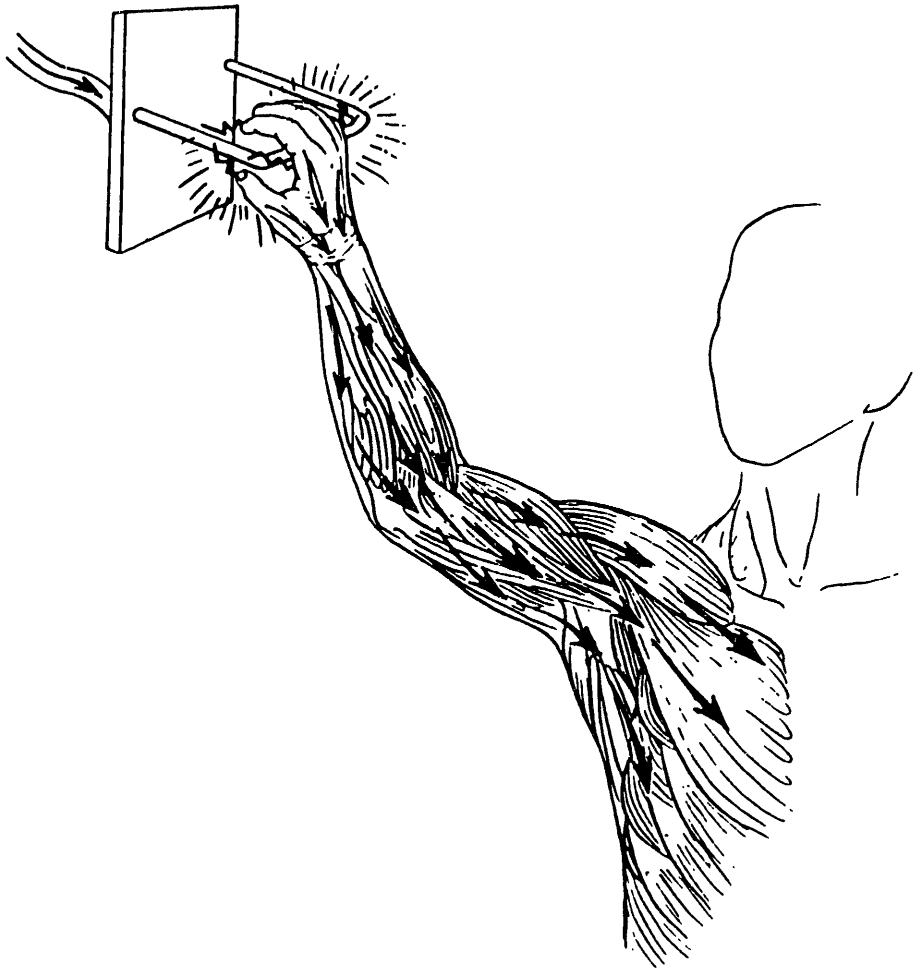

Figure 2.1: Illustration of the current path through the arm during a typical electrical accident. Electric field lines are generally near parallel to the major axis of the skeletal muscle cells.

and the intracellular and extracellular fluids are assumed to be homogeneous and isotropic, and to have electrical properties that are independent of the applied field until membrane breakdown.

2.1.1 Parallel Case – Cable Model Analysis

For the case of an elongated cell aligned parallel to an applied electric field, the traditional cable model approach is used. Electrical properties of the plasma membrane are represented by a series of parallel resistors and capacitors (Jack et al., 1975; Adrian, 1983), as illustrated in Figure 2.2. Longitudinal current in the membrane is ignored because the membrane has negligible cross-sectional area. This lumped-parameter circuit model of the membrane is combined with the specified resistivities of the intracellular and extracellular media to result in the well-known cable circuit representation. In the presence of an applied uniform field $E(t)$ in the $\hat{z}$ direction, a transmembrane potential will be superimposed over the natural resting potential across the membrane. Following the examples of Sten-Knudsen (1960), Ranck (1963), and Cooper (1984), the cable equations are used to solve for the spatial distribution of the induced transmembrane potential. Because human skeletal muscle cells may have significant cross-sectional areas, this application of the cable model necessitates the use of a boundary condition which accounts for the transmembrane current through the ends of the cell. The induced transmembrane potential distribution will be solved for isolated muscle cells and then for cells within intact tissue.

Analysis of the circuit model leads to a differential equation for the induced transmembrane potential $v_m(z,t)$:

$$\lambda_m^2 \frac{\partial^2 v_m(z,t)}{\partial z^2} = v_m(z,t) + \tau_m \frac{\partial v_m(z,t)}{\partial t} . \qquad (2.1)$$

The space constant λ_m and the time constant τ_m are given by

$$\lambda_m = \sqrt{\frac{1}{(r_i + r_o)g_m}} , \qquad \tau_m = \frac{c_m}{g_m} , \qquad (2.2)$$

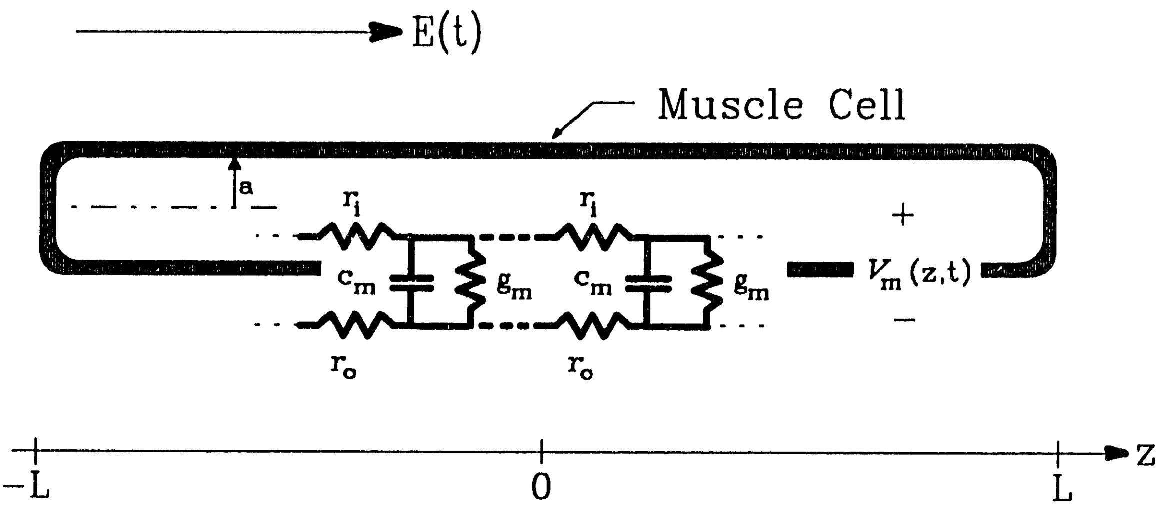

Figure 2.2: Cable circuit model of a skeletal muscle cell aligned parallel to an applied electric field $E(t)$. $V_m(z,t)$ is the induced transmembrane potential superimposed over the natural resting potential. Cell length is $2L$; cell radius is a.

where r_i and r_o are the resistivities (ohms/cm) of the intracellular and extracellular fluids respectively, and c_m and g_m are the capacitance per unit length (F/cm) and the conductance per unit length (mhos/cm) of the membrane respectively. For the case of a single cell in an infinitely extending bath of extracellular fluid, r_o is negligible compared to r_i since the extracellular space is much greater than the intracellular space. However, when the effects of neighboring cells are considered, this approximation is no longer valid.

Because powerline a.c. frequencies are of interest in this study, the problem will be solved for the sinusoidal steady state:

$$E(t) \;=\; \Re\{\, E_o\, e^{j\omega t}\,\} \tag{2.3}$$

and

$$v_m(z,t) \;=\; \Re\{\, V_m(z)\, e^{j\omega t}\,\}\;, \tag{2.4}$$

where V_m is a complex amplitude and E_o is assumed real. In this case, the differential equation simplifies to

$$\lambda_m'^{\,2} \frac{d^2V_m(z)}{dz^2} = V_m(z) , \tag{2.5}$$

where

$$\lambda_m'^{\,2} = \frac{\lambda_m^2}{1 + j\omega\tau_m} . \tag{2.6}$$

An appropriate solution is

$$V_m(z) = A \sinh(z/\lambda_m') , \tag{2.7}$$

where A is a constant to be determined from the boundary conditions. The boundary conditions constraining $V_m(z)$ can be determined from Kirchhoff's voltage law,

$$\frac{dV_m(z)}{dz} = -r_i I_i(z) + r_o I_o(z) , \tag{2.8}$$

where $I_i(z)$ is the complex amplitude of the total current in the $\hat{z}$ direction inside the cell $(i_i(z,t))$, and $I_o(z)$ is the complex amplitude of the total current in the $\hat{z}$ direction outside the cell $(i_o(z,t))$.

At the ends of the cell $(z = \pm L)$, charge conservation requires that the current through the membrane equal the current just inside the cell $(I_i(\pm L))$. If the admittance of the portion of the membrane which "caps" the end of the cell is denoted by

$$G_e' = (1 + j\omega\tau_e)G_e , \tag{2.9}$$

where G_e is the conductance of the membrane section (in mhos) and τ_e is the time constant reflecting the electrical properties at the ends of the cell,

$$I_i(\pm L) = \pm\, G_e'\, V_m(\pm L) . \tag{2.10}$$

It is assumed that the magnitude of the induced transmembrane potential is approximately constant over the entire ends of the cell at $|z| = L$. It is well known that the electrical properties near the ends of skeletal muscle cells can differ dramatically from the rest of the cell (Milton et al., 1985). This is generally attributed to the extensive membrane folds and invaginations which usually occur at the ends, and not to differences in the membrane electrical properties. Thus, it can be assumed that $\tau_e = \tau_m$, but it cannot be assumed that $G_e = \pi a^2 g_m$. Unfortunately, this difference has not been well-characterized for most species.

Isolated Cell Model

For the isolated cell case, it is assumed that $I_o(z)$ is much greater than $I_i(z)$ because the extracellular space is much larger than the intracellular space. Therefore, the product $r_o I_o(z)$ can be assumed to be approximately constant, leading to the condition

$$r_o I_o(z) \approx E_o \, . \tag{2.11}$$

The constant A can be determined by substituting the boundary conditions 2.10 and 2.11 into Equation 2.8, and evaluating at $z = L$. Thus,

$$V_m(z) = \frac{\lambda'_m E_o}{\cosh(L/\lambda'_m)} \frac{\sinh(z/\lambda'_m)}{1 + \lambda'_m r_i G'_e \tanh(L/\lambda'_m)} \, . \tag{2.12}$$

With the exception of the term which takes into account the end boundary condition, the form of the solution is consistent with Cooper (1984). In the limit that $L >> \lambda_m$, the end condition of Equation 2.10 is insignificant and Equation 2.12 gives the same prediction as Cooper. However, when $L << \lambda_m$, the end condition is significant. In this limit, the current entering the cytoplasm originates mostly at the end of the cell, with negligible current entering through the sides. Thus, the transmembrane potential changes linearly along the length of the cell. This behavior can be readily appreciated from Equation 2.12 by analysis of the $L << \lambda_m$ case in the d.c. limit. This predicts

$$V_m(z) \approx \frac{R_m}{R_i + 2R_m} 2 \, E_o \, z \qquad \text{for} \qquad L/\lambda_m << 1 \, , \tag{2.13}$$

where $R_m = 1/G_e$ is the resistance of each of the endcaps of the cell and $R_i = 2Lr_i$ is the resistance of the cytoplasm inside the cell. For $z = L$, $V_m(L)$ is expressed as a fraction of the total voltage across the cell ($2LE_o$) determined by the voltage divider $R_m/(R_i + 2R_m)$.

Tissue Model

For cells within intact tissue subjected to an electric field, the previous analysis can be modified to include the effects of neighboring cells on the induced transmembrane potential. The cells are assumed to be ordered parallel to each other in a hexagonal array as illustrated in Figure 2.3. To facilitate the comparison of induced transmembrane potential in tissue with the case of isolated cells, the quantity $V_c/2L$ is used as the "source" term, where V_c is the voltage drop across the full length of a cell. For the isolated cell case, $V_c/2L$ is equal to the applied field amplitude E_o.

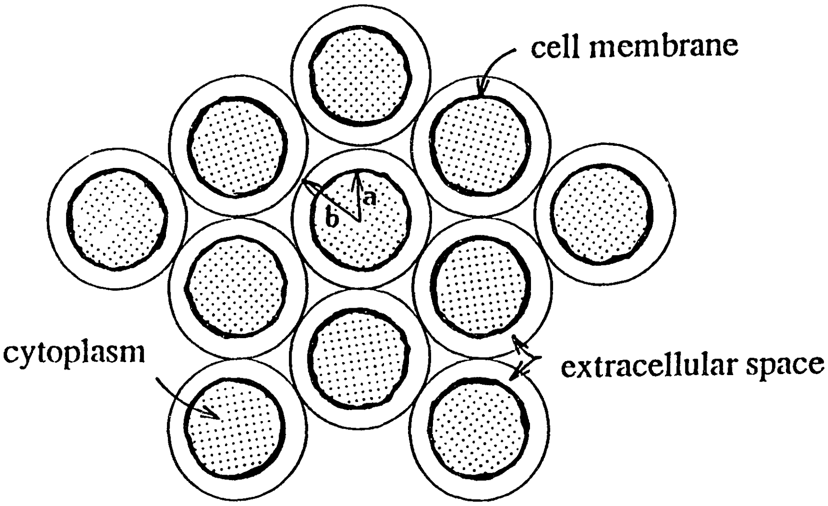

Figure 2.3: Hexagonal array representation of parallel skeletal muscle cells. Cell radius is a; extracellular fluid radius is b.

In this tissue model, each cell is surrounded by a volume of extracellular fluid. By symmetry no current crosses the boundry into the adjacent extracellular region. This conveniently isolates each cell from its neighbors for the purposes of the analysis. Here, the boundaries are approximated by cylinders of radius b as indicated in Figure 2.3 The total current I_T within each cell's region, consists of the intracellular current $I_i(z)$ and the extracellular current $I_o(z)$:

$$I_T = I_i(z) + I_o(z) . \tag{2.14}$$

The cross–sectional area of extracellular space will determine the extracellular resistivity r_o. Generally, for cells that are not on the muscle surface, r_o is not negligible compared to r_i and significantly affects the value of the space constant in Equation 2.2. In addition, the extracellular electric field amplitude between muscle cells is not constant in z. Therefore, the approximation of Equation 2.11 is no longer valid.

The solution form of Equation 2.7 is unchanged but retains a modified coefficient A' to be determined. Kirchhoff's law, Equation 2.8, provides

$$I_T = I_i(z=0)\left(1 + \frac{r_i}{r_o}\right)\frac{A'}{r_o\lambda'_m} . \tag{2.15}$$

By symmetry, the current inside a cell at $z = 0$ must be the sum of the current entering from the end (I_e) and from the sides (I_s). I_e is simply $I_i(-L)$, as expressed in Equation 2.10. I_s can be found by

$$I_s = g_m(1 + j\omega\tau_m)\int_{-L}^{0} -V_m(z)dz = \lambda'_m A' g_m(1 + j\omega\tau_m)[\cosh(L/\lambda'_m) - 1] . \tag{2.16}$$

Equations 2.14 thru 2.16 can be solved for the constant A'. Knowing A', the total currents inside $(I_i(z))$ and outside $(I_o(z))$ the cell can be derived. Integrating either $r_iI_i(z)$ or $r_oI_o(z)$ over the total length of the cell leads to V_c in terms of I_T. Thus,

$$V_m(z) = \frac{V_c}{2L}\,\frac{\lambda'_m\,(r_o + r_i)/r_i}{\cosh(L/\lambda'_m)}\,\frac{\sinh(z/\lambda'_m)}{1 + \lambda'_m\,(\,(r_i + r_o)G'_e + r_o/(Lr_i))\tanh(L/\lambda'_m)} . \tag{2.17}$$

Analysis

Using the above results, the variation in induced transmembrane potential with cell dimensions and intracellular spacing can be determined. Typical values for the electrical properties of human skeletal muscle cells are used: $C_m \approx$ 3–6 μF/cm^2 and $G_m \approx 1.0$–2.5×10^{-4} mhos/cm^2 (Schanne & Ruiz P.–Ceretti, 1978). From these values, $g_m = 2\pi a G_m$, $c_m = 2\pi a C_m$, and $\tau_m = C_m/G_m$ are easily determined. $r_i = (1/\pi a^2 \sigma_i)$ is determined from the intracellular fluid conductivity, $\sigma_i \approx .01$ mhos/cm. Since the electrical properties of the ends of human skeletal muscle cells have not been characterized in the literature, it will be assumed that the membrane properties are uniform over the entire cell, and thus $G_e = \pi a^2 G_m$ and $\tau_e = \tau_m$.

Using average values for human skeletal muscle cells, $\omega\tau_m = \omega C_m/G_m$ is > 1 for frequencies greater than approximately 10 Hz. Thus, in the sinusoidal steady state at standard commerical power frequencies (50–60 Hz), $\omega\tau_m$ cannot be neglected and the induced transmembrane potential remains a complex quantity. The magnitude of the induced transmembrane potential $V_m(z)$ at 60 Hz was calculated from Equation 2.12 for isolated skeletal muscle cells of several arbitrary lengths with a constant radius 100 μm, corresponding to a space constant λ_m on the order of 0.5 cm. The results are plotted in Figure 2.4(a) for cells of length 0.2 λ_m, 0.6 λ_m, λ_m, and in Figure 2.4(b) for cells of length 1.0 λ_m, 2.0 λ_m, 3.0 λ_m, 4.0 λ_m, 6.0 λ_m, and 8.0 λ_m.

For cells that are short compared to their space constant, the induced transmembrane potential varies linearly with z, is constrained by symmetry to be zero at the origin, and reaches a maximum at the cell ends. For longer cells, the transmembrane potential has a more exponential dependence. Thus, the imposed transmembrane current is disproportionately concentrated toward the ends. The extent to which cell structure leads to intramembrane field intensification can be appreciated from Equation 2.12. If the cell membrane conductivity were equal to that of the cytoplasm or extracellular fluid, then $|V_m(\pm L)|$ would equal $E_o\delta_m$. If the cell membrane were perfectly insulating, $|V_m(\pm L)|$ would equal E_oL. For muscle cells with characteristic membrane properties which are short enough that the resistance of the membrane is infinite compared with the cytoplasm, $|V_m(\pm L)|$ is equal to E_oL. For longer cells, the

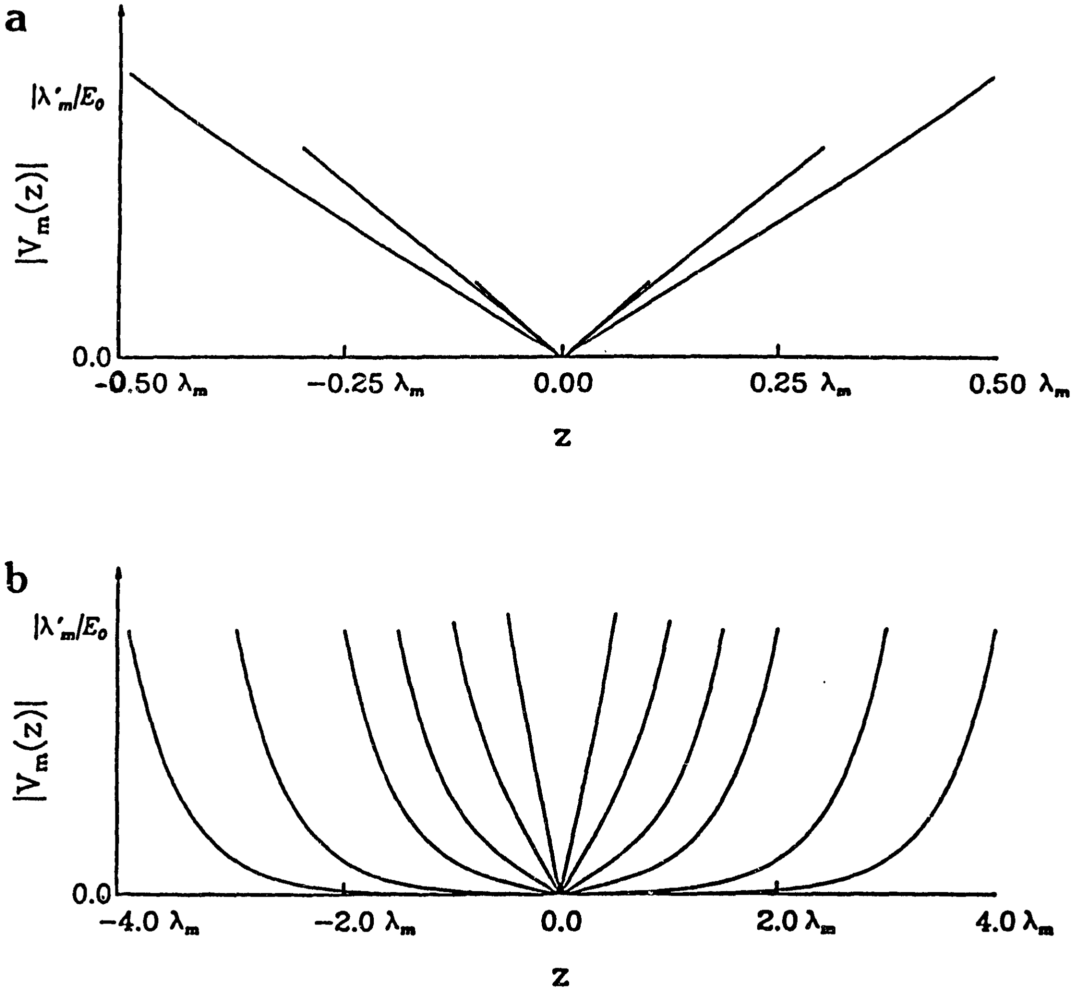

Figure 2.4: Spatial dependence of the induced transmembrane potential predicted by the cable model analysis for isolated cells. Plots indicate the magnitude of $V_m(z)$ at 60 Hz against position along the long axis of the cell (z) for cells having radius 100 μm, and (a) lengths $0.2\lambda_m$, $0.6\lambda_m$, λ_m, and (b) lengths λ_m, $2.0\lambda_m$, $3.0\lambda_m$, $4.0\lambda_m$, $6.0\lambda_m$, and $8.0\lambda_m$. The cells are centered on the z–axis.

maximum value of $|V_m(\pm L)|$ reaches E_o $|\lambda'_m|$, because the space constant λ_m reflects the value of the membrane conductivity relative to the conductivity of the intracellular and extracellular fluid.

In the sinusoidal steady state, $|V_m(\pm L)|$ does not increase monotonically with cell length, as expected for the d.c. case. Instead, it reaches its first and only significant maximum at a length which is determined by the frequency, the cell radius, and the electrical properties of the membrane. Then $|V_m(\pm L)|$ decreases to a plateau of $|\lambda'_m|E_o$. This behavior is illustrated in Figure 2.5(a).

For long cell, $|V_m(\pm L)|$ is strongly dependent on cell radius. For short cells ($L << \lambda_m$), $|V_m(\pm L)|$ is independent of cell radius. However, as the radius increases, the length of the cell over which membrane resistance governs the intracellular current increases. This added length allows a higher potential to be imposed across the ends of the cell as illustrated in Figure 2.5(b).

These results suggest a classification of cells into three groups, depending on their electrical properties. The electrically long cells, having large length–to–radius ratios, have a $|V_m(\pm L)|$ which is independent of length, but increases with radius. The electrically short cells, having small length to radius ratios, have a $|V_m(\pm L)|$ which is independent of radius, but increases with length. Cells having dimensions between these two limits have a $|V_m(\pm L)|$ which increases with both length and radius.

The effect of adjacent cells is fundamentally to limit the extracellular space available to each cell. This results in an increase in the maximum transmembrane potential for any given cell length and radius. The smaller the extracellular space, the greater the increase. This is illustrated in Figure 2.6 where $|V_m(\pm L)|$ is plotted as a function of b/a for a cell of length 10 mm (L=5 mm) and radius 50 μm. This result can be readily interpreted. When a cell is isolated in extracellular fluid, the low resistance of the extracellular fluid acts to short out the voltage drop across the length of the cell. In other words, the current tends to flow around the cell rather than through

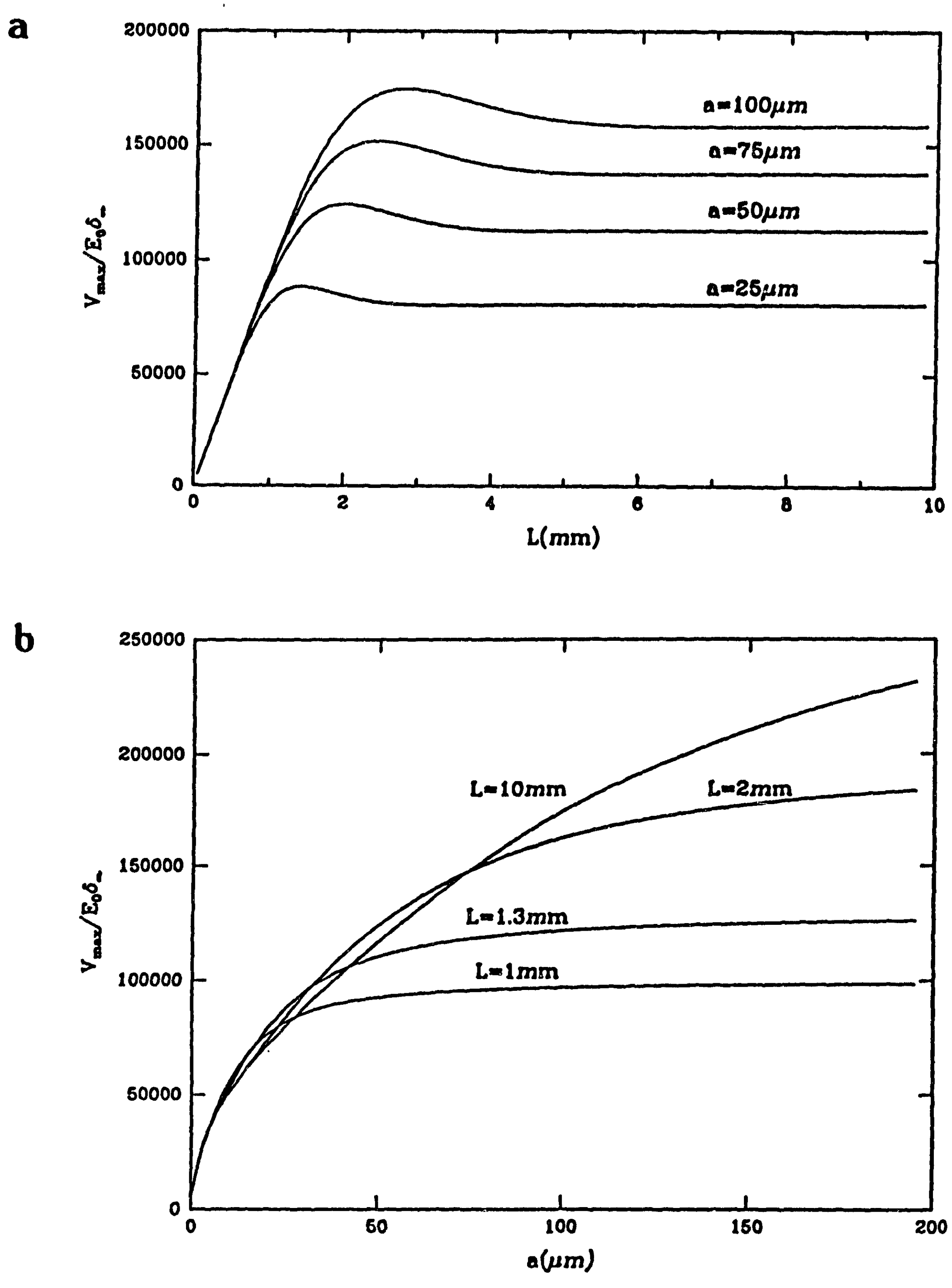

Figure 2.5: Cable model prediction of the magnitude of the induced transmembrane potential at the end of an isolated skeletal muscle cell parallel to an applied electric field as a function of (a) cell length $2L$ for selected radii a and (b) cell radius for selected lengths. This potential is the maximum induced along the length of the cell and is thus designated V_{max}. Here V_{max} is normalized to the potential drop across a distance δ_m, the thickness of the cell membrane, in the uniform field to indicate the "amplification" of the field in the membrane.

the cell. With other cells in close proximity, the resistance of the extracellular path increases and more current will flow end-to-end through the cell. This results in a greater transmembrane potential at the ends of the cell. In addition, because the space constant λ_m is decreased by an increased r_o, the induced transmembrane potential is more confined near the ends of the cells.

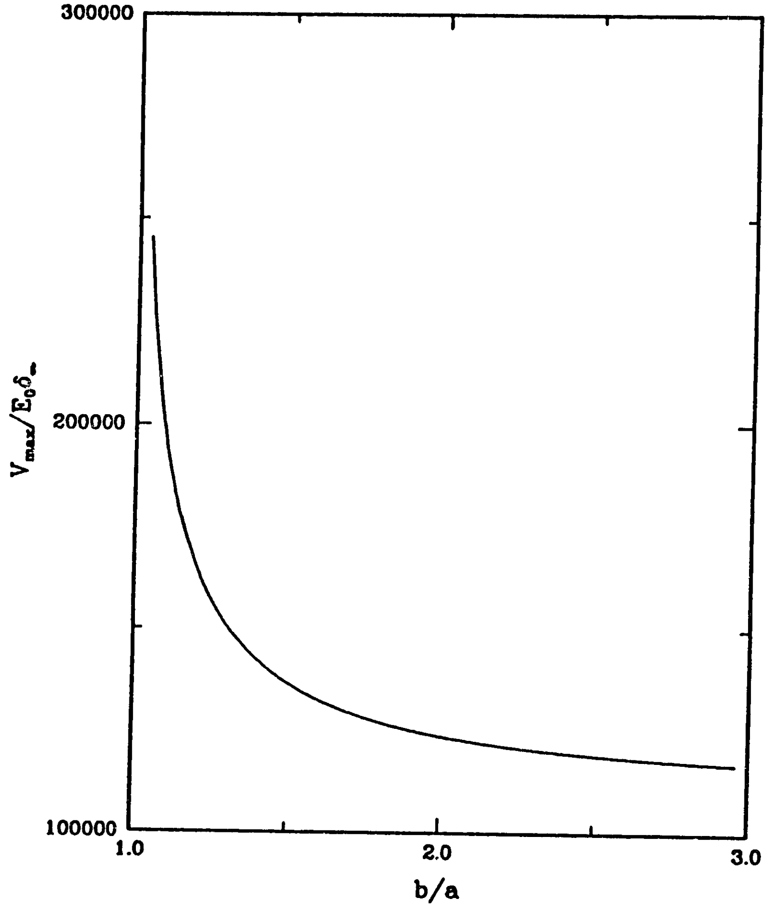

Figure 2.6: Cable model prediction for the maximum induced transmembrane potential in skeletal muscle cells (L = 5 mm, a = 50 μm) arranged in a hexagonal array as a function of the extracellular spacing b/a. Here V_{max} is normalized to the potential drop across a distance δ_m, the thickness of the cell membrane, in the uniform field to indicate the "amplification" of the field in the membrane.

As the ratio b/a becomes large, that is, as r_o becomes small, $|V_m(\pm L)|$ approaches that predicted for an isolated cell of the same dimensions. As the ratio b/a approaches unity, that is, as r_o approaches infinity, the cell appears to be a lumped three–element voltage divider. Thus, in the d.c. case,

$$|V_m(\pm L)| \approx \frac{V_c}{2} \frac{1/(2Lr_i)}{G_e/2 + 1/(2Lr_i)}, \qquad \text{when} \quad b/a \approx 1 . \tag{2.18}$$

The voltage divider does not depend on cell radius, and is in fact the same voltage divider relationship derived for isolated cells of short length to radius ratios (Equation 2.13). This is not surprising since a bundle of cells with no extracellular space ($r_o = \infty$) will behave like a single cell of the same length, but greater radius. Thus, the response can be described by the isolated cell model, with $E_o = V_c/2L$.

It has been shown that the presence of neighboring cells in a tissue prevents current from being diverted around a given cell, and instead forces more current to flow through the ends of the cell. This effect is more pronounced the closer the neighboring cells are located. The same idea can be applied to a study of the effects of various other cellular environments on the imposed transmembrane potential and, thus, the vulnerabilities of various cells to breakdown.

It seems reasonable that cells at the very edge of an intact muscle would experience a lower transmembrane potential than those cells in the interior, since cells on the edge are exposed to the more highly conducting fascial planes which short out the potential. The situation for cells adjacent to cortical bone is exactly the opposite. The cortical bone, being less hydrated than extracellular fluid, is far more resistive. As a result, cells next to bone would experience a higher transmembrane potential due to a greater amount of current flowing through the cell membranes. Thus, it seems reasonable that the cells closest to the bone are more likely to be ruptured by non–thermal electrical forces than the cells adjacent to the fascial plane.

These results suggest a pattern of injury which correlates strongly with clinical observation. When the current path includes an upper extremity, victims of electrical trauma have been found to develop a characteristic pattern of tissue injury. In tissue locations far enough away from the surface contact points so that the local temperature is unaffected by intense skin heating, the muscle injury has been observed to be the most severe around bone (Baxter, 1970; Hunt et al., 1980) and in the central core of the muscle (Zelt et al., 1986).

Charging Time

The response to a d.c. applied electric field can easily be found from the previous analysis by setting ω to zero. However, the time required for the cell to reach the predicted transmembrane distribution is still to be determined. Just as the voltage of a capacitor cannot change instantaneously, the transmembrane potential will not change instantaneously either. As demonstrated by Cooper (1986), a modal transient solution to the cable equation that is axisymmetric about $z = 0$ is

$$V_t(z,t) = \sum_{n=1}^{\infty} A_n \sin(\alpha_n, z/\lambda_m) e^{-(1+\alpha_n^2)t/\tau_m}; \qquad \alpha_n = \frac{n\pi\lambda_m}{2L} \tag{2.19}$$

Thus, the time–dependent terms decay with a time constant

$$\tau_n = \frac{\tau_m}{1 + (\frac{n\pi\lambda_m}{2L})^2} . \tag{2.20}$$

The time τ_1 is the maximum time constant and is thus the time required for the cell to attain the transmembrane potential distribution predicted by the cable model analysis. For long cells, this time approaches τ_m (typically on the order of milliseconds), but decreases for cells of decreasing length. The fact that the charging time is on the order of milliseconds implies that for a 60 Hz applied field, the cell may not charge to its maximum value during each excursion of the sinewave, since the duration of each excursion is about 8 msec and its magnitude is only above the root–mean–square value for 4 msec.

2.1.2 Perpendicular Case

To determine the induced transmembrane potential for an elongated cell aligned perpendicular to an applied electric field, the cell is modeled as an infinitely long cylinder, the cross–section of which is illustrated in Figure 2.7. Neglecting the ends in this way is of little significance since it is the maximum transmembrane potential that is required and this will occur in the middle of the cell, where the end effects will be negligible. The transmembrane potential will decrease as the ends are approached. Only the d.c. case will be considered here, since d.c. was used in all experimental protocols.

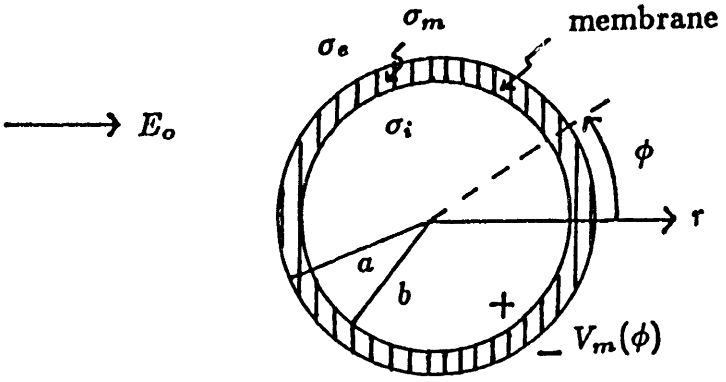

Figure 2.7: Cross section of a skeletal muscle cell aligned perpendicular to an applied d.c. electric field E_o. The induced transmembrane potential V_m is a function of ϕ, being maximum at $\phi = 0°$ and at $\phi = 180°$. Membrane thickness is $a - b$. Conductivities are denoted by σ's.

This case presents a simple three–region problem requiring solutions to Laplace's equation in cylindrical coordinates. The solution must be finite at the origin, equal E_0 at infinity and satisfy the charge conservation boundary conditions at the interfaces. The d.c. potential distribution inside the membrane is

$$\Phi_m = \frac{-2\sigma_e E_0}{\frac{-(\sigma_m+\sigma_e)(\sigma_i+\sigma_m)}{b^2(\sigma_i-\sigma_m)} + \frac{(\sigma_e-\sigma_m)}{a^2}} \left[\frac{-r\cos\phi}{b^2}\left(\frac{\sigma_i+\sigma_m}{\sigma_i-\sigma_m}\right) + \frac{\cos\phi}{r}\right], \qquad (2.21)$$

where E_0 is the magnitude of the applied electric field, a and b are the outer and inner radii of the cell, respectively, and σ_e, σ_m, and σ_i are the conductivities of the extracellular fluid, the membrane, and the cytoplasm, respectively. Since the membrane conductivity is much less than the conductivities of either the extracellular fluid or the cytoplasm, this expression can be simplified considerably:

$$\Phi_m = \frac{2E_0 \cos\phi}{\frac{1}{a^2} - \frac{1}{b^2}}\left(-\frac{r}{b^2} + \frac{1}{r}\right) . \tag{2.22}$$

Analyzing this expression at $r = a$ illustrates that the potential distribution at the outside edge of the membrane is the same as that of a perfectly conducting cylinder. This is due to the large resistivity of the membrane compared to the fluids, and to the geometry of the problem. Thus, it is reasonable to assume that only negligible current flows across the membrane and through the cytoplasm, and the maximum transmembrane potential is half the value of the maximum voltage drop across the cell. This maximum occurs at $\phi = 0°$ and at $\phi = 180°$, and is equal to $2E_0a$.

Charging Time

The charging time for the three–region problem illustrated in Figure 2.7 is a complicated function of the three permittivites, the three conductivities, and the geometrical parameters a and b. However, when approximations are made using the fact that the membrane conductivity is much less than that of the surrounding fluids, the charging time simplifies to that for an insulating cylinder:

$$\tau \approx \frac{\epsilon_e}{\sigma_e} . \tag{2.23}$$

This time is generally on the order of nanoseconds. This is obviously an underestimate of the charging time since it assumes no current flow through the membrane; however, it is clear that the charging time for cells perpendicular to the applied electric field will be orders of magnitude less than the charging time for long cells parallel to the field.

2.2 Muscle Impedance Model

As demonstrated by Chilbert et al. (1985) and Bhatt et al. (1990), the impedance of skeletal muscle tissue drops following electrical injury by an amount that depends on the extent of the damage incurred. In order to explore the physical reasons for the impedance drop and to develop a method for predicting the magnitude of the drop, a skeletal muscle tissue impedance model was developed. Of primary concern is the longitudinal impedance, that is, the impedance measured when the applied current is parallel to the long parallel muscle cells in an intact muscle. This is the predominant current distribution in most electrical injuries.

The model uses the one–dimensional cable model for single elongated cells in a uniform electric field to represent the behavior of the individual cells in the whole muscle. The cable model for a single cell represents the electrical properties of the components of the system (extracellular fluid, cell membrane, and cytoplasm) in terms of a lumped resistor–capacitor network. Using the single cell network as a unit, a whole muscle model can be formed by connecting these units in parallel to represent parallel cells and in series to represent cells aligned end–to–end, as illustrated in Figure 2.8. The resulting one–dimensional model of the transmembrane potential distributions of all the cells in the muscle can be used to derive an expression for the impedance of the whole muscle.

To derive the impedance of a single cell with its surrounding extracellular fluid, the total voltage drop across the cell (V_c) and the total current through the cell and extracellular fluid (I_c) must be derived. The impedance Z_c is then V_c/I_c. The voltage drop across the cell can be expressed

$$V_c = 2\left[V_m(L) + \int_0^L r_i I_i(z)dz\right] , \qquad (2.24)$$

or equivalently,

$$V_c = 2\int_0^L r_o I_o(z)dz . \qquad (2.25)$$

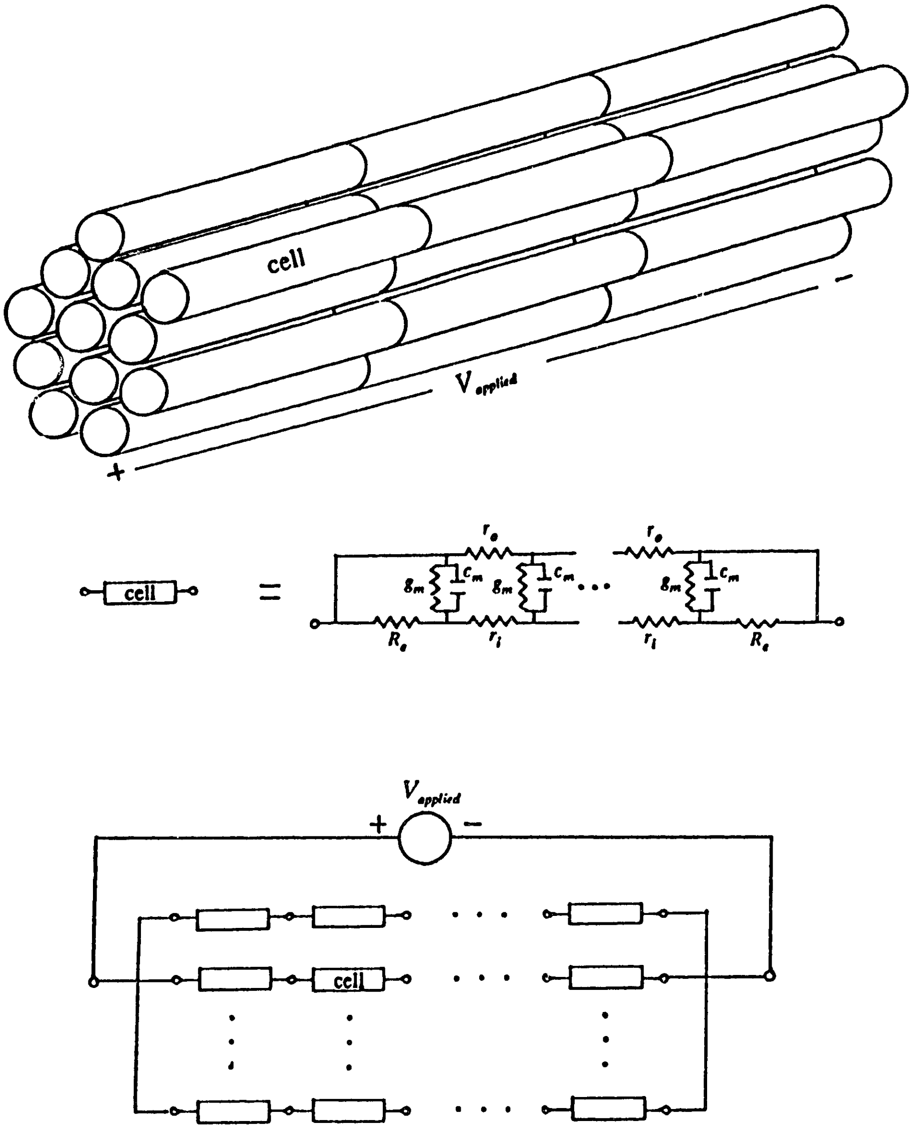

Figure 2.8: Cable model representation of intact skeletal muscle.

The current $I_i(z)$ can be expressed

$$I_i(z) \;=\; I_i(-L) \;-\; \int_{-L}^{z} g'_m V_m(z)dz \,. \tag{2.26}$$

The transmembrane potential distribution $V_m(z)$ and the end current $I_i(-L)$ were derived in the tissue model analysis and are given in Equations 2.17 and 2.10 respectively. Thus, it can easily be shown that

$$V_c/A' \;=\; 2\sinh(L/\lambda'_m) \;+\; 2r_i(G'_e L - \frac{1}{r_i + r_o})\sinh(L/\lambda'_m) \;+\; 2r_i g'_m \lambda'_m L \cosh(L/\lambda'_m) \,, \tag{2.27}$$

where A' is the coefficient derived in the tissue model analysis.

The total current I_c is easily evaluated by examining the parameters at $z = 0$, since

$$I_c \;=\; I_i(0) \;+\; I_o(0) \,. \tag{2.28}$$

Using Equation 2.15 and Equation 2.26, both evaluated at z=0, it is easy to show that

$$I_c/A' \;=\; \frac{1}{r_o\lambda'_m} \;+\; (1 + \frac{r_i}{r_o})[G'_e \sinh(L/\lambda'_m) + g'_m\lambda'_m(\cosh(L/\lambda'_m) - 1)] \,. \tag{2.29}$$

Thus,

$$Z_c \;=\; \frac{2L\frac{r_i r_o}{r_i + r_o} \;+\; 2r_o\lambda'_m[1 + r_i G'_e L - \frac{r_i}{r_i + r_o}]\tanh(L/\lambda'_m)}{1 \;+\; (r_o + r_i)\lambda'_m G'_e \tanh(L/\lambda'_m)} \,. \tag{2.30}$$

To obtain the impedance of an intact muscle from this value for a single unit cell, it is only necessary to multiply by the number of cells aligned end–to–end in the muscle (m) and divide by the number of cells in parallel in the muscle (n).

The single cell cable model predicts that rupture is most likely to occur at the ends of the cells, since that is where the induced transmembrane potential is the greatest. Thus, it appears valid to model a ruptured cell as a resistor having the resistance of the extracellular fluid in parallel with the resistance of the intracellular fluid, since a cell which is ruptured at the ends provides an open pathway for current flow from the extracellular space through the cytoplasm without the diversion around the membrane at the ends. Thus a ruptured cell has an impedance

$$Z_r = 2L \frac{r_i r_o}{r_i + r_o} . \tag{2.31}$$

The model for the longitudinal impedance of muscle can be adapted to form a model for electrically–damaged muscle by replacing a specified percentage of the cells with damaged cells of impedance Z_r. For an array of cells with n arbitrary and m equal to one, the change in impedance due to rupture of a specified percentage of the cells can be easily determined. For simplicity, the d.c. case will be considered using typical values for the cell dimensions and electrical properties. Using $\sigma_i = \sigma_o = .01$ mho/cm, $G_m = 1 \times 10^{-4}$ mho/cm^2, $L = 0.5$ cm, $a = 5.0 \times 10^{-3}$ cm, and $b/a = 1.05$, the impedances of intact and ruptured cells are $Z_c = 4.5$ MΩ and $Z_r = 1.2$ MΩ. Thus, when 100% of the cells are ruptured, the impedance of the tissue drops by about 73%. When 50% and 25% of the cells are ruptured, the drops are about 58% and 41% respectively. This compares well with the observations of Chilbert et al. (1985) who measured drops of 70% in tissues exhibiting severe necrosis, and drops of 20–40% in tissues exhibiting minimal necrosis. The measurements of Bhatt et al. (1990) show similar impedance drops (see Figure 1.19) in tissues damaged by pure electrical mechanisms.

In the previous calculations, the impedance drop was calculated using $m = 1$, that is, for no cells end–to–end. For $m > 1$, the calculations are more difficult, unless it is assumed that all damaged cells are end–to–end with other damaged cells and all healthy cells are end–to–end with healthy cells. This is probably not a realistic assumption. However, in cases of high percentage of damaged cells, this assumption is not as important, and the predictions for $m = 1$ are valid approximations. For cases of low percentage of damaged cells, the analysis for $m = 1$ will predict an impedance drop higher than can be expected if the damage is randomly distributed.

While it appears that this model is useful in interpreting the observed impedance drops associated with damaged tissue, it has limitations in other respects. The frequency response that it predicts rolls off at a frequency determined almost entirely by the membrane time constant $\tau_m = C_m/G_m$. Using $C_m \approx$ 1.0–10.0 μF/cm^2 and $G_m \approx$ 1.0–2.5$\times$ 10^{-4} mho/cm^2, this frequency is $\tau_m^{-1} \approx$ 10–250 Hz, a range far lower than observed experimentally (Zheng et al., 1984; Bhatt, 1988). This could be due to inaccurate numerical values for the parameters in the model, but is more likely due to the influence of the complex structures of the skeletal muscle cell, such as the T–tubule network and the sarcoplasmic reticulum, which were not included in this simple model.

Chapter 3

Experimental Methods

Experimental protocols were designed to observe the response of skeletal muscle cells to electrical and thermal stimuli and to determine the thresholds for membrane damage due to membrane electrical breakdown and Joule heating. Rat sketetal muscle cells were harvested for use in these experiments. Custom–built exposure chambers allowed real–time observation of cells with a microscope. Experiments were video–recorded and digitized images were stored for later analysis using image processing techniques. Induced transmembrane potentials due to weak applied electric fields were imaged using the membrane–incorporating potential–sensitive fluorescent dye di–4–ANEPPS. The cytomorphological changes induced by intense electric field pulses and elevated temperatures were observed using cells bathed in phyiological solution. Both stimuli led to cell twitching and contraction. In separate experiments using cells paralyzed in hypertonic solutions and loaded with the fluorescent dye carboxyfluorescein, induced changes in membrane diffusive permeability were observed and quantified.

3.1 Isolation and Culture of Rat Skeletal Muscle Cells

Rat skeletal muscle cells were harvested from the flexor digitorum brevis muscle of the hind foot of adult female Sprague–Dawley rats (Bekoff & Betz, 1977; Bischoff, 1986).

This muscle consists of a few thousand short muscle cells divided into three slender muscles to flex the second, third and fourth digits.

First, a rat was sacrificed by asphyxiation in 100% CO_2 using a protocol approved by the Massachusetts Institute of Technology Animal Studies Committee. The muscles were quickly excised and immediately placed in a specimen container filled with Dulbecco's Modified Eagle's Medium (DMEM) (GIBCO, Grand Island, NY). The DMEM was supplemented with antibiotics at 2× concentrations (1000 U/ml penicillin and 1000μg/ml streptomycin, GIBCO), 25 mM HEPES Buffer (Sigma, St. Louis, MO) and 10% NuSerum (Collaborative Research, Waltham, MA), a partially-defined serum formula, less variable from lot to lot than serum derived entirely from an animal.

The cells were loosened from the intact muscle by digestion of the extracellular matrix using 1.5 mg/ml collagenase (type II, Sigma) in the supplemented DMEM. Digestion was allowed to proceed for about 2.5 hours at 37°C. Then the muscles were washed 4 times in the supplemented DMEM to remove the collagenase. To obtain the cells from the muscle, the tendons were teased apart and the pieces were pipetted up and down gently in a wide-mouth pipette. These short cells could survive this mechanical agitation, which has been shown to easily damage and break longer skeletal muscle cells (Bekoff & Betz, 1977). The resulting suspension of isolated cells was pipetted into several 60 mm glass petri dishes. Cells were maintained in a 5% CO_2–95% air incubator at 37°C and 99% humidity until used in experiments.

The isolated muscle cells were 600 to 1200 microns in length and 15 to 30 microns in diameter. Several hundred cells could be obtained from each digested muscle. Under 10× and 40× phase contrast optics, the characteristic striations and numerous nuclei were clearly visible, as illustrated in Figure 3.1. Evidence of the vitality of the cells included their characteristic striated appearance, indicating a functioning outer membrane, and their ability to incorporate and de-esterify the vital dye fluorescein diacetate (Rotman, 1973). Damaged cells would hypercontract, making them easily distinguishable from the healthy cells.

The cells could be maintained in culture for at least one week. The cells did not readily adhere to the glass petri dish, but remained in suspension, which facilitated their use in experiments. However, after several days in culture, the fibroblast population would cover the bottom of the petri dishes and skeletal muscle cells would begin to attach in clumps to the fibroblasts. At this point, some of the skeletal muscle cells in the clumps, and occasionally isolated cells, would begin to fibrillate.

Bekoff and Betz (1977) have shown that cells dissociated using this technique have a slightly low resting transmembrane potential of about -60 mV, compared to the -70 – -80 mV range observed in undissociated mammalian muscle cells. This resting potential was shown to remain constant for up to 12 days in culture. However, the normal value of the specific membrane resistance (500 Ωcm^2) that was measured for these cells indicates that the dissociation procedure does not lead to a change in membrane permeability.

3.2 Use of Fluorescent Dyes

3.2.1 Carboxyfluorescein

Fluorescein diacetate (FDA) and carboxyfluorescein diacetate (CFDA) (M.W. 460.4) (Molecular Probes, Eugene OR) were used to determine cell viability and to demonstrate and quantify changes in cell membrane permeability. These dyes diffuse across cell membranes, where esterases of healthy cells cleave the dye molecules producing fluorescein and carboxyfluorescein. These are negatively–charged fluorescent molecules that do not diffuse readily across the cell membrane and thus accumulate in the cytoplasm. Only cells with cell membrane integrity will retain the dye. These dyes are commonly used as a test of viability in a large range of cell types and to measure subtle changes in membrane permeability. The fluorescence intensity of fluorescein dyes is also pH dependent and has been used as a probe for measurement of intracellular pH

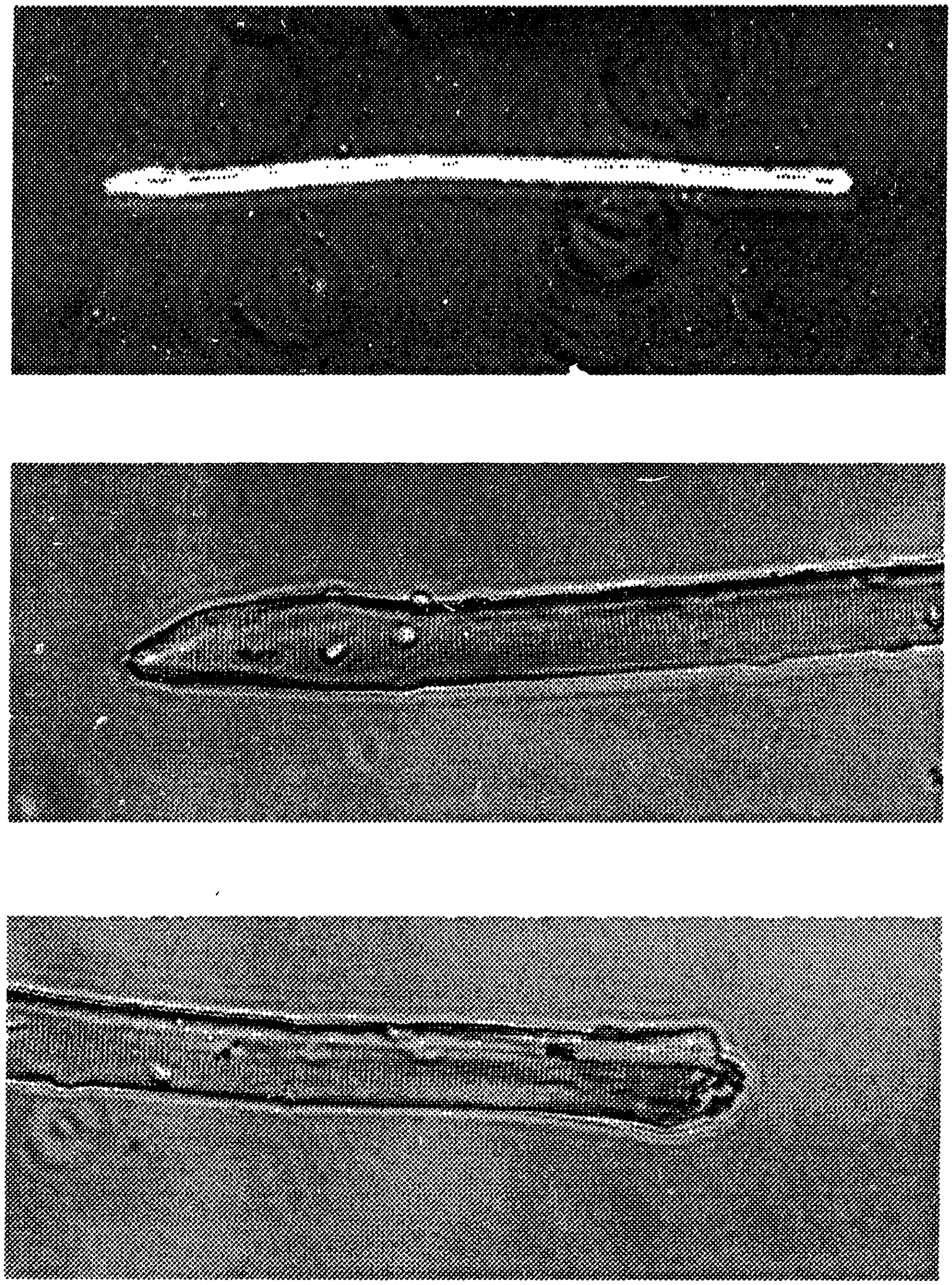

Figure 3.1: Isolated rat skeletal muscle cell photographed using 10× and 40× phase contrast optics. Cells were typically 600 to 1200 μm in length and 15 to 30 microns in diameter. The characteristic striations and numerous nuclei are clearly visible. The two ends illustrate typical morphologies of skeletal muscle cell end regions.

(Cowden, 1985). The molecular stucture of CFDA and the spectral response curves for the excitation and emission of carboxyfluorescein are shown in Figure 3.2.

It was established that 10 μl of FDA or CFDA (derived from a 4 mg/ml stock solution in acetone) added to 5.0 ml of cell suspension in DMEM labelled skeletal muscle cells brightly. The cells were allowed to incubate for about 15 minutes at 37°C to incorporate the dye before use in experiments. CFDA provided better results than FDA since FDA hydrolyses to a much less hydrophobic fluorophore and thus leaks more rapidly from the cell.

3.2.2 di–4–ANEPPS

The potentiometric dye di–4–ANEPPS (Molecular Probes) was used to image the potential drop across the cell membrane. This dye is taken up by cell membranes and undergoes a change in fluorescence intensity of approximately 8–10 % per 100 millivolt change in transmembrane potential (Gross & Loew, 1989). di–4–ANEPPS is classified as a charge–shift dye since it undergoes a large charge shift upon excitation. The energy difference between the ground and excited states is therefore sensitive to an external electric field oriented in the direction of the shifting charge. The response to potential changes is fast, occurring on the order of milliseconds. The dye is commonly used to image the spatial variation in potential along the surface of a cell. The molecular stucture of di–4–ANEPPS and its spectral response curves for excitation and emission are shown in Figure 3.3.

It was determined that 10 μl of di–4–ANEPPS (derived from a 1.0 mg/ml stock solution in 20% ethanol – 80% phosphate–buffered saline) added to 5.0 ml of cell suspension in DMEM labelled cells properly. The muscle cells were allowed to incubate for about 15 minutes at 37°C to incorporate the dye. It was obvious that cells with membrane integrity were stained only in the outer membrane by the bright edges observed under fluorescence microscopy. Cells with disrupted membranes would appear

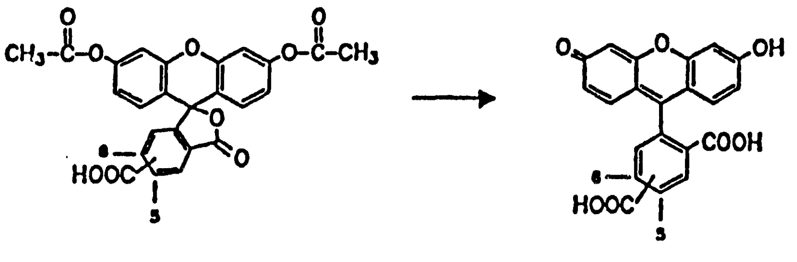

Carboxyfluorescein Diacetate   Carboxyfluorescein

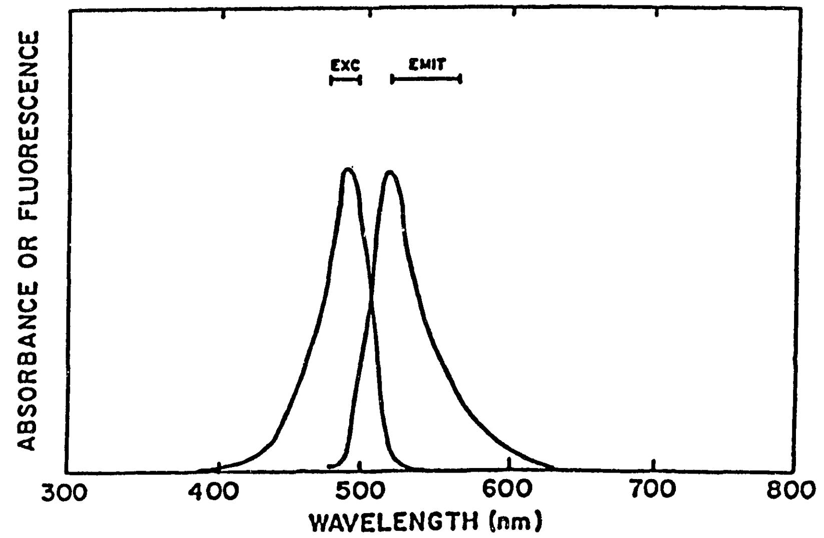

Figure 3.2: Molecular structure of carboxyfluorescein diacetate and carboxyfluorescein, the product of intracellular enzymatic hydrolysis (taken from Haugland, 1989), and spectral response curves for the excitation and emission of the fluorescent molecule carboxyfluorescein (adapted from DeBiasio et al., 1987).

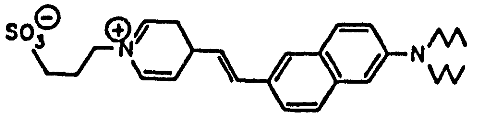

DI-4-ANEPPS

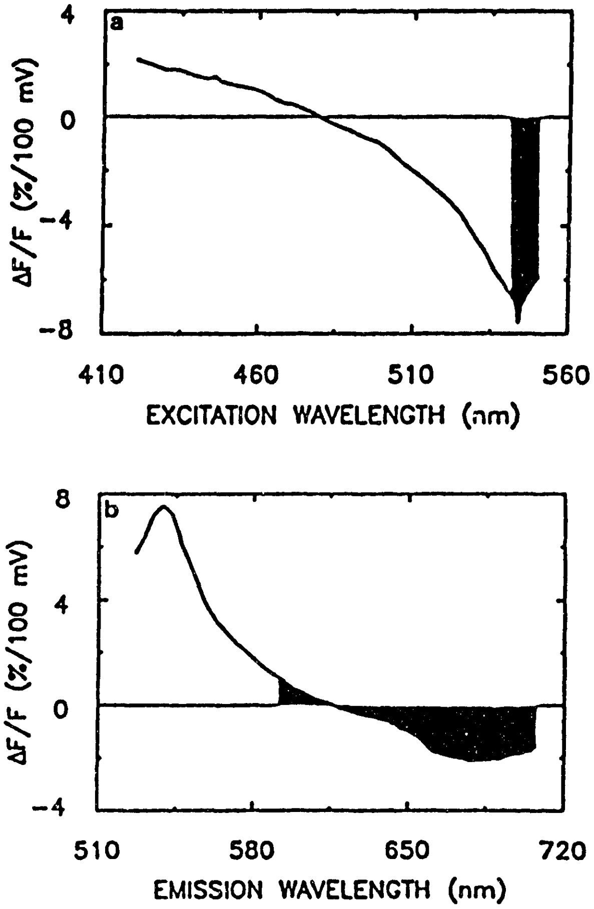

Figure 3.3: Molecular structure and spectral response curves for the fluorescent dye di-4-ANEPPS. Excitation and emission changes in response to a change in transmembrane potential are indicated. The shaded portions indicate the best choice of filter wavelengths for the largest relative response. (Taken from Gross & Loew, 1989.)

bright throughout, due to the staining of the internal membranes of the cell. Thus, it was very easy to choose the healthiest cells for use in the experiments.

3.3 Use of Hypertonic Solutions to Paralyze Cells

In order to monitor changes in membrane permeability using fluorescent dyes, it was necessary that the cells remain absolutely still during the protocols. Unfortunately, application of an electric field produces an action potential which leads to twitching and contraction. It was also discovered that heating leads to contraction. Therefore, it became necessary to artifically prevent these physiologic responses. Many techniques have been discussed in the literature for altering the cellular response to an action potential (R. Eisenberg, 1983, Caputo, 1983). Most of the methods merely diminish or delay response. However, one of the most common techniques, bathing the cells in hypertonic solutions, is often used to completely paralyze skeletal muscle cells. It has been shown that contractility can be completely blocked by exposure to solutions of tonicity made two– to three–times normal by the addition of solutes unable to penetrate the cell membrane. Membrane properties such as the transmembrane potential are not significantly affected.

The mechanism of muscle cell paralysis caused by hypertonic solutions is not totally understood. In an early study, Howarth (1958) proposed that since some water will exit a cell in hypertonic solution due to osmosis, the fiber diameter will shrink, which may lead to an increased cytoplasm viscosity and friction between parallel sliding contractile proteins. He also hypothesized that the change in cytoplasmic concentration of certain ions may effect the actin and myosin proteins.

While it appears that the hypertonic solutions primarily effect the contractile mechanism directly, effects on the excitation–contraction coupling have also been observed. Parker and Zhu (1987) have demonstrated significant suppression of intracellular calcium transients in frog muscle cells exposed to tonicities greater than two–times normal. Tonicities of three–times normal diminished the transients by half, while tonicities of four–times normal blocked them completely. In addition, hypertonic solutions have been shown to suppress depolarization–induced tension more than caffeine–induced tension, which does not depend on the excitation–contraction mechanism.

In preliminary experiments with harvested rat skeletal muscle cells, it was determined that although a tonicity of 2.5–times normal was often sufficient to suppress the contractile response, a tonicity of 3.0–times normal was required to reliably paralyze nearly all cells in all the protocols. Thus, for use in the experiments, the tonicity of phosphate buffered saline (PBS) was made 3.0–times normal with either sucrose or mannitol. Both molecules do not permeate healthy cell membranes. Assuming the isotonic osmolarity of PBS is about 280 mOsm, the solutions were prepared to have an osmolarity of about 840 mOsm, attained with 192 gm/l sucrose (molecular weight 342.30) or 102 gm/l mannitol (molecular weight 182.17). Although decreases in cell volume were expected when the cells were exposed to the hypertonic solutions, no obvious changes were often evident, as illustrated in Figure 3.4 where a cell is shown in both isotonic and hypertonic solutions. Cytomorphological changes were sometimes observed, the most common being kinks in the cell, causing them to curve. Unhealthy cells would contract irreversibly when exposed to the solution. Cells exhibiting noticeable deformations were avoided in the experiments.

3.4 Image Processing

In order to analyze fluorescence images of cells, a computer–controlled image processing system capable of image acquisition, enhancement, and analysis was employed. Images were digitized in real–time or from tape into one of three 512×512×16 bit frame buffers of a Hamamatsu image processor (Hamamatsu City, Japan). Sixty–four thousand intensity levels were available with the 16–bit encoding scheme used. The buffer contents were then transferred via DMA interface to the memory of a Vax-

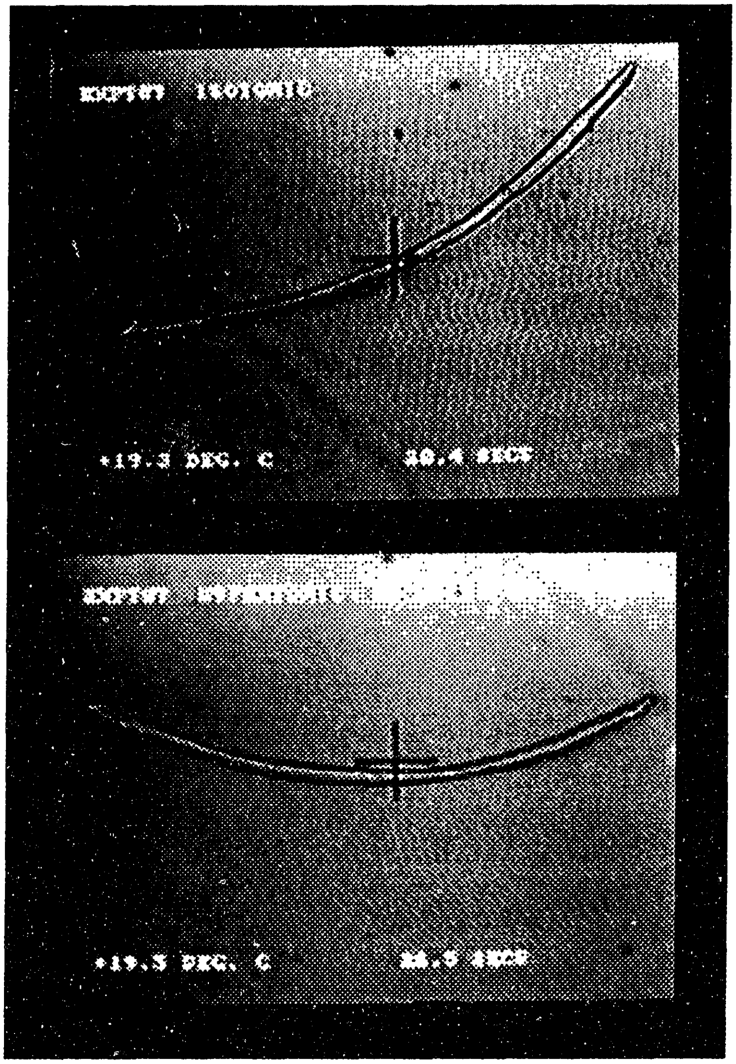

Figure 3.4: Rat skeletal muscle cell photographed in isotonic and then in hypertonic solution (3.0–times normal tonicity). As shown, no obvious cytomorphological changes were induced by the exposure to the hypertonic solution.

Station II computer (Digital Equipment Corp.). Because of the time required to store images to fixed disk, the storage rate was limited to 1 image every 4 seconds. Typically 64 frames at 1/30 second per frame were averaged into each image; thus, the mean image acquisition and storage throughput was approximately 1 image every 6 seconds.

To analyze the images, a menu-driven digital image processing package custom-designed by D. Askey (1987) was employed. The software was capable of identifying the cell by the range of intensities it occupied compared with the range occupied by the background.

First, a frame of video was loaded into the frame memory of the image processor. Then, a window of the image background specified by the user was sampled. A Gaussian distribution of intensities within the window was assumed. The mean and the range of the background intensities were calculated. The range was defined as two standard deviations above and below the mean, and thus 96% of the samples fell within the range.

Next, the program sampled a user-specified window that contained the cell of interest and accumulated an intensity histogram of the window. It searched the part of the histogram corresponding to the background and subtracted out the background peak. Then the program looked for the remaining mode intensity and, assuming a Gaussian distribution of cell intensities, located the range of cell intensities as the range of intensities above the background range and symmetric about the mode. Data on the cell area (in number of pixels) and the average cell intensity were returned. Average cell intensities were reported in two ways: referenced to the background median and normalized to the background median. Normalized data helped correct for background intensity fluctuations that sometimes occurred during a single experiment. The same method was used to analyze small sections of a cell. In this case, the progam identified the entire cell window as cell and proceeded accordingly.

3.5 Imaging the Induced Transmembrane Potential

Induced transmembrane potentials in skeletal muscle cells were imaged using the membrane–incorporating potential–sensitive fluorescent dye di–4–ANEPPS, described in Section 3.2.2. The experimental system used to apply weak electric fields to the cells and to observe, record, and analyze the response is illustrated in Figure 3.5.

3.5.1 Exposure Chamber

The chamber used to apply electric fields to isolated skeletal muscle cells is illustrated in Figure 3.6. The space occupied by the cells above the glass window and below the coverslip was 200 μm thick. When the chamber was filled with medium, this thin region had a resistivity much greater than the other channels of the chamber. Thus, most of the applied voltage dropped across this section, which was approximately 2 cm long. An applied voltage of A V led to a field experienced by the cells of about $A/2$ V/cm.

Platinum electrodes were mounted on opposite ends of the chamber. Platinum was chosen for its resistance to corrosion. The distance between the electrodes and the cell exposure area (about 3 cm) isolated the cells from any electrode products for times well beyond that of the experimental protocols (on the order of one minute).

Since electric field application for several seconds was required, heating was conceivably a problem, depending on the magnitude and duration of the applied voltage. The chamber provided a mechanism of cooling by a flow of cooled nitrogen gas. A copper–constantan foil thermocouple (RdF Corp., Hudson, NH) permanently mounted below the glass window allowed constant monitoring of the temperature.

The expected temperature rise in the chamber during the application of a single

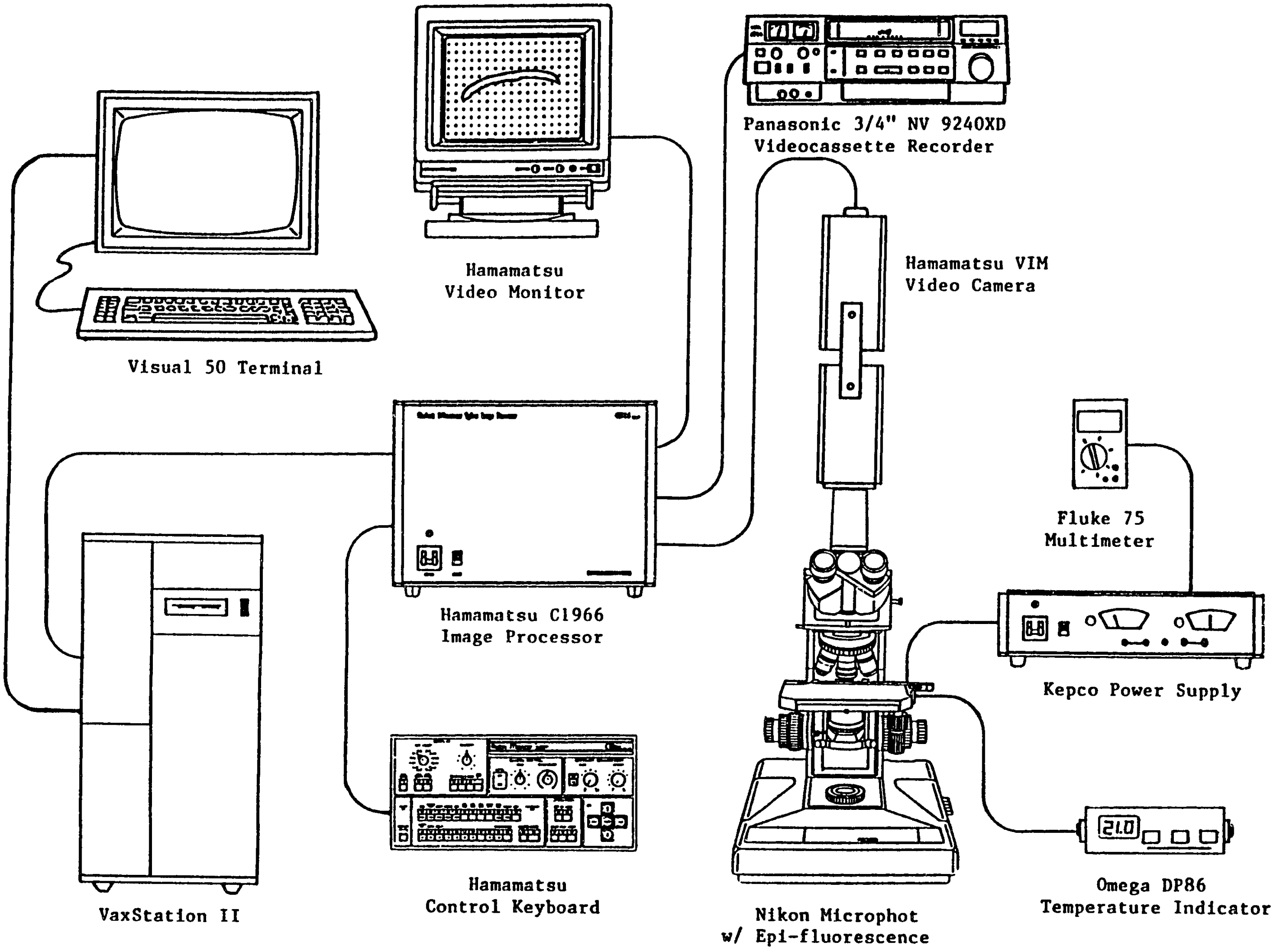

Figure 3.5: System used to image the induced transmembrane potential in isolated skeletal muscle cells in an applied electric field using di-4-ANEPPS.

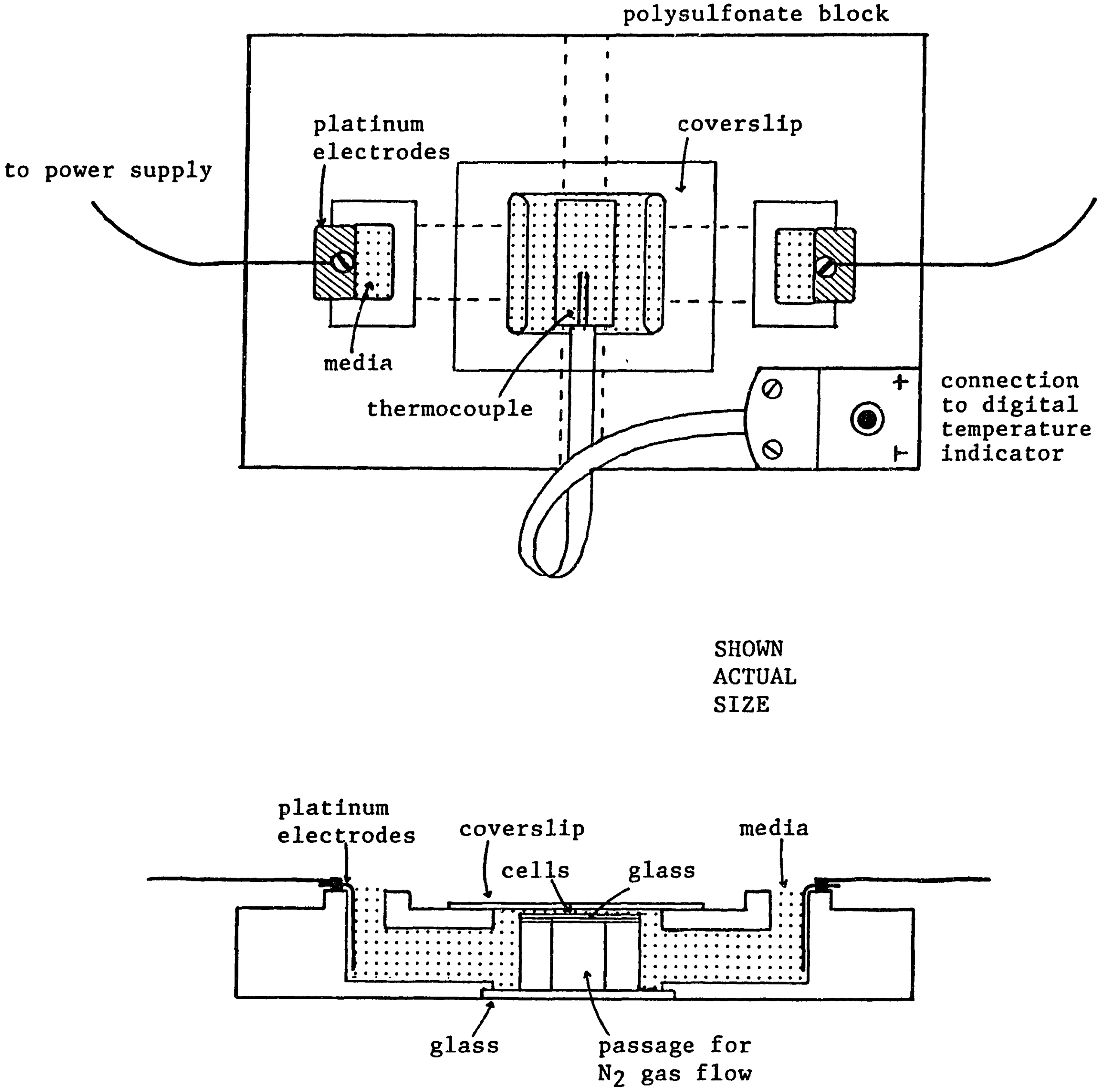

SHOWN
ACTUAL
SIZE

Figure 3.6: Chamber used to expose isolated skeletal muscle cells to electric fields in order to image the induced transmembrane potential using di-4-ANEPPS. The chamber allowed for continuous temperature monitoring using a thermocouple.

electric field pulse was calculated using

$$\Delta T = \frac{\sigma E^2 t}{\rho \Theta} \tag{3.1}$$

where σ is the conductivity of the medium (about 8×10^{-3} mhos/cm for physiologic solutions), E is the applied electric field, t is the time of the exposure, ρ is the density of the medium (about 1 gm/cm^3), and Θ is the specific heat of the medium (about 4.17 J/gm/°C). For the exposure generally used in the protocols, $E = 5$ V/cm for $t = 5$ sec, the temperature rise in the chamber was expected to be about 0.24°C. This was considered to be a negligible amount and no cooling of the chamber was required.

3.5.2 Imaging System

The exposure chamber was mounted on the stage of a Nikon Microphot with phase–contrast and epi–fluorescence capabilities. A Nikon G–2A filter block was used which provided excitation in the range of 510–560 nm, a dichroic mirror passing wavelengths above 580 nm and reflecting those below, and a barrier filter passing wavelengths above 590 nm. Illumination for the fluorescent optics was provided by a 75 W Xenon arc lamp. Various Nikon objectives in the range of 4× to 100× were used. Figure 3.7 shows a properly–stained cell observed under light and fluorescence optics.

It was determined that cells were sensitive to prolonged excitation of the dye. They hypercontracted after 5–10 minutes of continuous excitation when using the full power of the Xenon lamp. Therefore, it was necessary to limit the power of the excitation with the use of a filter (ND4). As a result, properly stained cells had a relatively low fluorescence intensity. A Hamamatsu video–intensified camera connected to a Hamamatsu C1966 digital image processor (Hamamatsu City, Japan) was used to collect images in standard video format. This set–up produced grainy and noisy, but adequate, images.

To decrease the effects of the noise, images were processed using the jumping or rolling average feature of the Hamamatsu Image Processor. Typically a 4–16 frame

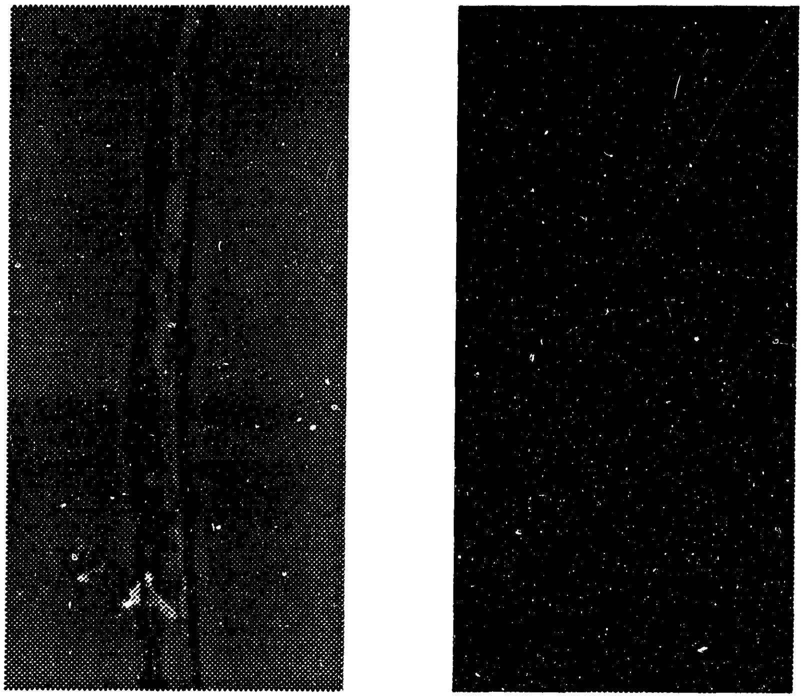

Figure 3.7: Skeletal muscle cell stained with di–4–ANEPPS observed under 10× phase contrast and fluorescence optics.

average was specified. The processed image that was recorded by a high resolution 3/4 inch format videocassette recorder (Panasonic model 9240–XD).

3.5.3 Protocols

Cells in DMEM were stained with di–4–ANEPPS using the protocol described in Section 3.2.2. Experiments were performed using cells in isotonic and hypertonic solutions, prepared as described in Section 3.3. To obtain cells in hypertonic solution, the DMEM in a dish of cells stained with di–4–ANEPPS was replaced a little at a time with hypertonic solution until the color of the cell suspension changed from red (the color of the DMEM) to clear (the color of the hypertonic solution).

Before cells were placed in the chamber, a thin coating of Cell–Tak (BioPolymers, Farmington CT), an adhesive protein derived from the marine mussel, was deposited on the glass window of the chamber by spreading a 5 μl volume evenly over the surface. When the Cell–Tak dried, the window was rinsed with dionized, distilled water. To place cells in the chamber, an instrument made from a flame–pulled Pasteur pipette (to a tip diameter of a few hundred microns), a length of rubber tubing, and a thumb screw suction device was used. Using this tool, individual cells which had incorporated di–4–ANEPPS could easily be removed from a petri dish along with a small volume of fluid and transferred to the exposure chamber. Cells were quickly aligned using a flame–sealed micropipette before they settled to the bottom and adhered to the window. Several were transferred for each trial because when the coverslip was set in place, fluid motion would cause many cells to move. The Cell–Tak did not adhere cells very reliably in this protocol. After the wells on each side of the window were filled with medium, the coverslip was anchored in place with a thin coating of vaccuum grease around the edges.

For each experiment, a cell or section of a cell of interest was monitored and video–recorded for a short time under light and then fluorescence optics. Then, a prescribed voltage was applied to the chamber for 5 or 10 seconds. Repeated field applications were separated by about 30 seconds.

The models described in Section 2.1 were used to approximate the applied voltage required to induce a maximum transmembrane potential of 100–200 mV, a range considered to be too low to significantly damage the cell by membrane electrical breakdown. For cells aligned parallel to the applied electric field, a voltage of 10 V was applied, leading to a field in the chamber of about 5 V/cm. For cells aligned perpendicular to the field, voltages in the range of 25–100 V were applied, leading to fields of about 12.5–50 V/cm.

For applications of 10 V, heating was measured to be less than 1°C (as predicted by Equation 3.1), so no cooling was required. For larger voltage applications, shorter exposure times (1–2 seconds) were used to limit temperature rises to under 5°C. This was found to be much simpler than using the cooling capabilities of the chamber. Since the experiments were performed at room temperature, at no time did the temperature in the chamber rise above physiologic temperature (37°C).

Induced transmembrane potentials were observed as changes in the fluorescence intensity of the di-4-ANEPPS molecules incorporated in the membrane. Using the known sensitivity of the dye (about 8–10% change per 100 mV induced), the intensity measurements were converted to induced potentials. The results are presented and discussed in Section 4.1.

3.6 Electrical Experiments

The experimental system used to observe the response of isolated skeletal muscle cells to intense electric field pulses is illustrated in Figure 3.8. The system allowed real-time observation of the cells during pulse application, as well as video-recording and digital image storage and analysis.

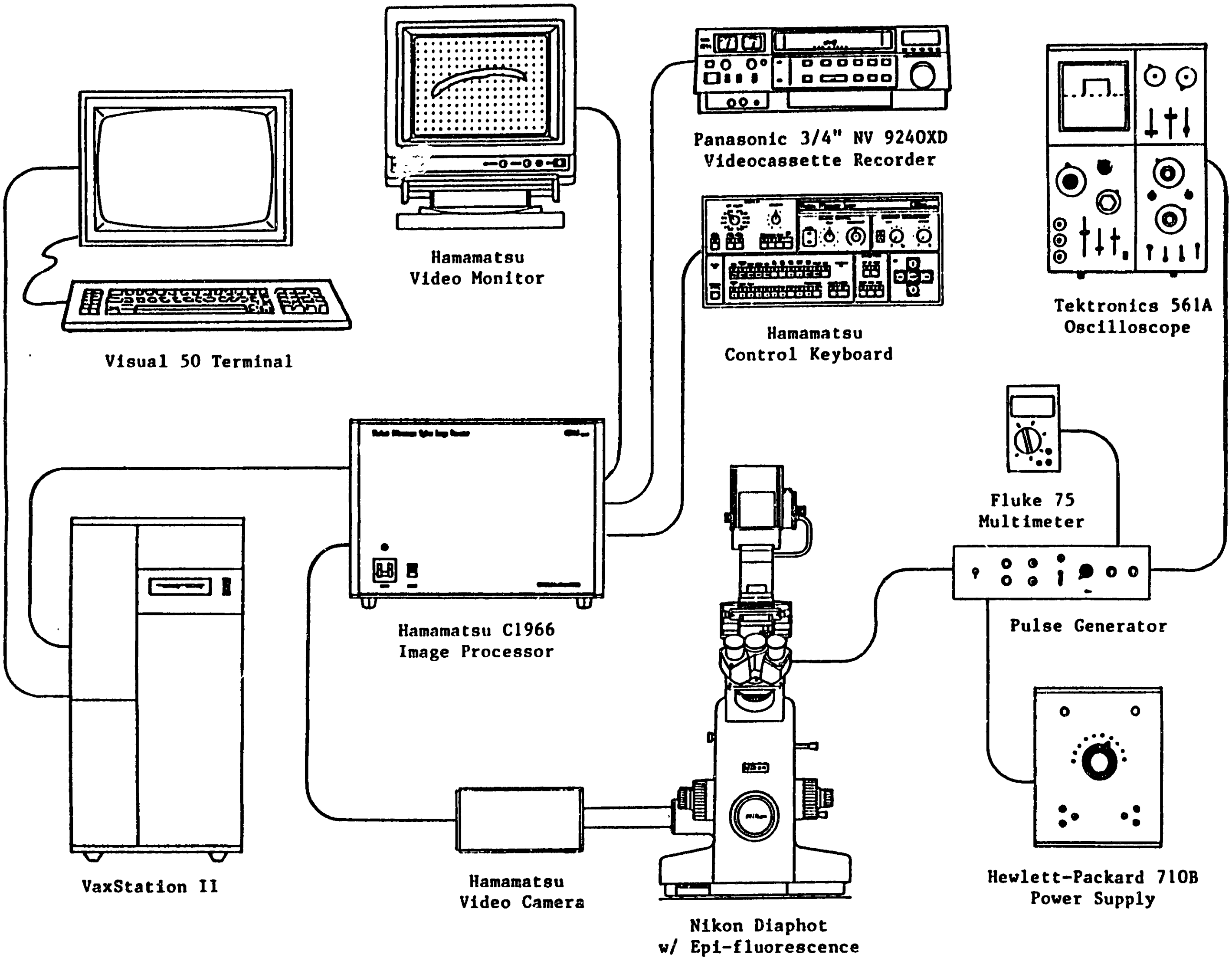

Figure 3.8: System designed for the application of short–duration, high–intensity electric field pulses to isolated skeletal muscle cells. The system allowed real–time observation of the cells during pulse application, as well as video–recording and digital image storage and analysis.

3.6.1 Exposure Chamber

An electric field exposure chamber was designed and built to mount on a microscope and allow observation of cells during electric field pulse application. The chamber is illustrated in Figure 3.9. To construct the chamber, a 10 × 10 mm square hole was cut through a 7 mm thick polysulfonate block. A glass reticle ruled with a 100 μm square grid was mounted on the bottom surface of the block using Silastic brand medical grade silicon elastomer (Dow Corning) to produce a water–tight seal. Platinum electrodes were mounted on opposite ends of the chamber. Platinum was chosen for its resistance to corrosion. Stainless steel electrodes were found to quickly form an oxide layer with use, which would eventually block conduction entirely.

For monitoring of the temperature of the medium in the chamber, a 2–mm diameter precision thermistor element (Omega model 44033, Stamford, CT) was mounted in one side wall of the chamber so that the epoxy–coated tip extended 2 millimeters into the chamber midway between the electrodes. The thermistor had a maximum operating temperature of 150°C and a specified time constant on the order of seconds (time to indicate 63% of a newly impressed temperature). The thermistor leads were connected to a multimeter (Fluke model 75, Everett WA) and the measured resistance (2252 Ω at 25°C) was used to determine the temperature using the standardized resistance temperature curve (provided by Omega) within ±0.1°C.

The expected temperature rise in the chamber during the application of an electric field pulse can be calculated using Equation 3.1. For the maximum exposure used in the protocols, $E = 300$ V/cm and $t = 4$ msec. This leads to a temperature rise per electric field pulse of about 0.7°C.

To determine the temperature rise associated with the series of pulses used in the experiments, the temperature in the chamber was monitored in control experiments with twenty 4 msec 300 V/cm pulses, spaced at 15 seconds. The results are plotted in Figure 3.10. As indicated the total temperature rise was approximately 5°C. Cooling

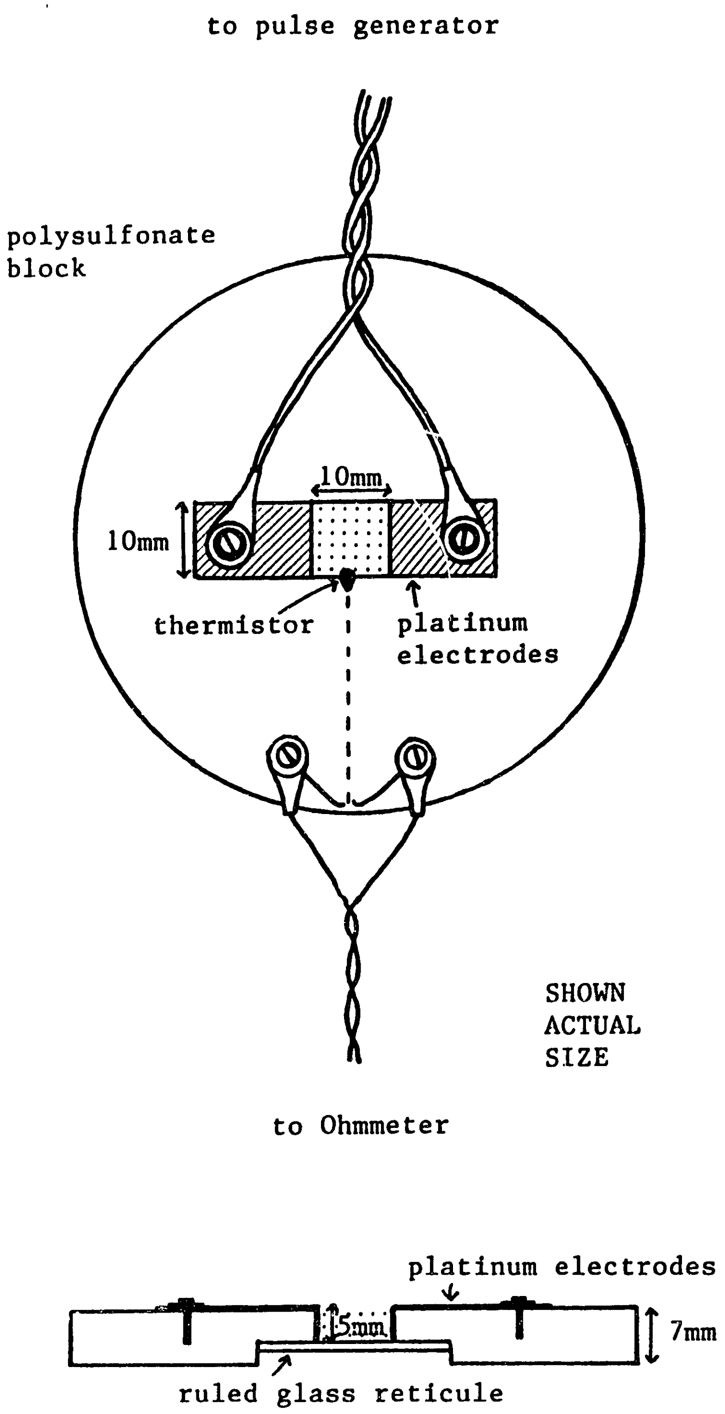

Figure 3.9: Chamber used to expose isolated skeletal muscle cells to brief high-intensity electric field pulses. The transparent glass bottom permitted real-time observation of cells with a microscope. The thermistor was used to monitor the temperature in the chamber throughout experimental protocols.

between pulses clearly helped minimize the rise. Since the experiments were performed at room temperature, the temperature in the chamber was always below the physiologic temperature of 37°C.

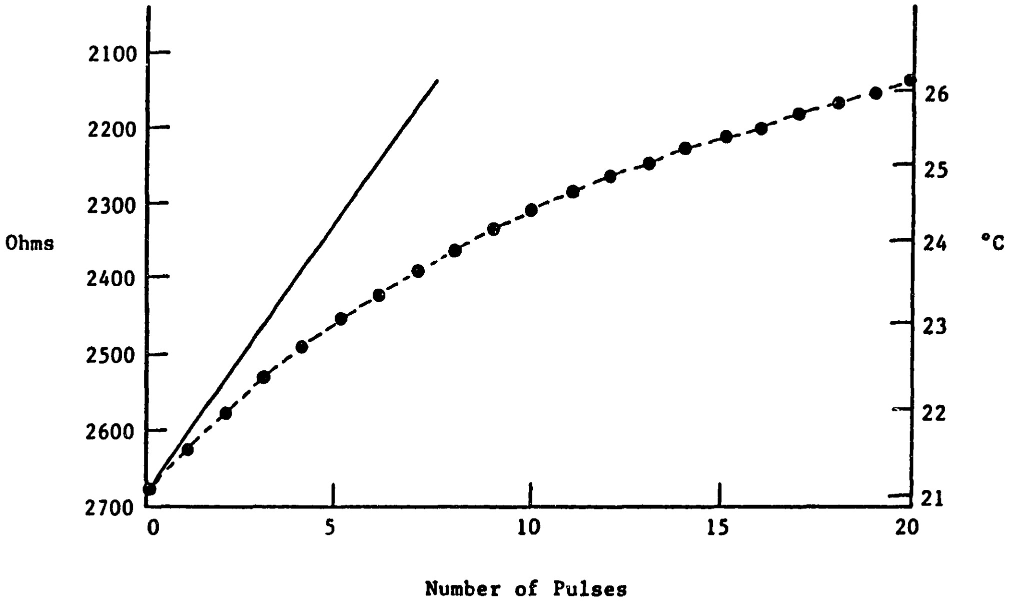

Figure 3.10: Measured temperature rise in exposure chamber during maximum exposure (300 V/cm 4 msec pulses, one every 15 seconds). The left vertical axis indicates the measured thermistor resistance, the right vertical axis converts these readings into temperature using the conversion curve provided by Omega. The dots indicate measured data; the solid line is the rise predicted by Equation 3.1 in the absence of cooling.

The current flow through the media leads to a pH gradient in the chamber. This is caused by chemical reactions at the electrodes. At the positive electrode, electrons are generated by the breakdown of water, releasing hydrogen ions and oxygen gas. Thus the region near the positive electrode becomes acidic. At the negative electrode, electrons are combined with water to form hydrogen gas and hydroxyl ions. Thus the region near the negative electrode becomes basic. These electrode reactions are necessary for the current flow to be continuous between the two kinds of conductors, the metallic electrodes and the ionic media.

In preliminary experiments using twenty 4 msec 300 V/cm pulses, it was demonstrated using litmus paper that pH changes of about 2–3 pH units adjacent to the electrodes occurred. When the media in the chamber was supplemented with 100 mM HEPES buffer or when the polarity of the electrodes was switched after every four pulses, the changes at the electrodes fell to less than 1 pH unit. These changes were not considered important, since in the protocols cells were placed near the center of the chamber where no significant pH changes occurred.

3.6.2 Pulse Generator

A custom designed and built pulse generator was used to apply electric field pulses of 50–300 volt/cm magnitude and 0.1–10.0 msec duration to the exposure chamber. Figure 3.11 shows the circuit diagram for the pulse generator, which was powered by a 50–350 V power supply (Hewlett Packard model 710B, Palo Alto).

The generator was designed with ports for continual monitoring of the voltage across the capacitors using a multimeter (Fluke model 75) and for scoping the current or voltage delivered to the chamber during pulse application (Hewlett Packard oscilloscope type 561A). Assuming a conductivity of 0.8×10^{-3} mhos/cm for the physiologic medium in the chamber, the resistance of the 1 cm×1 cm×0.5 cm ($\ell \times w \times d$) chamber was 250 Ω. Preliminary measurements indicated that applied 300 V pulses across the chamber resulted in currents of 1.0–1.5 A in the chamber, which is consistent with Ohm's law. Thus, it was concluded that any impedance drops across the electrodes due to electrode polarization did not contribute significant error.

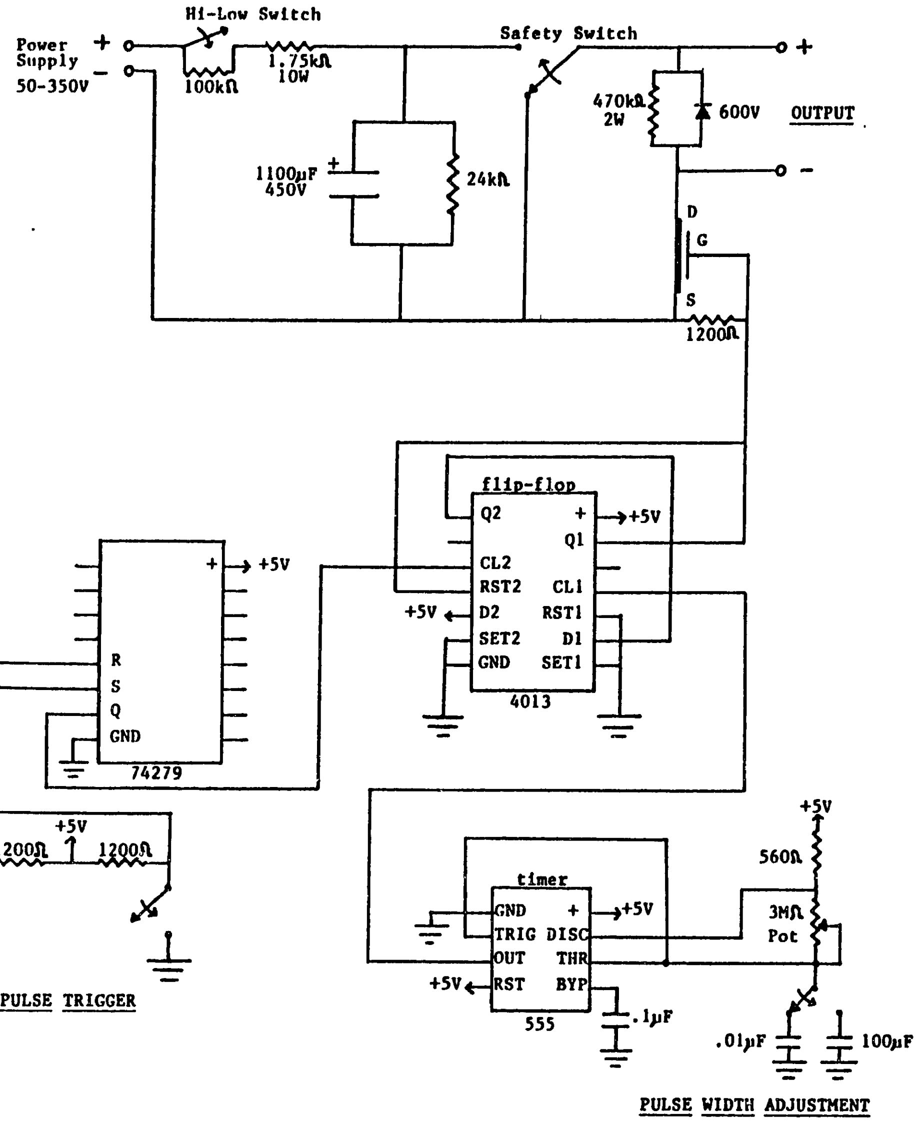

Figure 3.11: Custom designed and built pulse generator used to apply electric field pulses of 50–300 V/cm magnitude and 0.1–10.0 msec duration to the exposure chamber.

3.6.3 Imaging System

The chamber was mounted on the stage of a Nikon Diaphot inverted microscope with phase–contrast, Nomarski, and epi–fluorescence capabilities. A standard Nikon filter block (B–2A) for use with fluorescein was used which provided excitation in the range of 470–490 nm, a dichroic mirror passing wavelengths above 510 nm and reflecting those below, and a barrier filter passing wavelengths above 520 nm. Illumination for the fluorescence optics was provided by a 100 W mercury arc lamp.

A Hamamatsu (Hamamatsu City, Japan) chalnicon camera head connected to a Hamamatsu C1966 digital image processor was used to collect images in standard video format. Video recordings were made using a high resolution 3/4 inch format video recorder (Panasonic model 9240–XD).

3.6.4 Protocols

Protocols were designed to observe and quantify the physical damage to isolated skeletal muscle cells caused by exposure to brief electric field pulses. All experiments were performed at room temperature.

To place cells in the chamber, an instrument made from a flame–pulled Pasteur pipette (to a tip diameter of a few hundred microns), a length of rubber tubing, and a thumb screw suction device was used. Using this tool, individual cells could easily be removed from a petri dish along with a small volume of fluid and transferred to the exposure chamber.

In experiments using single cells, cells were always placed halfway between the electrodes to minimize the effects of electrode products and pH changes. They were aligned either parallel or perpendicular to the applied electric field. It was not very hard to deposit cells in the center of the chamber in the desired alignment, although cells that were not correctly placed could be moved by use of a flame–sealed micropipette to create fluid motion near the cell.

In most experiments, a pulse duration of 4 msec was used. This value was chosen for its relevance to electrical injury. It is the time during which the voltage in a 60 Hz signal is above its root–mean–square value, occurring twice every cycle as illustrated in Figure 3.12. Thus the 4 msec square pulse roughly models the "pulses" of a sinusoidal signal.

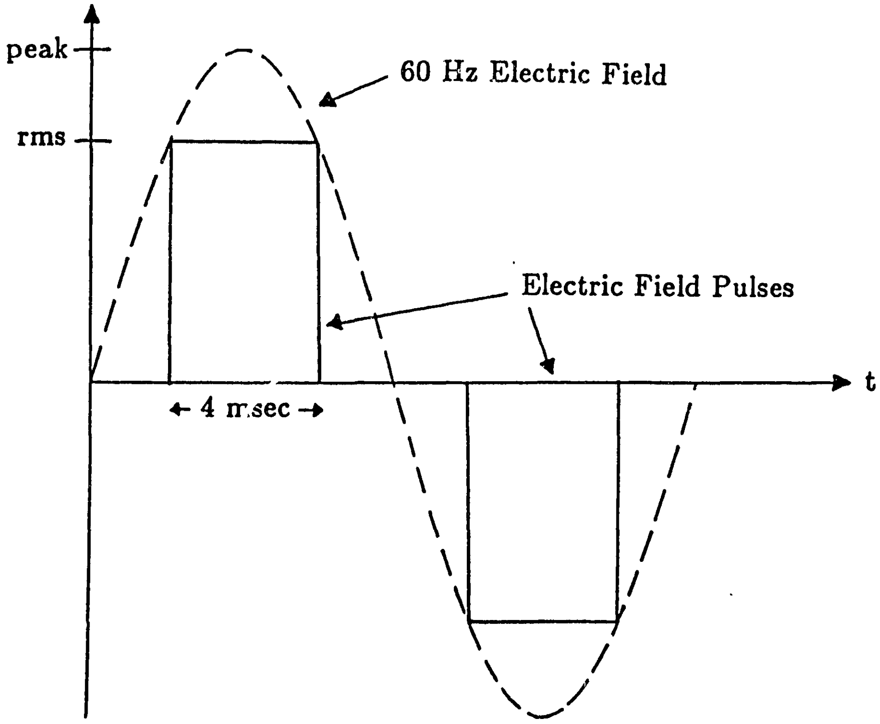

Figure 3.12: A pulse duration of 4 msec was used in most experiments due to its relevance to electrical injury. It is the time during which the voltage in a 60 Hz signal is above its root–mean–square value, which occurs twice every cycle.

Cytomorphological Changes

Experiments were performed to observe the cytomorphological changes induced by brief electric field pulses for cells bathed in a physiologic, isotonic solution. For each experiment, a single cell was transferred to the PBS–filled chamber and aligned. Cells damaged in the process would hypercontract, making it easy to ensure that only undamaged cells were used in the experiments. Pulses of magnitude 50–300 V/cm magnitude and 0.1–4.0 milliseconds were applied. The cellular response was observed under 10× phase contrast optics on the monitor and recorded on tape for further analysis. In selected experiments, cells loaded with carboxyfluorescein (as described in Section 3.2.1) were observed under 10× fluorescence optics in an effort to detect any obvious dye leakage. The results are presented and discussed in Section 4.2.1.

Membrane Permeability Changes

Experiments were performed to demonstrate and quantify changes in the diffusive permeability of skeletal muscle cell membranes induced by brief high–intensity electric field pulses. These experiments involved use of cells loaded with carboxyfluorescein (as described in Section 3.2.1) and paralyzed by exposure to a hypertonic solution (as described in Section 3.3). Figure 3.13 shows a cell loaded with carboxyfluorescein in hypertonic solution aligned in the chamber prior to the start of an experiment. Membrane permeability changes were observed as a rate of dye loss greater than established baseline values.

Qualitative Studies: A protocol was developed to examine many cells of different alignment in the chamber during a given exposure. In this way, the amount of dye loss could be compared visually between cells and patterns could be observed. For these trials, the DMEM in a dish of cells labelled with carboxyfluorescein was replaced a little at a time with hypertonic solution until the cell suspension changed from red (the color of the DMEM) to clear (the color of the hypertonic solution). Then, cells were transferred several at a time to the chamber until it was filled with solution. The chamber was examined under the microscope. Typically 25–50 cells were randomly placed throughout the chamber. Position and alignment of cells was adjusted using a flame–sealed micropipette so that many cells were in the center of the chamber aligned

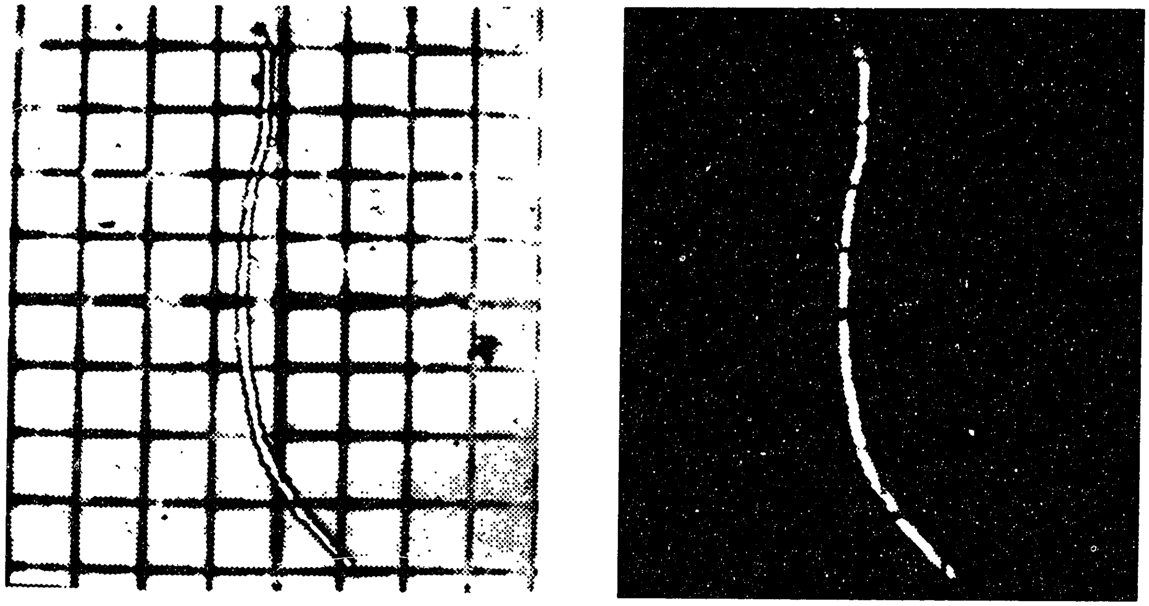

Figure 3.13: Skeletal muscle cell loaded with carboxyfluorescein in hypertonic solution aligned in the electric field pulse exposure chamber under light and fluorescence optics. The grid markings represent 100 μm.

either parallel or perpendicular to the electric field.

A video recording of the location, orientation, and condition of the cells in the chamber was made as the chamber was slowly scanned using 10× light optics and then 10× fluorescence optics. Digital images were stored of 10–15 particularly well-positioned fluorescent cells. Fifteen minutes later, the chamber was scanned again under fluorescence optics and images were stored as before. By this time any damaged cells had lost a large amount of dye and their decrease in intensity was noticed. Thus, only healthly cells were studied further.

After the initial examinations of the cells, a specified protocol of electric field pulses was delivered to the chamber. In most experiments, twenty 4 msec pulses of 150, 200, 250, or 300 V/cm magnitude were applied. Pulses were always separated by 15 seconds. Fifteen minutes after the application of the pulses, the chamber was scanned under fluorescence optics and images of the selected fluorescent cells were stored. This was repeated every fifteen minutes for at least one hour. After the completion of the experiment, the videotape and/or the stored digital images were reviewed to determine what effect, if any, the electric field pulses had on the fluorescence intensity of the cells. The results are presented and discussed in Section 4.2.2.

Quantitative Studies: Experiments were performed with single cells to quantify the changes in fluorescence intensity associated with exposure to electric field pulses. For each trial, a cell from a petri dish of cells in DMEM loaded with carboxyfluorescein was transferred to the exposure chamber which was filled with hypertonic solution. The cell was positioned in the center of the chamber and aligned either parallel or perpendicular to the field as precisely as possible. Estimates of the length and diameter of the cell were made using the grid on the glass reticule.

The cell was exposed to the optical excitation for approximately ten seconds once every minute, at which time a digital image of the fluorescent cell was stored. After

10 minutes, the application of electric field pulses commenced. Usually twenty 4 msec pulses of 200-300 V/cm amplitude were applied, one every 15 seconds. Images were stored at one-minute intervals during and after the pulse application until a total elapsed time of 30 minutes was reached. The 31 stored images were analyzed, and the average cell intensity as a function of time was determined. A membrane permeability increase appeared as a rate of intensity decrease beyond the baseline established during the first 10 minutes of monitoring. The results are presented and discussed in Section 4.2.2.

3.7 Thermal Experiments

The experimental system used to examine the effects of elevated temperatures on isolated skeletal muscle cells is illustrated in Figure 3.14. The system allowed real-time observation and video-recording of cells during carefully-controlled thermal exposures. The system is described in detail in Cosman et al. (1989) and Cosman (1983).

The system was set up in a lab remote from that used for the electrical experiments, and therefore the Hamamatsu image processing system was not available for real-time use in the experiments. All experiments were videotaped for analysis at a later time.

3.7.1 Exposure Chamber

The chamber used to control the temperature of the cells is illustrated in Figure 3.15. The chamber was heated from below with a transparent resistive element (tin oxide on glass) and cooled with a flow of nitrogen gas under the resistive element. A copper-constantan foil thermocoupie (RdF Corp., Hudson, NH) was sandwiched between the heating element and a glass window above. A thin film of mineral oil was used to affix a sapphire window above the glass window. Cells were placed on the sapphire and a coverslip was set down on top, held in place with vaccuum grease. Sapphire has broad band optical transparency and a very high thermal conductivity which reduced

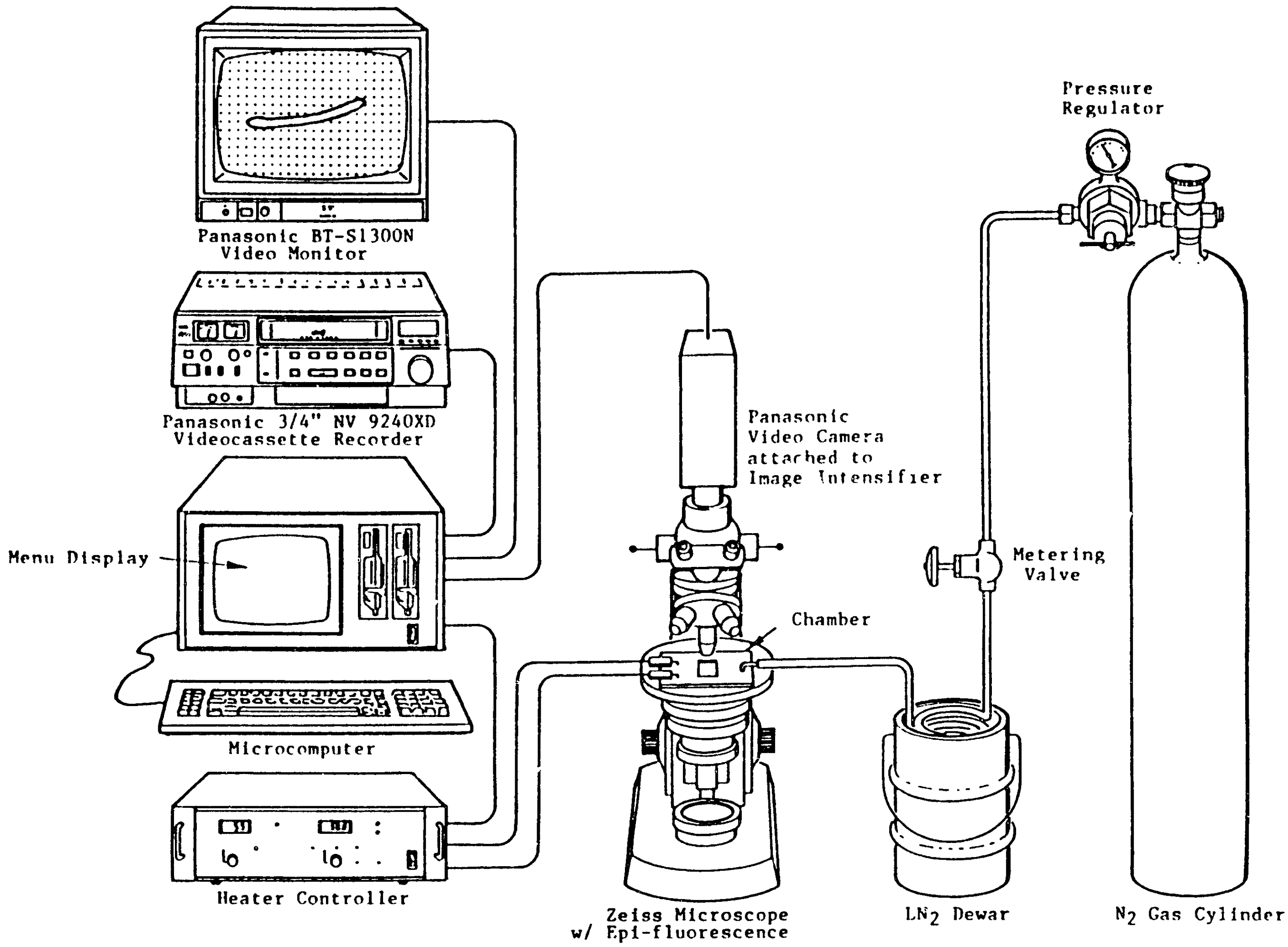

Figure 3.14: System used to observe the response of isolated skeletal muscle cells to elevated temeratures. The system allowed real-time observation of cells during carefully-controlled thermal exposures, as well as video-recording of experiments for later analysis. (Adapted from Cosman et al., 1989.)

thermal gradients to a maximum of 0.1°C/mm.

3.7.2 Temperature Control System

Gaseous nitrogren, cooled by passage through a coil immersed in liquid nitrogen, flowed through the chamber at a constant rate. A heater controller system used feedback from the thermocouple in the chamber to adjust the power in the heating element to counteract the cooling and thus maintain the cells at a specified setpoint temperature.

Menu–driven temperature control software running on a microcomputer allowed temperature protocols to be specified in one of two ways: a series of linear intervals defined by their heating or cooling rates and their durations, or linear intervals defined by their durations and final temperatures. The program used this information to generate mathematically the time–varying temperature setpoints, which were converted to an analog voltage and sent to the heater controller.

The heater controller displayed a temperature obtained from a linear conversion of the thermocouple voltage. The controller then corrected this temperature estimate using the known non–linear properties of the thermocouple (supplied by the manufacturer). The corrected temperature was used by the feedback control algorithm and was also sent to the video monitor for display.

Figure 3.16 shows the temperature readings of the heater controller and the video monitor in response to a user–specified setpoint temperature. Unfortunately, the software was not programmed to display temperatures over 50°C on the monitor. As indicated, it was the corrected temperature (displayed by the monitor) that the heater controller attempted to make equal to the input setpoint.

A calibration of the system's temperature measurements to the actual chamber temperature was performed using Tempilstik temperature indicators (60630 series, VWR Scientific, San Fransisco, CA). These indicators melt at a temperature within 1% of their stated melting temperatures in degrees Fahrenheit. Four Tempilstiks with

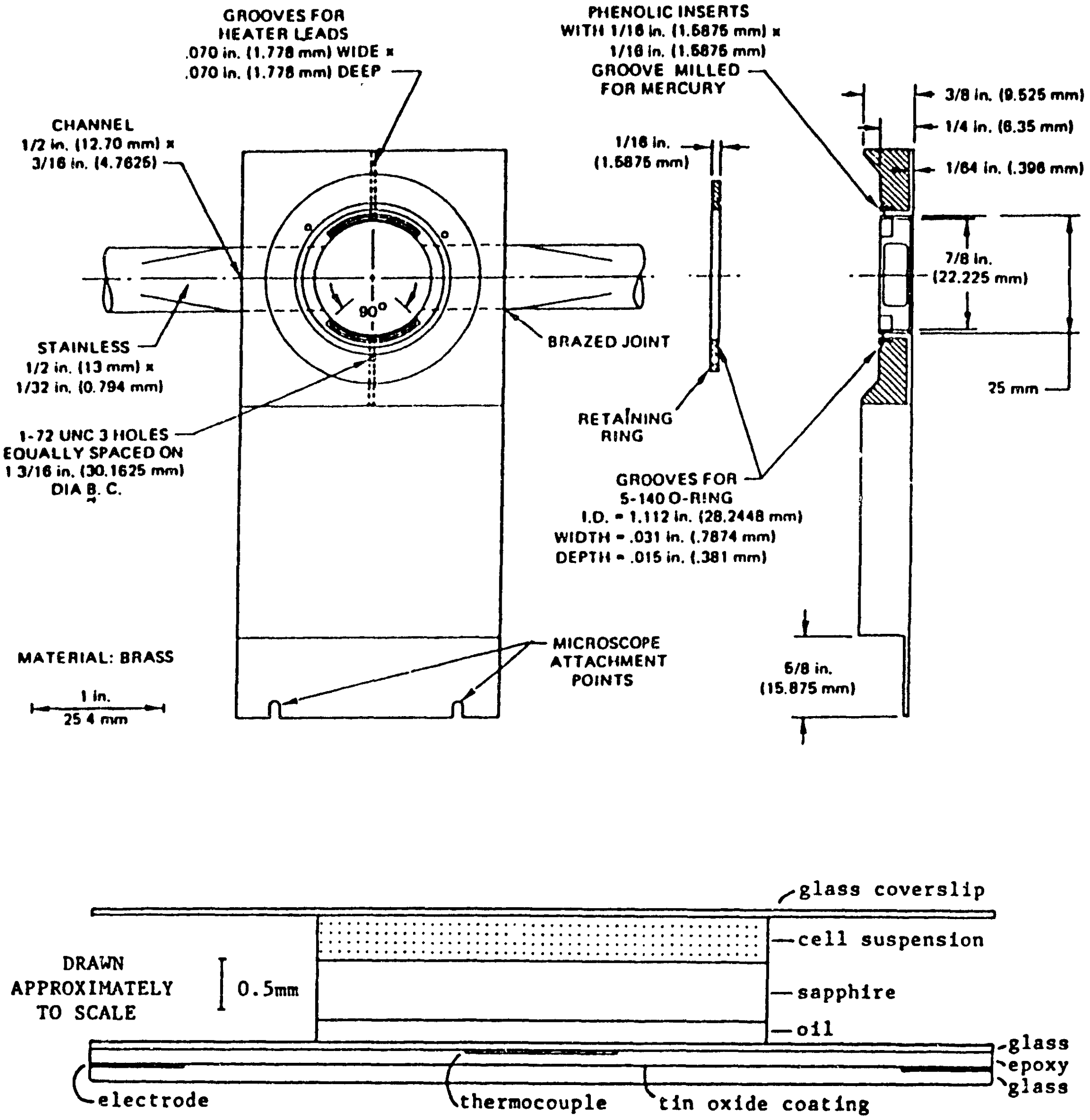

Figure 3.15: Chamber used to expose isolated skeletal muscle cells to carefully-controlled temperature elevations. A flow of cooled nitrogen gas cooled the chamber. Feedback from the thermocouple was used to control the resistive heater. The transparent windows allowed real-time observation of the cells. The high thermal conductivity of the sapphire reduced thermal gradients. (Adapted from Cosman, 1983.)

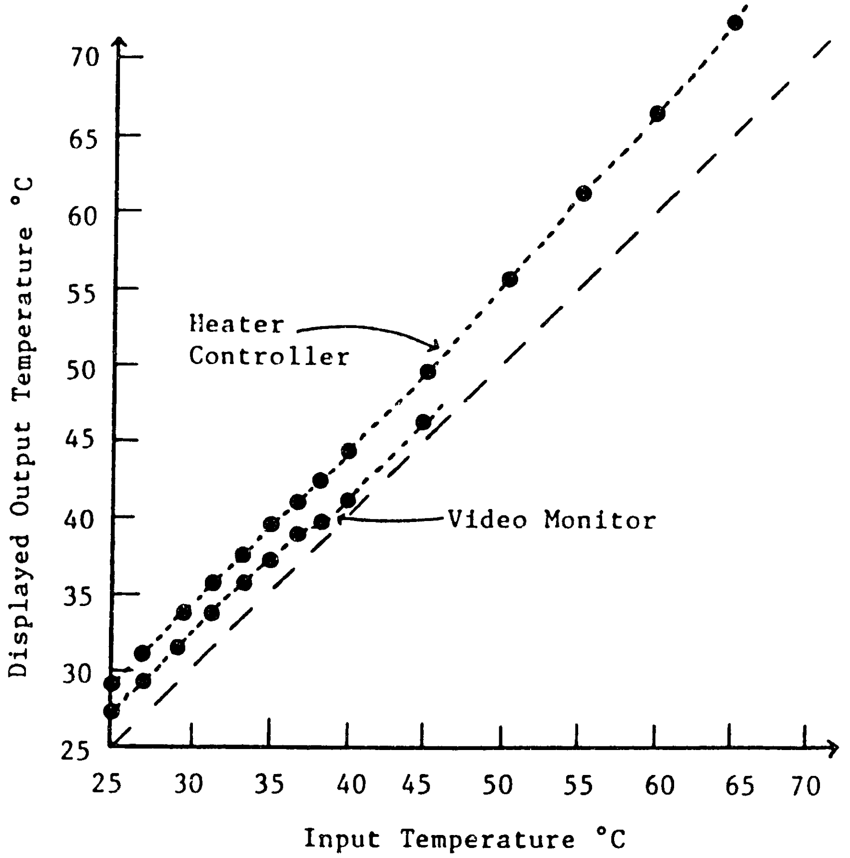

Figure 3.16: Displayed temperatures as a function of user-specified setpoint temperature. The video monitor displayed a corrected temperature computed from the heater controller displayed temperature using the known non-linear behaviour of the thermocouple.

melting temperatures of 37.8±.6°C, 45.0±.6°C, 55.0±.7°C, and 65.6±.8°C were used. For each trial, a small amount of the Tempilstik was shaved off with a razor blade and put in the chamber. The chamber was heated until the substance liquified and then cooled down until crystallization occurred. This created a smooth layer in the chamber. Then the temperature was raised slowly (2–10°C/minute) until melting was observed. The melting temperature as indicated on the heater controller and on the video monitor was recorded. Two trials were performed using each Tempilstick.

With the data obtained using the Tempilstiks, the readings of the temperature controller and the video monitor were calibrated. The results are shown in Figure 3.17 which shows the temperature in the chamber as measured using the Tempilstik as a function of the user-specified setpoint temperature. As shown, temperatures appear to be controlled to within ±1°C.

3.7.3 Imaging System

The exposure chamber was attached to a Zeiss research microscope with epi-fluorescence capabilities. For fluorescence observations, a standard Zeiss FITC filter block for fluorescein dyes was used. A 200 W Mercury arc lamp provided the illumination for the fluorescence excitation. Typically, cells were observed using 8× light or fluorescence optics. A microchannel intensifier (Electrophysics Corp., Nutley, NJ) was attached between the video port of the microscope and a Panasonic videocamera to provide gain in the fluorescence experiments. The camera was connected to the monitor (Panasonic model BT-S1300N) and the 3/4 inch video recorder (Panasonic model 9240-XD).

3.7.4 Protocols

Cytomorphological Changes

Several protocols were used to examine the cytomorphological changes induced by thermal stimuli. Cells in isotonic DMEM were transferred to the exposure chamber

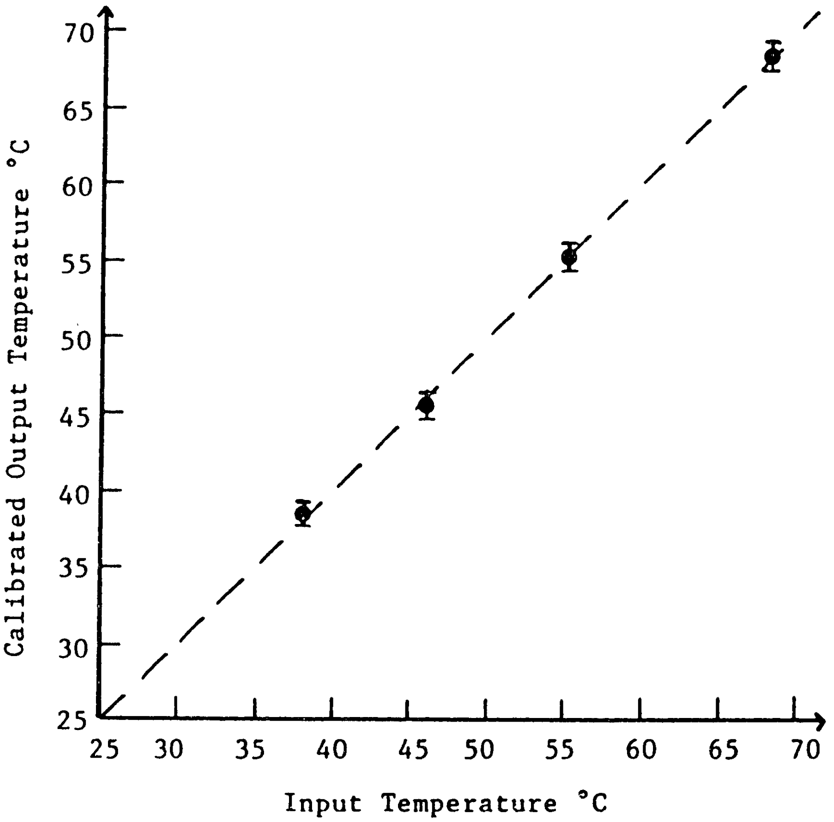

Figure 3.17: Chamber temperature as a function of user-specified setpoint temperature, calibrated using Tempilstik temperature indicators.

using a suction device similar to that used in the electrical experiments. The cover slip was set in place, and the chamber was attached to the microscope stage.

In the simplest experiments, the temperature in the chamber was raised from room temperature at a rate of either 1°C/min or 30°C/min to a final temperature in the range of 37–70°C. Cells were held for several minutes at the final temperature.

In another protocol, cells were raised in two–degree increments from room temperature to 50°C. Each temperature was held for one minute before the next increase.

The final protocol was a control for the electrical experiments, where the cells were subjected to small but rapid temperature jumps. To allow observation of the effects of such jumps, cells were stepped from room temperature to temperatures in the range of 30–40°C at a rate of over 1000°C/min (the maximum possible with the system). The cells were cooled back down to room temperature over a period of 15 seconds, and the heat step was repeated. In each trial, 10–20 heat steps were applied. While the rate of heating could not be made to match that occuring in the electrical experiments, the magnitude of the total temperature excursion was much greater than that predicted to occur in the electrical experiments (see Section 3.6.1). The results are presented and discussed in Section 4.3.1.

Membrane Permeability Changes

In preliminary experiments, it was discovered that isolated rat skeletal muscle cells hypercontracted in response to temperatures of 45°C and above. Therefore, in order to perform fluorescence experiments paralleling the electrical protocols, cells were paralyzed by exposure to hypertonic solutions prepared as described in Section 3.3.

For each trial, a cell from a dish of cells loaded with carboxyfluorescein (as described in Section 3.2.1) was transferred to a dish of hypertonic solution. The cell was then transferred to the chamber, the coverslip was set in place, and the chamber was attached to the microscope. The gain of the intensifier was increased, if necessary, to produce an image of the fluorescent cell of good contrast.

The videotape recorder was set to begin recording, and the cell was monitored at room temperature for 5 minutes to establish baseline levels of cell intensity loss due to natural leakage and bleaching. Then, the temperature was raised in 5 seconds to temperatures of 37, 45, 50, 55, or 60°C. The cell was monitored until it lost all or nearly all fluorescence intensity. The videotapes of the experiments were used to obtain digitized images of the cell intensity at regular time intervals, and the image processing software was used to examine the time dependence of the intensity loss. The results are presented and discussed in Section 4.3.2.

It was important to know if the temperature alone has any effect on the fluorescence intensity of the dye. To answer this question, the chamber was filled with media taken from a dish of cells that had been loaded with carboxyfluorescein several hours earlier. The media contained a large concentration of carboxyfluorescein that had diffused from the cells, and thus fluoresced brightly. The fluorescence intensity of the media was monitored for 5 minutes at room temperature and then for 15 minutes at 60°C. No intensity change was detected.

Chapter 4

Results

In this chapter, the experimental results will be presented and discussed. From the data, the thresholds for skeletal muscle cell membrane damage due to thermal and electrical mechanisms will be determined. In the next chapter, this information will be used to predict patterns of tissue damage in typical cases of electrical injury.

4.1 Imaging the Induced Transmembrane Potential

The potential-sensitive dye di-4-ANNEPPS was used to image the induced transmembrane potential for cells aligned parallel to an applied electric field exposed to both isotonic and hypertonic solutions. Figure 4.1 shows the average percent change of the dye intensity at the ends of cells when an electric field of approximately 5 V/cm was applied for several seconds. The induced transmembrane potential was calculated from the reported response of the dye (about 9% per 100 mV; Gross & Loew, 1989). In 11 trials using cells in isotonic solution, only 1 showed no intensity change. All others exhibited an intensity change of at least 10%. The average for the 11 trials was 10.9%. In 9 trials with cells in hypertonic solution, the greatest intensity change observed was 5%, which occurred in only one cell. More than half showed no intensity change. In order to obtain an average, cells exhibiting a slight, but less than 5%, intensity change were counted as 5%, since the exact value was difficult to resolve. The average for the 9 trials was 2.2%.

The results indicate that exposure of skeletal muscle cells to hypertonic solutions of 3.0-times normal tonicity has a dramatic effect on the magnitude of the induced transmembrane potential. It is proposed that this effect is caused by the extensive internal membrane system of the skeletal muscle cells, particularly the T-tubules and the sarcoplasmic reticulum (see Section 1.3.3). In hypertonic solution, water removal from the cell is expected. This appears to lead to membrane packing or overlap which acts to dramatically increase the cytoplasm resistance to current flow in the longitudinal direction. The relatively large induced transmembrane potentials observed for cells in isotonic solution indicate that these membranes do not prevent current flow under normal circumstances. As will be seen in Section 4.2, the diffusion of carboxyfluorescein is significantly hindered along the long axes of cells bathed in hypertonic solutions, which also suggests that membrane blockages occur at points along the axes. The hypothesis is consistent with the finding of Parker & Zhu (1987) that intracellular calcium transients in frog muscle are significantly diminished in solutions of 3.0-times normal tonicity. As will be shown in Section 4.2, current and diffusion in the radial direction did not appear to be affected, indicating that the regions between the membranes of each sarcomere are not blocked in the process.

The measurements of the induced transmembrane potential for skeletal muscle cells in isotonic solution can be compared to the cable model prediction (see Section 2.1.1). Nominal values for the membrane electrical properties of rat skeletal muscle cells are $r_m = 500\ \Omega\text{cm}^2$ and $c_m = 7\ \mu\text{F/cm}^2$ (Bekoff & Betz, 1977; Kiyohara & Sato, 1967; Dulhunty et al., 1984). In hypertonic solutions, the cells had radii of 10–20 μm and lengths of 500–1000 μm. Using these values, the predicted maximum induced transmembrane potential is 30±10 V per applied V/cm. Thus, an applied field of about 5 V/cm is expected to induce a maximum potential of 150±50 mV for the average

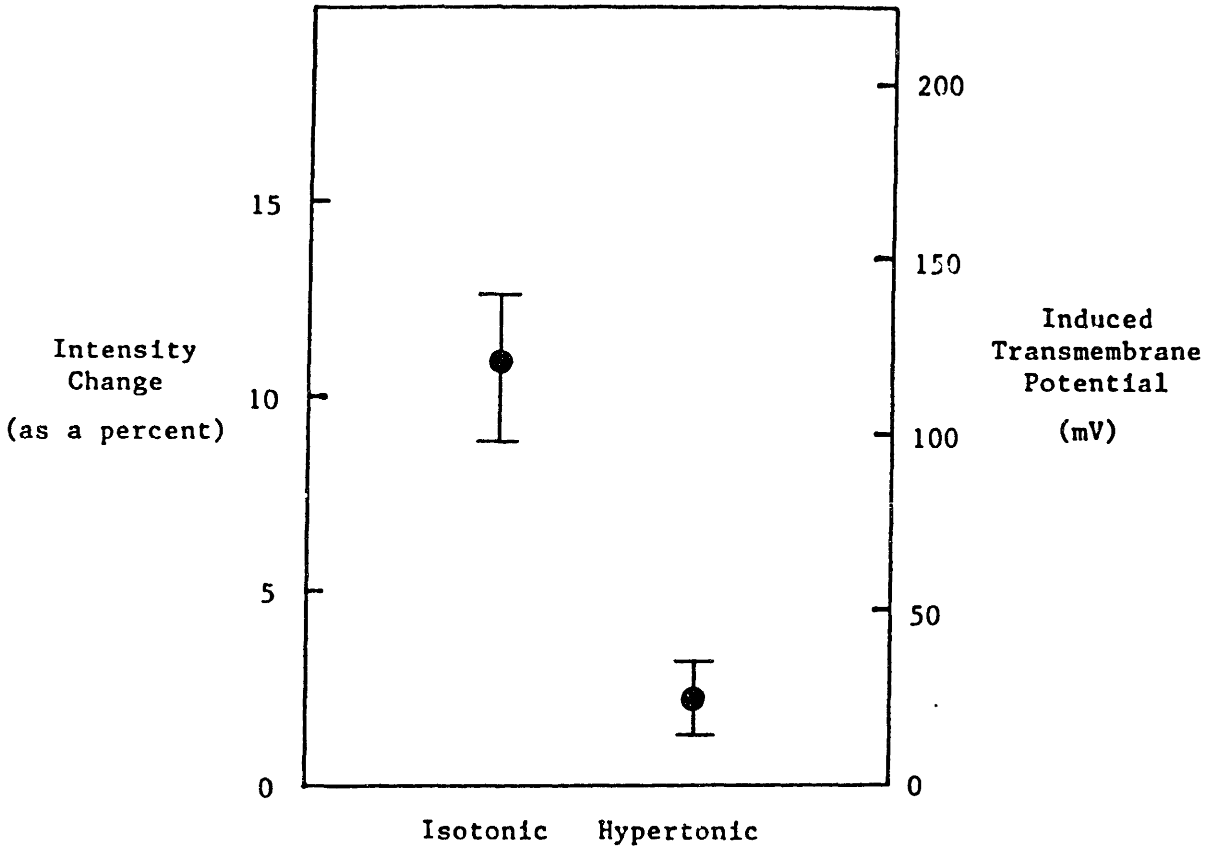

Figure 4.1: Transmembrane potential induced in the ends of isolated skeletal muscle cells aligned parallel to an applied electric field of approximately 5 V/cm as measured by a change in the fluorescence intensity of di-4-ANEPPS incorporated in the membrane. The dye responds with a fluorescence intensity change of about 9% per 100 mV induced. The averages are computed from 9–11 trials. The error bars represent the standard error of the mean.

cell. In isotonic solution, the average induced potential was 120 mV. This is in good agreement with the predicted value, given the uncertainties in the electric field in the chamber, the electrical properties of the cells, the sensitivity of the dye, and the linearity of the imaging system. It thus appears that the cable model derived in Section 2.1.1 provides a good estimate of the induced transmembrane potential for skeletal muscle cells aligned parallel to an applied electric field.

As mentioned in Section 3.5.2, cells stained with di–4–ANEPPS in isotonic solution were particularly sensitive to electric fields when excited with the light source. Since only the ends of the cells were excited (using 40–100× optics) in the preceding experiments, this was generally not a limiting problem. Often, the end under observation would contract a little (for cells in isotonic solution), but usually a measurement could be made before this happened. However, when a lower magnification was used to image the entire cell, this sensitivity was a problem. In this situation, nearly all cells in isotonic solution aligned parallel to the field contracted as soon as 5 V/cm was applied. In over 15 trials, only one completely satifactory observation was recorded. The cell was short (about 600 μm in length). This allowed the entire length to be observed with 10× optics. A smaller induced transmembrane potential is expected in shorter cells and this is probably the reason that the cell did not contract. The fluorescence intensity change in response to a field of about 5 V/cm was measured at regular intervals along the length of the cell. The result is plotted in Figure 4.2. As shown, the variation is approximately linear in the middle of the cell. This agrees with the cable model prediction for short cells (see Figure 2.4). The linear relation breaks down near the ends, however. This may be due to electroporation. As explained in Section 1.3.1, even small induced transmembrane potentials can lead to an increased membrane permeability by increasing the number and size of pores in the membrane, leading to an increased membrane conductivity and decreased induced potential (Powell & Weaver, 1986). This has been demonstrated using sea urchin eggs by Kinosita et al. (1988). For the case shown, the induced transmembrane potential adds to the resting potential on the right end, but subtracts from the resting potential on the left end. Thus, electroporation should be much greater on the right end. As shown in Figure 4.2, the induced potential at the right end is much more limited than that at the left end. Clearly, however, further studies of this kind are required before conclusions can be drawn.

Unfortunately, efforts to image the induced transmembrane potential for cells applied perpendicular to the applied electric field were not successful. The large fields required to induce a potential of about 50–100 mV usually resulted in the collapse of cells in isotonic solution. The fields also caused the cells to electrophorese toward the positive electrode. The intensity of the dye should increase on the side facing the positive electrode and decrease on the side facing the negative electrode when a potential is induced. For this reason, an induced transmembrane potential could not be distinguished from a slight movement of the cell toward the positive electrode.

4.2 Electrical Experiments

4.2.1 Cytomorphological Response

Isolated skeletal muscle cells in isotonic solutions responded dramatically to the application of brief electric field pulses. In one set of experiments, a 0.1 or 1.0 msec electric field pulse was delivered to a cell every 30 seconds, starting at a field intensity of 30 volts/cm, and increasing by 10 volts/cm with each additional pulse up to 300 volts/cm. Typically, a cell would exhibit a strong twitch response at field intensities up to 100 volts/cm. At higher values, the twitching often ceased, possibly due to damage incurred at the lower field strengths. In the highest range of field intensities applied (from about 200 volts/cm to about 300 volts/cm), irreversible contraction and total collapse of the cell along its long axis usually occurred. This response was observed for both pulse durations used, but was more pronounced for the longer dura-

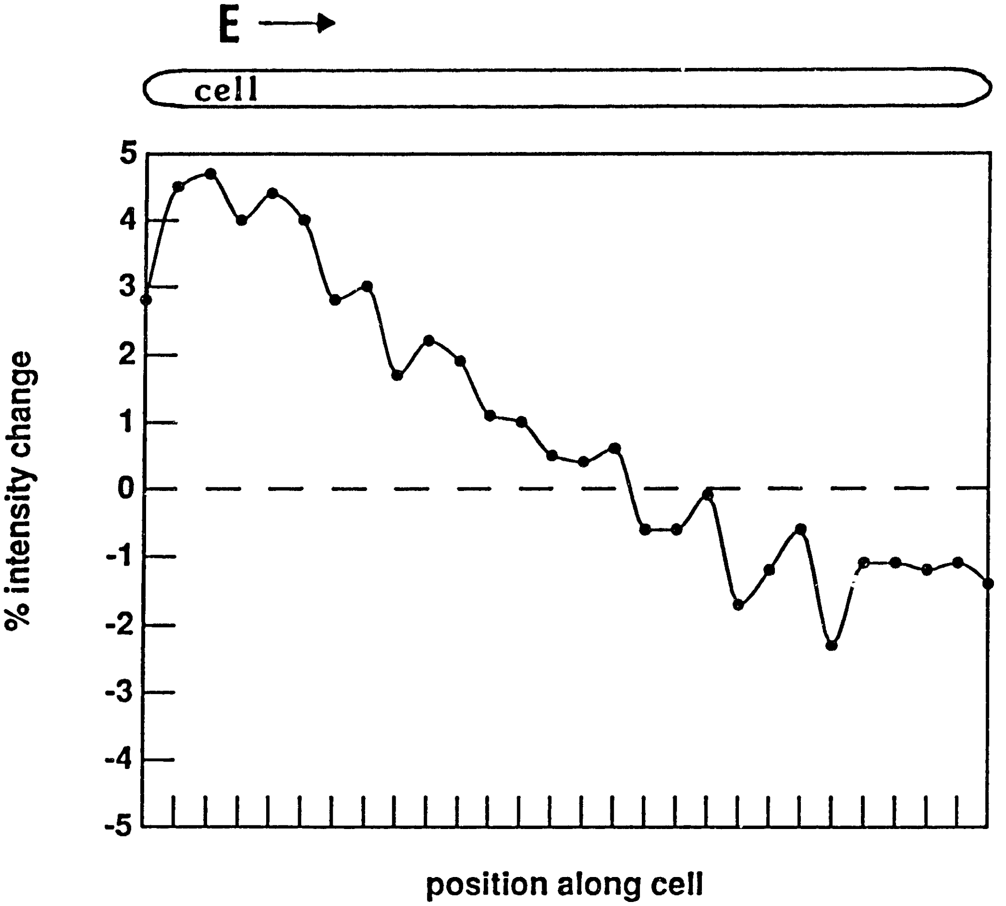

Figure 4.2: Transmembrane potential induced along an isolated skeletal muscle cell in isotonic solution aligned parallel to an applied electric field of about 5 V/cm as observed by the change in the fluorescence intensity of di-4-ANEPPS incorporated in the membrane. The cell was small, about 600 μm in length and about 15 μm in diameter.

tion pulses. Cells aligned perpendicular to the applied electric field exhibited a more forceful twitching response in general than those aligned parallel to the field.

In other experiments, a pulse of 1–4 msec duration and 100–300 V/cm magnitude was applied every 15 seconds until irreversible contraction occurred. A typical experiment is pictured in Figure 4.3. In this case, a cell approximately 1 mm in length aligned perpendicular to the field was exposed to 1 msec 300 volts/cm pulses. Irreversible contraction occurred after only 1 pulse (b). Several more pulses resulted in the total collapse of the cell (c,d). Similar responses were observed in all other trials. The higher field strengths and pulse durations in general caused more rapid cell collapse. As before, a more forceful twitch response was observed in cells aligned perpendicular to the applied field. In some cases, the twitches were so violent that the cell moved out of the field of view.

The twitch response exhibited by cells in isotonic solutions is the natural cellular response to an action potential. Apparently, the perpendicular field is more effective in producing a contraction in isolated cells. This may be due to the fact that the T-tubules are themselves perpendicular to the long axis of the cell. These small channels transmit electrical signals to the inside of the cell, causing the release of calcium from the sarcoplasmic reticulum and triggering the contractile response. This effect may also have to do with the longer charging time of the parallel cells compared to the perpendicular cells (see Sections 2.1.1 and 2.1.2).

The irreversible contraction that occurred indicates some damage to the excitation–contraction coupling mechanism or to the contractile apparatus itself. The total collapse of the cell can only be explained by a breakdown of the contractile proteins, since the intact structure can only contract by about 32% (Mannherz & Holmes, 1982). It is well known that actin and myosin filaments are very sensitive to their environments and that small changes in pH or ion concentration cause their breakdown into globular form (Laki, 1971; Tonomura, 1973; Lapanje, 1978). These changes are expected

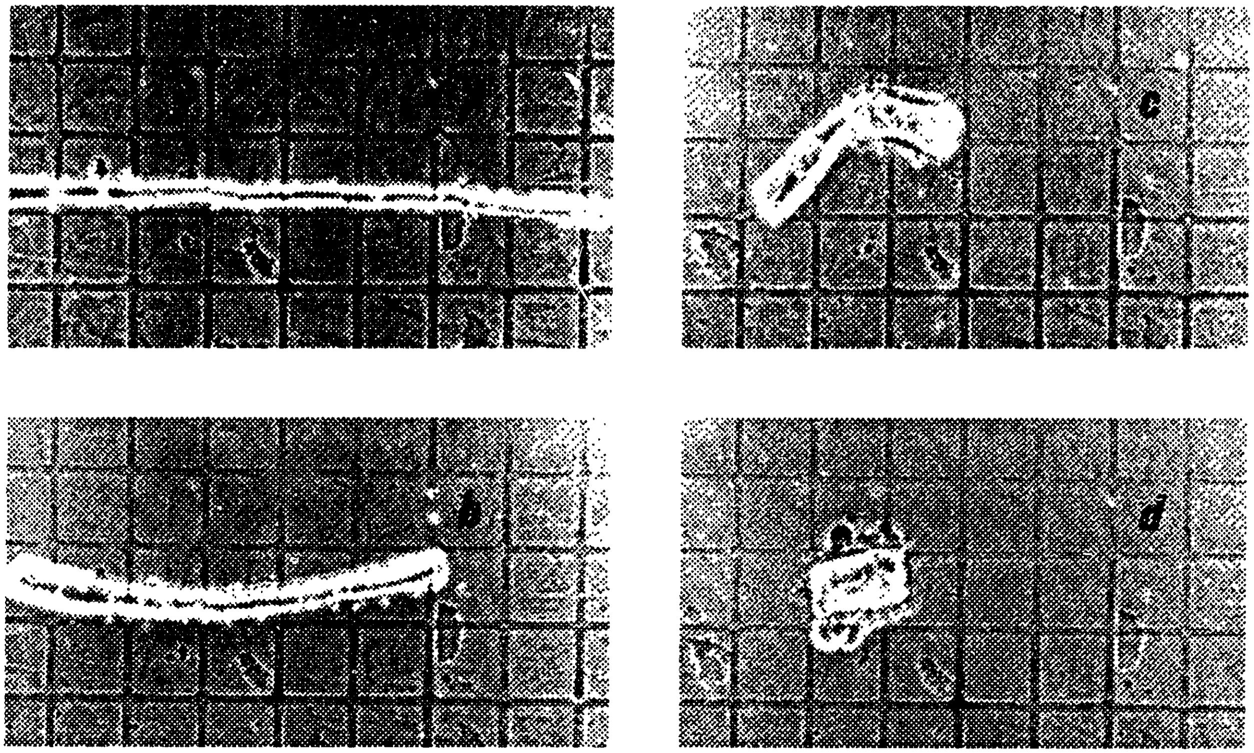

Figure 4.3: Typical cytomorphological response to electric field pulses of 1–4 msec duration and 100–300 V/cm magnitude. In this series of photographs, the cell was exposed to a 1 msec 300 V/cm pulses every 15 seconds. The cell was about 1 mm long (grid is 100 μm) and aligned perpendicular to the applied field (a). After a single pulse, an irreversible contraction occurred (b). Further pulses led to the eventual collapse of the cell along its long axis (c,d).

following membrane disruption.

It appears that the cell membrane remains largely intact, but significantly permeabilized, following the pulse application and cell collapse. In experiments performed with cells loaded with carboxyfluorescein in isotonic solution, no obvious dye leakage was observed, even following the collapse of the cells. However, in most cases, the overall cell fluorescence intensity appeared to the eye to decrease at a rate beyond that due to bleaching, indicating an increase in the membrane permeability to the dye molecules. Quantification of this observation using image processing was not possible due to the movements of the cells.

It is important (and surprising) to note that the volume of the cell in Figure 4.3 following its collapse is roughly the same as it was before the collapse. The length was reduced by a factor of about 6.5, but the radius was increased by a factor of about 2.5. Modelling the cell as a cylinder, the volume is proportional to the length and to the square of the radius. Thus, the volumes are approximately the same. It appears that no cytoplasm is lost in the process.

It was initially considered that the the damage observed might be due to ripping of the cell membrane during the violent twitches which occurred. However, as shown, no evidence of such gross membrane defects was discovered. The twitch and contraction responses must be restrained to a great extent *in vivo* by the support of the extracellular matrix and surrounding cells. In this case, the forces are more likely to result in ripping of the membranes, since there is a mechanical constraint against the force. The extracellular matrix could also be disrupted by the forces. Thus, non–thermal mechanisms of membrane damage other than electrical breakdown are possible.

4.2.2 Membrane Permeability Changes

The experiments performed with cells loaded with carboxyfluorescein in hypertonic solutions were initially designed to provide visual evidence of membrane disruption by making evident sites of dye leakage. However, at no time was such obvious leakage detected, indicating that the effect of the field was to permeabilize but not to grossly rupture the cell membrane.

Membrane permeability changes were observed as an increased rate of dye loss from cells in hypertonic solutions. As will be seen, the induced transmembrane potential required to produce these changes is in the range known to cause membrane electrical breakdown.

Qualitative Studies

Increases in membrane permeability were observed to depend heavily on cell orientation in the electric field. Cells exposed to 20 4 msec 300 V/cm pulses spaced at 15 seconds lost all or nearly all fluorescence intensity in the fifteen minutes following the exposure if aligned perpendicular to the applied electric field, but appeared unchanged if aligned parallel. That no effect was observed for cells aligned parallel to the field is consistent with the results presented in Section 4.1, which showed that exposure to solutions of 3.0–times normal tonicity suppresses the large induced transmembrane potential expected at the ends of a cell. It was proposed that this was due to current blockages by the internal membrane at intervals along the long axis of the cell. The effect observed for cells aligned perpendicular to the field suggests that current is not hindered radially along most of the length of the cell.

Cells aligned diagonally usually lost intensity, but at a markedly slower rate. Cells that were curved lost intensity in the perpendicular parts, but remained bright in the parallel parts. Kinks or sharp bends were not required for this behavior. A gradual curvature could lead to one end of a cell parallel and the other end perpendicular to the applied field. Observed gradients of dye intensity in a cell usually remained for the duration of the experiments (at least one hour). This behavior demonstrated that there was a significant hindrance to dye diffusion along the long axes of the cells. It has been shown by Mastro et al. (1984) that when cells are subjected to hypertonic solutions, translational motion of small molecules (M.W. less than 1000) can decrease significantiy. Mastro et al. hypothesized that the decrease in cell volume under hypertonic conditions is accompanied by an increase in cytoplasmic barriers to diffusion. However, in the skeletal muscle cells, no dye concentration gradients were observed in the radial direction, so it is likely that membrane blockages also played a role in this behavior.

The dramatic difference between the behavior of perpendicular and parallel cells was used to detect induced changes at lower electric field strengths. With the parallel cells essentially acting as controls, relative changes in the intensities of the perpendicular cells could be noted. Without this comparison, it would have been difficult to discriminate between slight induced dye leakage and the natural dye leakage and bleaching that occurred in all cells.

Cells exposed to 250 V/cm pulses and aligned perpendicular to the field exhibited evidence of slow dye leakage. Large fluorescence intensity losses were usually not noticed until one–half hour after exposure. It could take an hour or longer for cells to lose all intensity. When cells were exposed to 200 V/cm pulses, only slight differences between the fluorescence intensities of perpendicular and parallel cells were noted one hour after exposure. Cells exposed to 150 V/cm pulses showed no obvious intensity loss beyond that which occurs in cells of both alignments due to natural leakage and bleaching.

In Section 2.1.2, it was shown that the maximum induced transmembrane potential in a cell aligned perpendicular to an applied electric field E_o is $E_o d$, where d is the cell diameter. The diameters of the cells in hypertonic solution were in the range of 15–20 μm. For this range, the predicted induced potential for an application of 250–300 V/cm is approximately 400–600 millivolts. These potentials are in the range known to cause membrane electrical breakdown for pulse widths on the order of milliseconds and a temperature of about 25°C (see Section 1.3.1). For shorter pulse widths and/or lower temperatures, the critical potential is expected to be higher. However, for the physiologic temperature 37°C, the critical potential is expected to be lower.

As shown in Section 2.1.2, the transmembrane potential induced in cells perpendicular to an applied field does not significantly depend on the conductivity of the cytoplasm, as long as that conductivity is much greater than the conductivity of the membrane. Thus, any changes in the cytoplasm caused by loss of water from cells in hypertonic solutions cannot be expected to alter the induced transmembrane potential. This water loss can, however, reduce the radius of the cell. This reduced radius was used to calculate the induced potential from the applied electric field.

As shown in Section 2.1.2, the transmembrane potential induced in a cylindrical cell perpendicular to an applied electric field has a sinusoidal distribution that is maximum along the sides of the cells facing the electrodes. Thus, the damage will not be uniform over the membrane. Unfortunately, it cannot be expected to be sinusoidally distributed either, since damage occurs above a potential threshold, not in direct proportion to the potential. It is predicted that the membrane will be perforated with damage sites on the areas facing the electrodes where the induced transmembrane potential is above the threshold, and undamaged elsewhere.

Minimal cytomorphological changes were observed. Membrane irregularities were not detected under 10–40× phase–contrast optics. The characteristic striations of the skeletal muscle cells which exhibited dye loss always disappeared. Cells which exhibited little or no dye loss generally retained clear striations. The loss of striations indicates a breakdown of the contractile proteins, presumably due to changes in their chemical environment caused by the membrane disruption. Some swelling of the permeabilized cells was also observed. This may have been due to the regaining of the water lost when the cell was placed in hypertonic solution. When the cell membrane was disrupted, the fluids inside and outside the membrane re–equilibrated.

As explained in Section 3.6.1, the pH was kept under control in all experiments in one of two ways. The first was to supplement the hypertonic solution with 100 mM Hepes buffer; the second was to switch the polarity of the electrodes after every four pulses. With either of these methods, the changes at the electrodes fell to less than 1 pH unit. The membrane permeability changes observed in this experiment did not depend on which method was employed.

It was determined that pH changes and the presence of electrode byproducts in the chamber did not significantly affect the results. It was clear from the results for cells aligned parallel to the field that these artifacts did not affect the permeability of the cells, as they would affect cells independently of their alignment. Also, it was demonstrated that cells could be placed as close to 1 mm from an electrode without a significant change in their response to the field. Occasionally, a cell would end up behind an electrode. These cells always retained fluorescence intensity even though they were exposed to the pH changes and electrode byproducts. They were not, however, exposed to the electric field.

Experiments were usually performed using hypertonic solution prepared with sucrose. To determine whether the sucrose itself had any effect on the membrane permeability changes observed, experiments were also performed using hypertonic solution prepared with mannitol. No qualitative difference in the cellular response to the fields was observed.

The carboxyfluorescein dye molecule carries a negative charge. Migration of the dye in the applied electric field was therefore a concern. It can easily be shown, however, that this had little effect on the results. Assuming a mobility of 1×10^{-5} cm^2/V·sec for the dye molecule in media outside the cell (the value for a small molecule in water), the distance it would move during a 4 msec application of 300 V/cm is .12 μm, two orders of magnitude smaller than the cell radii. Inside the cell, the electric field is much less than the 300 V/cm applied due to the highly insulating cell membrane (before significant permeabilization occurs), and the movement of dye particles would be even less. Particles would diffuse to equilibrium in the cell between pulses, so the movement would not be additive as further pulses were applied. Thus, the migration of dye molecules in the applied electric field could not lead to significant decreases in cell intensity. Proof that this was the case is the fact that dye diffused out of the cell membrane at an increased rate long after the pulse application was completed.

It was considered that the presence of an electric field inside the cell could catalyze chemical reactions altering the fluorescence of the dye. However, before significant permeabilization occurs, the electric field inside the cell is expected to be very small. In addition, the pH dependence of the dye fluorescence was a concern. However, a pH drop of several pH units was found to be necessary to extinguish the fluorescence intensity of the dye. The major evidence indicating that these were not artifacts in the experiment derives from the results of preliminary experiments performed by D. Israel (1988) using the dye Lucifer Yellow. This dye must be injected into the cells, a process that proved to be too time–consuming for use in collecting large amounts of data. However, trial experiments demonstrated qualitatively the same results described here.

As shown in Section 3.6, the chamber temperature never exceeded the physiologic temperature of 37°C. Thus, thermal damage could not have contributed to the permeability changes measured.

It was considered that the direct heating of the membrane by the induced transmembrane potential and current could play a role in membrane electrical breakdown. This, of course, would not be an artifact of this experiment, but the case in all reported observations of the phenomenon. The magnitude of the heating expected to occur can be calculated using Equation 3.1. Due to the extreme thinness of the membrane, the temperature of the membrane will equilibrate with the temperature of the surrounding fluid essentially instanteously, but an upper bound can be approximated. For a cell of radius 10 μm aligned perpendicular to an applied electric field of magnitude

300 V/cm, the induced transmembrane potential is about 600 mV. If the thickness of the membrane is assumed to be 50 Å, the electric field in the membrane is 120 × 10^6 V/m. The membrane conductivity can be approximated by $\sigma = 10^{-4}$ mho/cm^2 × 50 Å. Since the membrane has thermal properties more similar to oil than to water, the density and heat capacity of olive oil can be used: $\rho = .92$ gm/cm^3, $\Theta = .4(4.17)$ J/gm°C (Weast, 1970). Equation 3.1 then predicts a maximum temperature rise of 0.19°C per 4 msec pulse. This is less than the calculated temperature rise in the media (0.7°C per pulse). The interior of the cell is expected to have a negligible electric field and hence negligible heating. It is possible that the small temperature gradients that are briefly induced play a role in cell membrane electrical breakdown.

Quantitative Studies

The induced changes in membrane permeability following electric field exposure were quantified for applied fields of 250, 275, and 300 V/cm. All cells were aligned perpendicular to the field. Using the image processing techniques described in the last chapter, average cell intensity as a function of time was plotted. To facilitate comparison of the responses, each intensity value in a given trial was normalized to the intensity value recorded immediately before pulse application began. To illustrate the response for a given applied field, the normalized plots were averaged. The results are shown in Figures 4.4a through 4.4c. The plots show that in all cases, a clear increase in the rate of fluorescence intensity loss began as soon as the pulse application started. The new rate depended on the applied voltage.

The initial rate of fluorescence intensity loss in cells occurring in the 10 minutes before the pulse application was due to the combined effects of natural dye leakage and bleaching. These effects were removed from the data by subtracting the slope obtained from a linear regression of the first 10 points in Figures 4.4a through 4.4c. The results are shown in Figure 4.5. In this figure, the fluorescence intensity drop is

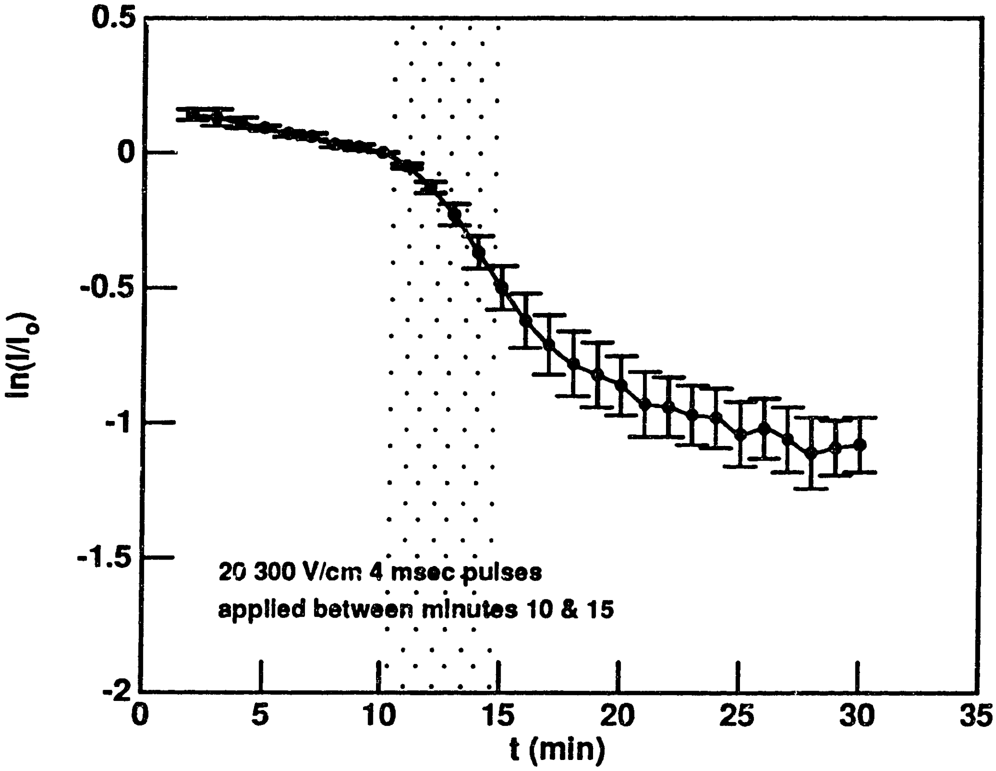

Figure 4.4a: Normalized cell fluorescence intensity versus time for cells exposed to 20 300 V/cm 4 msec pulses between the 10 and 15 minute marks. The average is computed from 7 trials. The error bars represent the standard error of the mean.

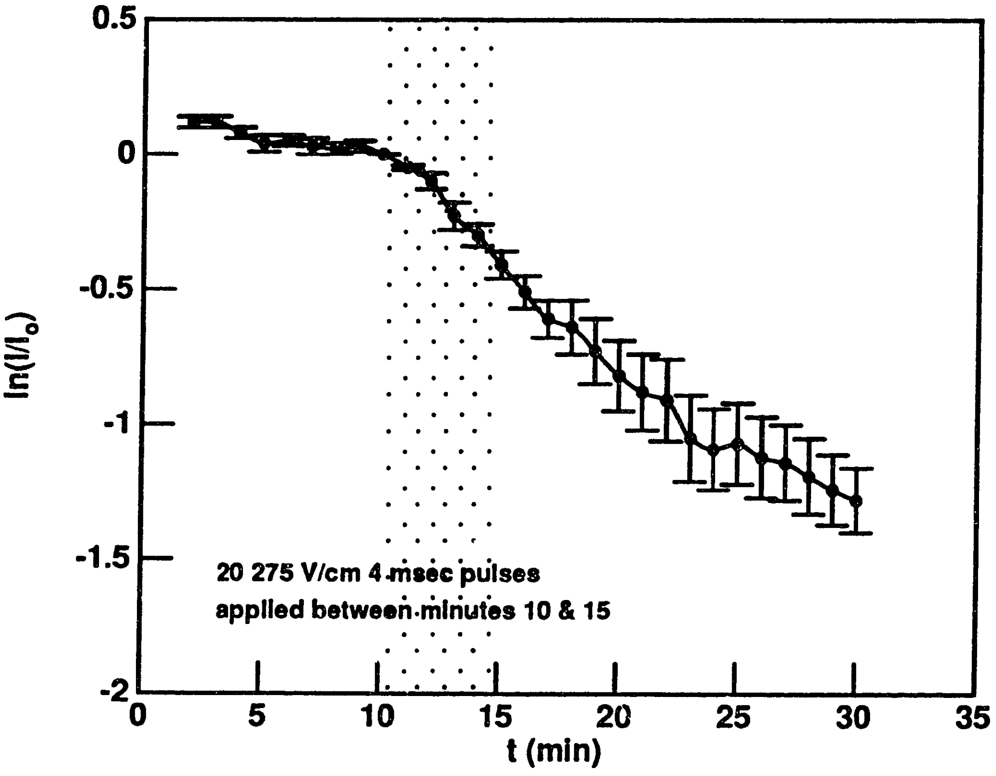

Figure 4.4b: Normalized cell fluorescence intensity versus time for cells exposed to 20 275 V/cm 4 msec pulses between the 10 and 15 minute marks. The average is computed from 5 trials. The error bars represent the standard error of the mean.

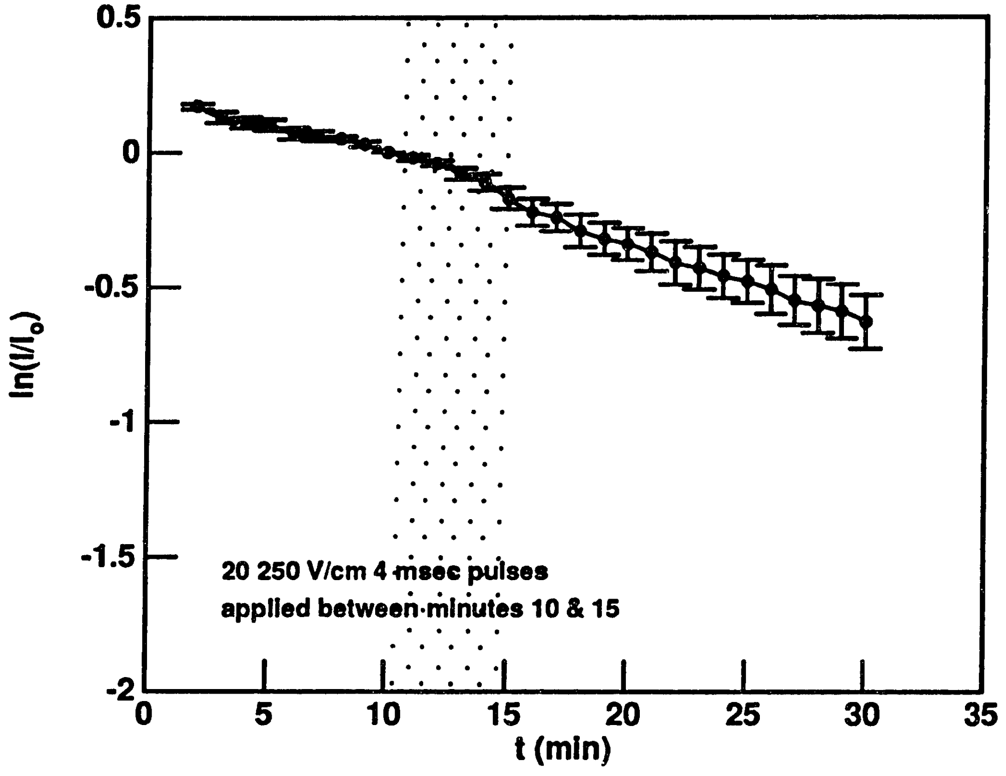

Figure 4.4c: Normalized cell fluorescence intensity versus time for cells exposed to 20 250 V/cm 4 msec pulses between the 10 and 15 minute marks. The average is computed from 7 trials. The error bars represent the standard error of the mean.

due solely to the effects of the electric field pulses.

As illustrated in Figure 4.5, the damage incurred by the cells due to the field exposure appears to be at least partially reversible. For a field application of 300 V/cm, a complete reversal seems occur during a 5 minute period following the exposure. This effect may be partially due to nonlinearities of the imaging system, as the cell intensities were significantly lower 5 minutes after the exposure than they were at the start. It is also likely that the cell exposure to the hypertonic solution caused some dye to become trapped in the internal membrane system due to water removal. In this case, the cell intensity cannot be expected to go to zero, and irreversible damage could lead to the results illustrated in Figure 4.5. However, the fact that the slope began to reverse almost immediately after the exposure was completed is evidence that at least a partial reversal of the permeability increase occurred. The trials using 250 and 275 V/cm show less evidence of reversal. The qualitative experiments performed using 200 V/cm showed that a small but steady dye loss could proceed for as long as an hour after exposure.

As discussed in Section 1.3.1, reversible electric breakdown of artificial planar bilayer lipid membranes has been shown to occur at higher potentials than those causing irreversible breakdown. The proposed reason for this is that when higher voltages are applied, the membrane quickly breaks down and discharges, analogous to the breakdown of a capacitor. This quick phenomenon (thought to last on the order of nanoseconds) appears to cause no lasting damage to the membrane. However, lower induced potentials lead to a slower discharge, and more permanent damage to the membrane.

The diffusion of dye across the cell membrane is described by

$$V \frac{\partial c_i}{\partial t} + J\,A = 0\,; \qquad J = P_m\,(c_i - c_o)\,, \tag{4.1}$$

where V is the volume of cytoplasm, A is the surface area of the cell membrane, c_i and c_o are the dye concentrations inside and outside the cell, J is the flux of dye out of the cell, and P_m is the membrane permeability, which for now is assumed uniform.

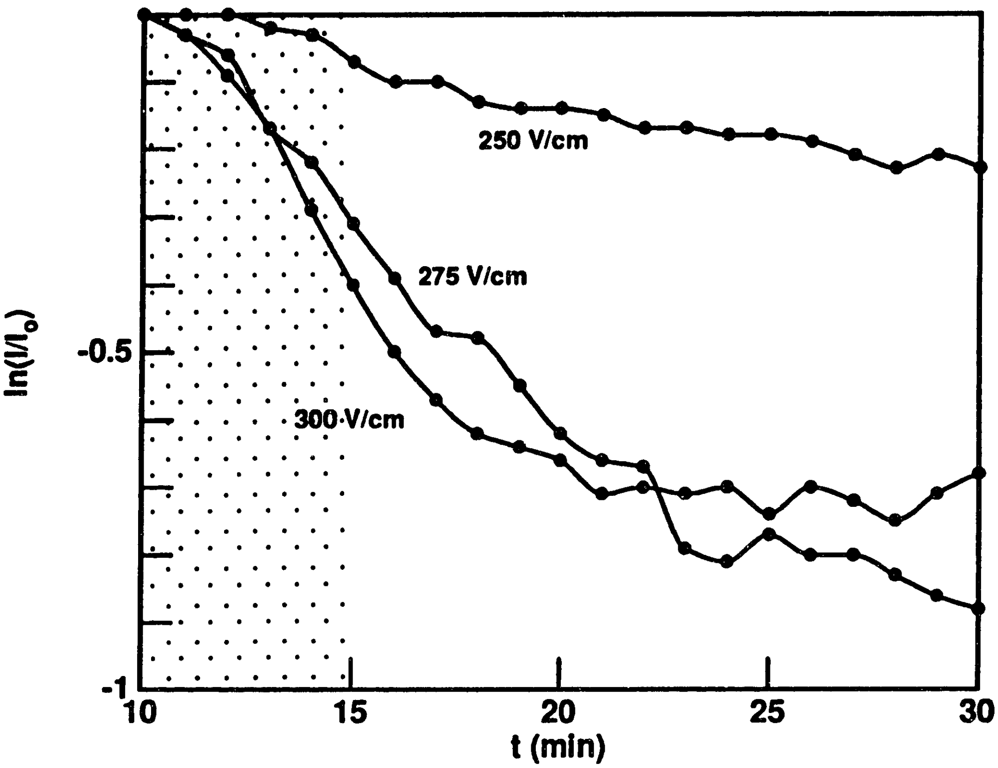

Figure 4.5: Cell fluorescence intensity as a function of time for cells exposed to 20 4 msec electric field pulses of the indicated magnitude between the 10 and 15 minute marks. The effects of natural dye leakage and bleaching have been subtracted off. Thus, the intensity drop is due solely to the effects of the electric field pulses.

Assuming that the dye concentration outside the cell is negligible compared to that inside, the concentration inside as a function of time can be expressed

$$c_i(t) = C\, e^{-t/\tau}\,; \qquad \tau = \frac{V}{AP_m}\,. \tag{4.2}$$

Thus, the dye loss proceeds as an exponential which depends on the permeability. An increase in the permeability leads to a decrease in τ and an increased rate of dye loss. The natural logarithm of c_i is a straight line of slope $s = -\frac{1}{\tau}$. A change of permeability results in a change of slope. Relative changes of permeability can be obtained from the change of slope:

$$\frac{P_{m_2}}{P_{m_1}} = \frac{\tau_1}{\tau_2} = \frac{s_2}{s_1}\,. \tag{4.3}$$

In order to examine the changes in permeability occurring during and after the pulse application, the plots of the natural log of the cell intensity as a function of time were examined for each trial. The initial slope s_1 was determined from the images stored before the application of the pulses. The slope s_2 was taken as the maximum slope calculated using at least four consecutive data points. The ratio of the slopes was calculated for each trial and the values were averaged. The results are plotted in Figure 4.6. The curve has been extrapolated to lower fields using the information obtained from the qualitative experiments. Also plotted are the permeability changes calculated by taking s_2 to be the slope of the data points 10–15 minutes after the pulse application. As shown, smaller permeability changes are calculated for this time period, indicating the reversibility of the process.

The permeability changes indicated in Figure 4.6 are actually lower bounds of the true values. Several effects not included in the analysis act to increase the estimates.

For the calculations of membrane permeability changes, the permeability of the membrane was assumed to be uniform at all times. Clearly, this is not expected to be the case after the cell has been permeabilized by the electric field. Since the experimentally–determined permeability change really represents an average over the

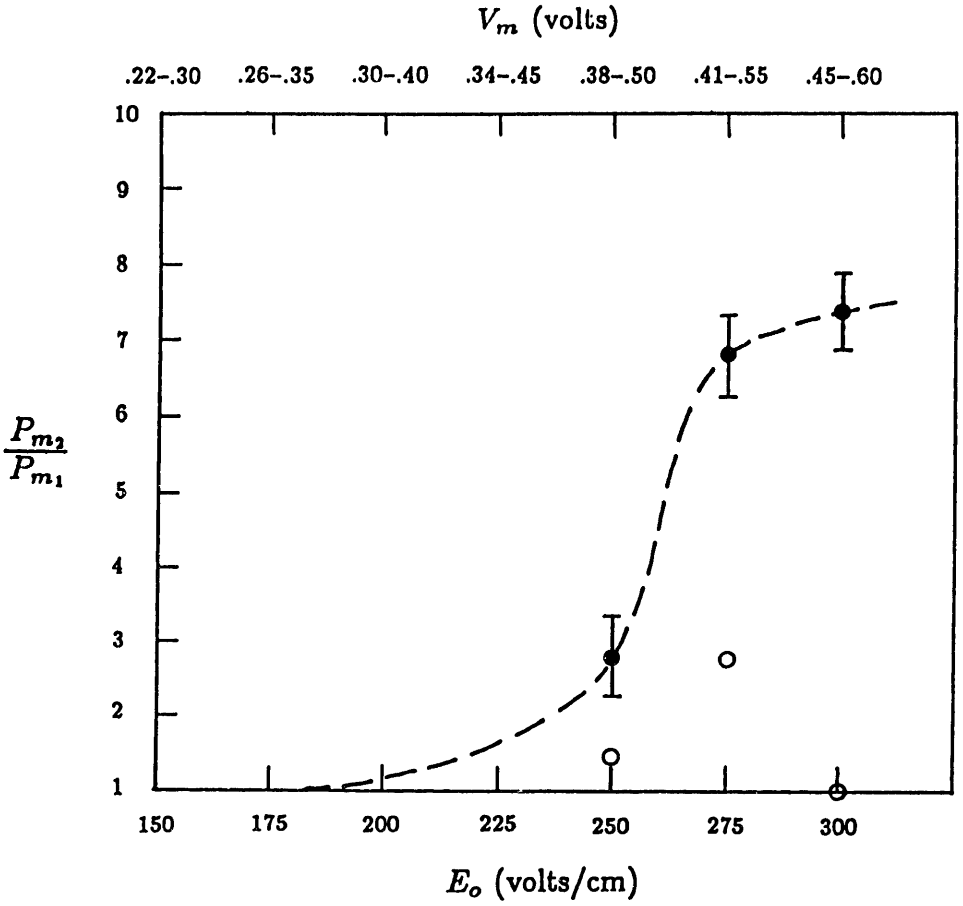

Figure 4.6: Induced membrane permeability change as a function of applied field strength and induced transmembrane potential. The averages are computed from 5–7 trials. The error bars represent the standard error of the mean. The filled circles represent the maximum permeability that occurred during and just after the pulse application. The open circles represent the permeability 10–15 minutes after the pulse application, and give some indication of the reversibility of the process.

extent of the cell membrane, the maximum induced in certain regions must be more than this value. The maximum value can be approximated if it is assumed that the induced increase in permeability has a sinusoidal distribution like the induced transmembrane potential. As already stated, this is not exactly the case, but it will provide a useful approximation. The average of the absolute value of a sinusoid of amplitude P_m is $\frac{2}{\pi}P_m$. Thus, the maximum value of the induced permeability change can be expected to be roughly $\frac{\pi}{2} \approx 1.6$ times the measured value.

Equation 4.1 was used in the analysis with the assumption that all cell fluorescence intensity loss was due to diffusion across the cell membrane. However, in the experiments, this was not the case. The photochemical effect of bleaching also caused a steady decrease in intensity during all intervals when the dye was optically excited. In order to minimize these effects, the cells were only exposed to the excitation for 10 seconds per minute, the minimum required to store images of cells at their full fluorescence intensity. However, it cannot be assumed that the intial slope observed in Figures 4.4a through 4.4c is not at least partially due to bleaching. The effect of this bleaching is to reduce the membrane permeability change calculated using Equation 4.3. In fact, if the bleaching effects were much larger than the diffusive effects, no membrane permeability change would be measured. Therefore, the permeability changes plotted in Figure 4.6 may be underestimated slightly due to the effects of bleaching.

Equation 4.1 is valid only if the dye concentrations are uniform at all times. For rapid dye diffusion from the cell, it might be expected that concentration gradients would form. The time for equilibrium to reestablish in a cylinder following a change is on the order of 0.1 a^2/D (Harris, 1972). The diffusion of small molecules (M.W. less than 1000) in the cytoplasm of mammalian cells has been characterized by Mastro et al. (1984), who demonstrated that the diffusion coefficient in cytoplasm is 1/2 to 1/5th that in water. For a cell radius a of 10 μm and a dye diffusivity D of 20×10^{-7}

cm^2/sec (Mastro et al.'s value for sucrose (with a M.W. close to CDFA) in cytoplasm), this time constant is on the order of 0.05 sec. However, Mastro et al. also showed that the diffusion coefficient can decrease substantially (by factors of 2 or more) when cells are bathed in hypertonic solutions. Nevertheless, the redistribution of the dye takes place in a time under a second, which is negligible compared to the time over which the dye diffuses from the cell (tens of minutes).

Two experiments were performed using 60 300 V/cm *0.4 msec* pulses spaced at 10 seconds. The cells exhibited an increased rate of dye loss as soon as the pulse application started, just as in the trials with the longer pulse width. The maximum permeability attained in both trials was about 2.5 times the starting permeability. The fact that significant damage could be caused with field pulses as brief as 0.4 msec is consistent with the hypothesis that the membrane disruption is caused by the same mechanisms discussed in Section 1.3.1. As discussed in that section, experiments performed by others have shown that irreversible membrane electrical breakdown occurs with pulse widths of 0.1 msec and above.

4.3 Thermal Experiments

4.3.1 Cytomorphological Response

Isolated skeletal muscle cells raised from room temperature to the physiological temperature of 37°C exhibited no cytomorphological changes, as expected. However, temperature elevations just above this value caused cell contraction by an amount that depended on the temperature. Small contractions observed at temperatures between 38°C and 42°C were usually completely reversed when the temperature was lowered to 37°C. Larger contractions occurring between 42°C and 44°C were only partially reversible. Cells raised to temperatures of 45°C and above rapidly and irreversibly collapsed along their main axis. This response appeared to be independent of the rate of heating.

The extent of the contraction at various temperatures is illustrated in Figure 4.7. The sequence of photographs shows five cells at temperatures of 28°C, 38°C, 40°C, 42°C, 44°C and 46°C. Each cell was held at the indicated temperature for one minute before the temperature was stepped up 2°C. The photographs were taken 30 seconds after each new temperature was imposed.

The total collapse of the cells along their major axis that occurred at temperatures of 45°C or above in isotonic solution was irreversible and was very similar to that seen in the electric field experiments. It is likely that the collapse was caused by the denaturation of the actin and myosin filaments since protein denaturation commonly begins at about 45°C (Gershfeld & Murayama, 1988). It is known that the skeletal muscle cells in meat retain their striated appearance while cooking, even for long periods at high temperatures; however, significant protein alterations occur (Davey & Winger, 1979). The first phase of cooking, at temperatures of 40–50°C, is associated with a loss of myosin solubility and denaturation of the contractile system. Sarcoplasmic proteins are also denatured in this temperature range.

The stimulus of the partially-reversible contractions observed at lower temperature elevations is unknown, but it is possible that a temperature-induced increase in the permeability of the cell membrane or the sarcoplasmic reticulum to calcium ions is the mechanism. It is unlikely that any significant membrane defects were formed at such small temperature elevations, but membrane transformations resulting in leaky patches have been postulated by others (Gershfeld and Murayama, 1988) to occur at even 1°C above physiologic temperature. It is also possible that the actin–myosin complex itself is temperature sensitive in this low temperature range. The fact that these contractions were at least partially reversible indicates that the contractile mechanism was at least partially functional following the exposure to the elevated temperature.

In several experiments, cells were loaded with carboxyfluorescein in isotonic solution. No obvious dye leakage was observed when the cells were collapsed by exposure

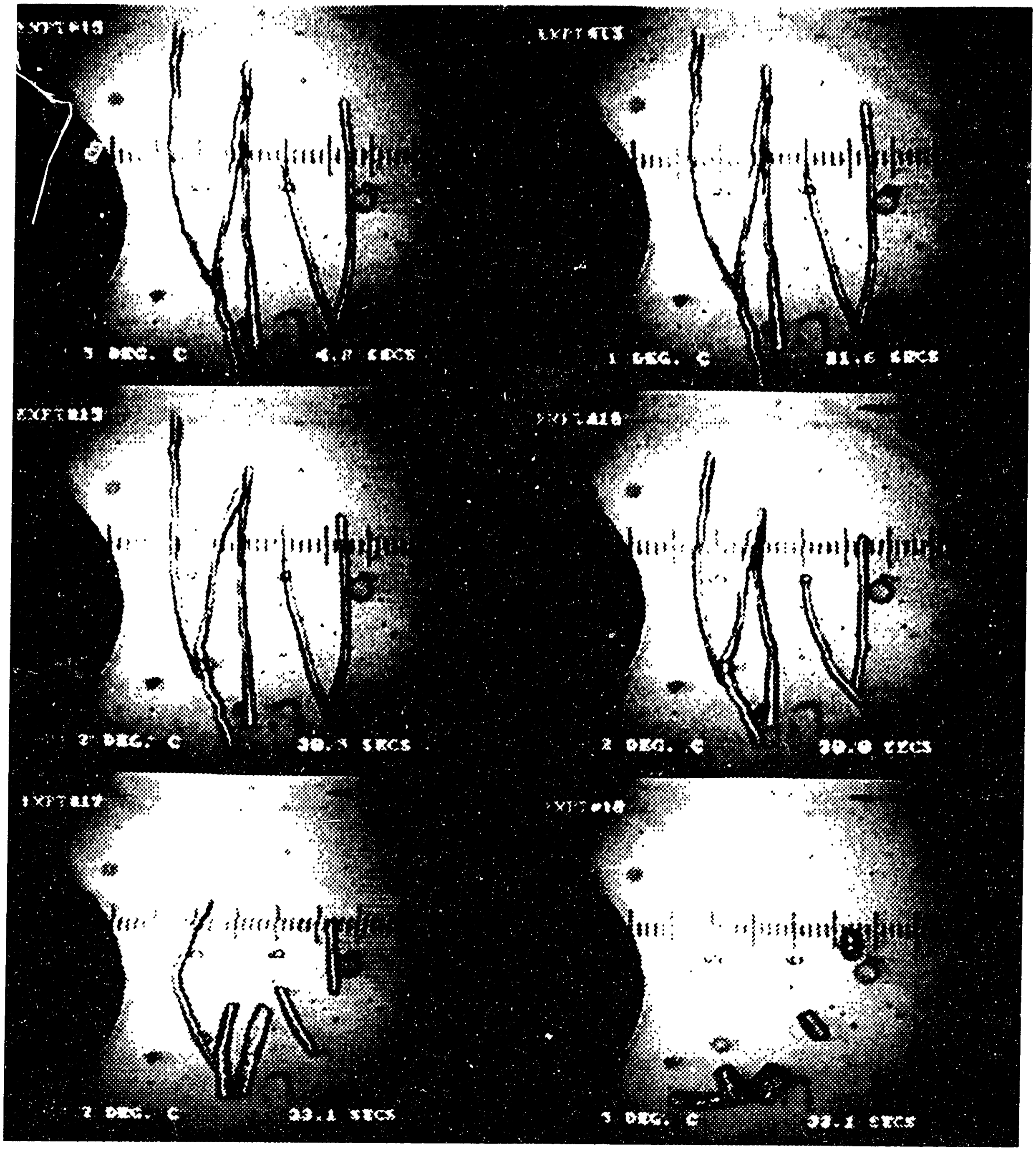

Figure 4.7: Cytomorphological response to supraphysiological temperatures. The temperature in the chamber was raised in 2°C increments from room temperature to 46°C. Each temperature was held for 1 minute. The photographs show the cells 30 seconds after temperatures of 38°C, 40°C, 42°C, 44°C and 46°C were imposed. The dark semicircle on the left of each image is the thermocouple.

to temperatures just above 45°C. This indicates that the cell membranes were not significantly disrupted when the cell collapsed. As in the collapse associated with applied electric field pulses (see Section 4.2.1), the collapse was not accompanied by any significant change in cell volume. When cells were rapidly raised to temperatures of 60°C or higher, evidence of dye would appear outside the collapsed cell for several seconds until it diffused away. This indicates an increased permeability of the cell membrane caused by the heating.

The collapse of the cells in response to both thermal and electrical stimuli prompted the concern that the electrical response could be due to heating, even though the temperature rise associated with each field pulse was very small. To examine this, cells initially at room temperature were exposed to heat 'pulses' by raising the temperature rapidly (over 1000°C/min) and then immediately forcing them to cool back down to room temperature over a 15-second period. Repeated heat pulses to temperatures below 37°C showed no cellular response. Heat pulses to temperatures between 37°C and 40°C caused very slight reversible contractions to occur, as expected. At no time did collapse occur. Unfortunately, the rate of heating used (the maximum attainable with the system) was substantially less than that caused by a 4 msec electric field pulse, but the imposed temperatures were much greater. However, no evidence to suggest a thermal contribution to the cytomorphological changes observed in the electrical experiments was discovered.

4.3.2 Membrane Permeability Changes

Increased membrane permeability at elevated temperatures was demonstrated using skeletal muscle cells loaded with carboxyfluorescein in hypertonic solutions. The increased permeability was observed as an increased rate of dye loss from the cell. The increase in permeability generally did not appear immediately after an elevation from room temperature to temperatures between 45 and 60°C. Rather, a delay occurred before the onset of dye loss. The length of the delay depended on the magnitude of the temperature rise. The rate of dye loss following the delay also depended on the temperature.

At high temperatures (above about 60°C), the presence of dye outside the cell immediately following the temperature rise was apparent with the proper brightness and contrast settings on the monitor, as illustrated in Figure 4.8. The dye diffused rapidly away from the cell, and was replaced at a slower and slower rate as the dye concentration inside the cell decreased. At lower temperatures, or with lower contrast settings on the monitor, dye outside the cell was not readily detected. This was required in the experiments so that the image processing software could properly identify the cell at all times.

The kinetics of the dye loss were quantified for cells raised to temperatures of 45°C, 50°C, 55°C, and 60°C. The average fluorescence intensity of the dye in the cells as a function of time was plotted for each trial. To facilitate comparison of the responses, the fluorescence intensities at each time point in a given trial were normalized to the value recorded just before the elevation of the temperature. To illustrate the kinetics of the response, the normalized plots for a given elevated temperature were averaged. The results are shown in Figures 4.9a through 4.9d. The delay before the onset of dye loss is evident in the plot for 45°C. The large scatter after the delay indicates the variability of the response. Many individual trials exhibited longer delays than apparent in the average. The plot for 50°C shows a smaller delay and a similar variability in the response. The plots for 55°C and 60°C illustrate the rapid onset of dye loss that occurred at the higher temperatures.

In Figure 4.9a the plot levels off at the point were the temperature was elevated. This is because some (but not all) of the individual plots showed a small but clear increase (a few percent) in intensity at this point. Since it was shown (see Section 3.7.4) that the fluorescence intensity of the dye was not temperature dependent, another

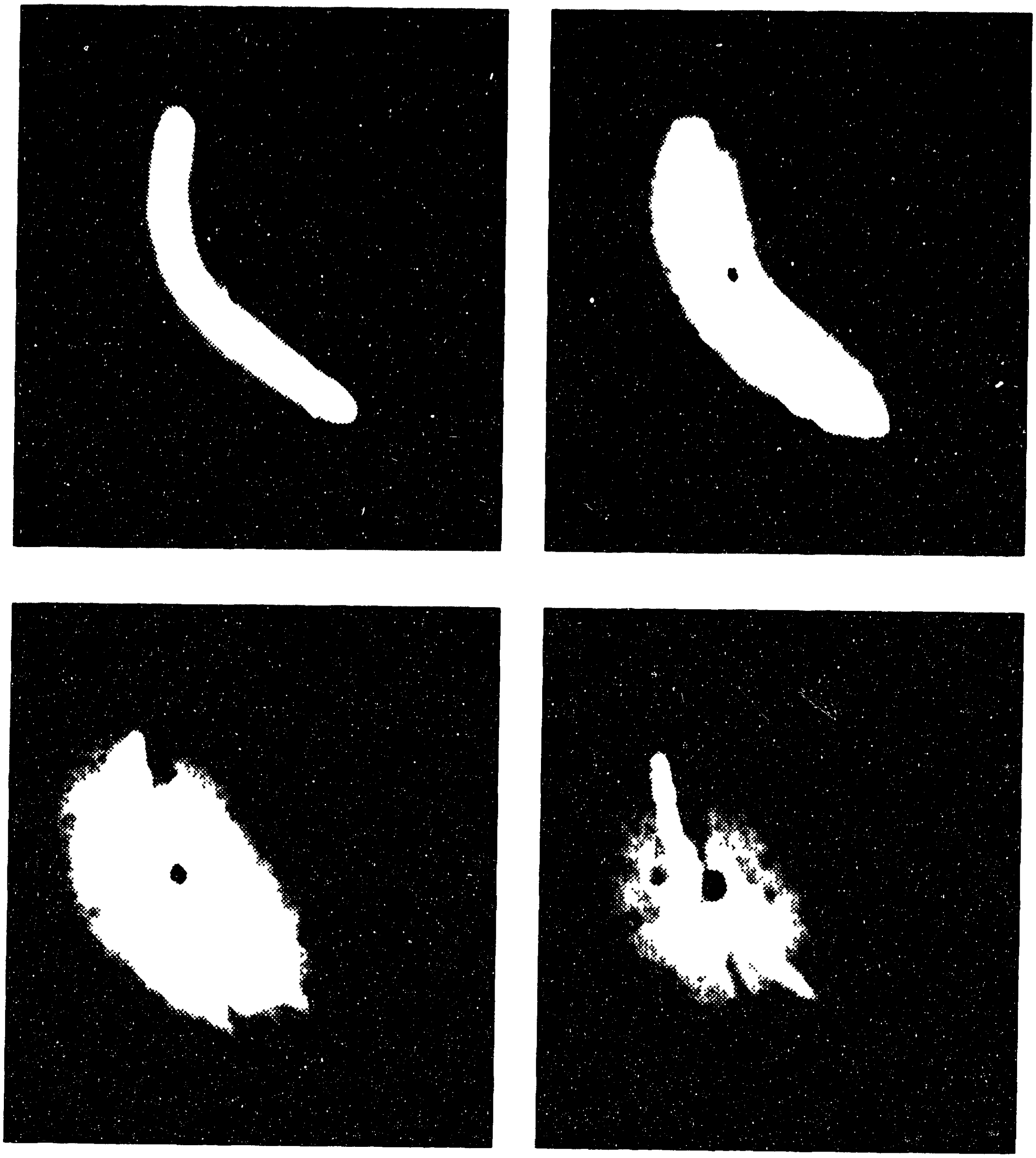

Figure 4.8: Diffusion of carboxyfluorscein across a cell membrane of thermally induced increased permeability. The cell was raised to 60 C in 5 seconds. The high contrast sequence of photographs shows the dye leakage before the temperature rise and every 10 seconds for the 30 seconds following the temperature rise. The cell lost all fluorescence intensity within 60 seconds

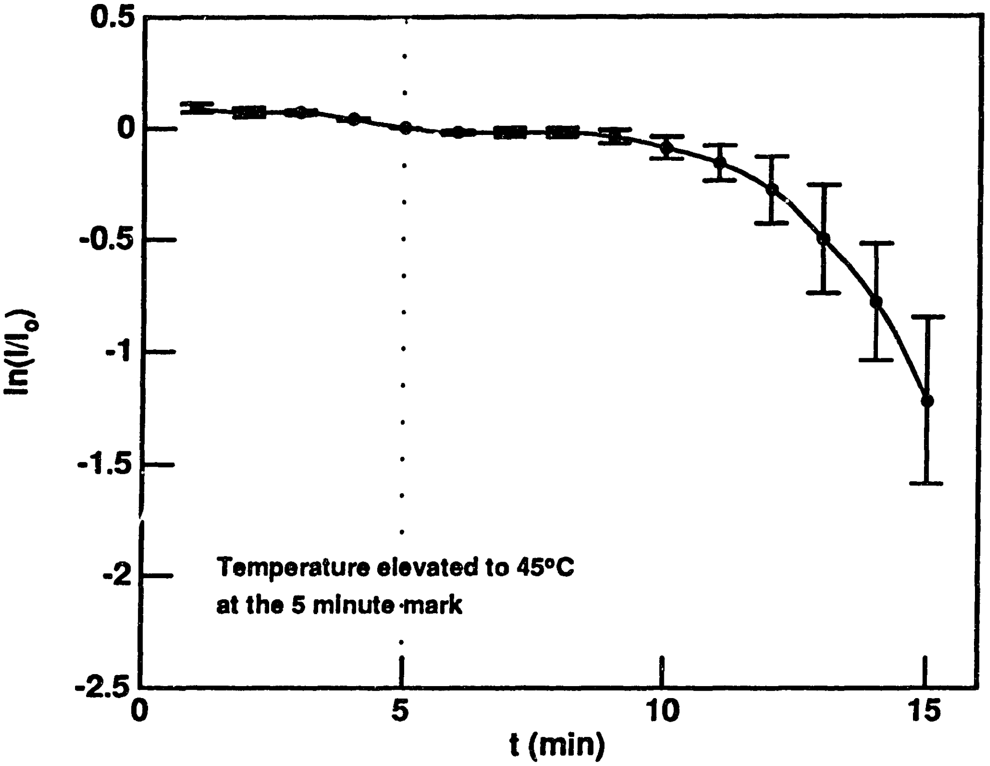

Figure 4.9a: Normalized cell fluorescence intensity as a function of time for cells elevated from room temperature to 45°C in 5 seconds at the 5 minute mark. The averages are computed from 9 trials. The error bars represent the standard error of the mean.

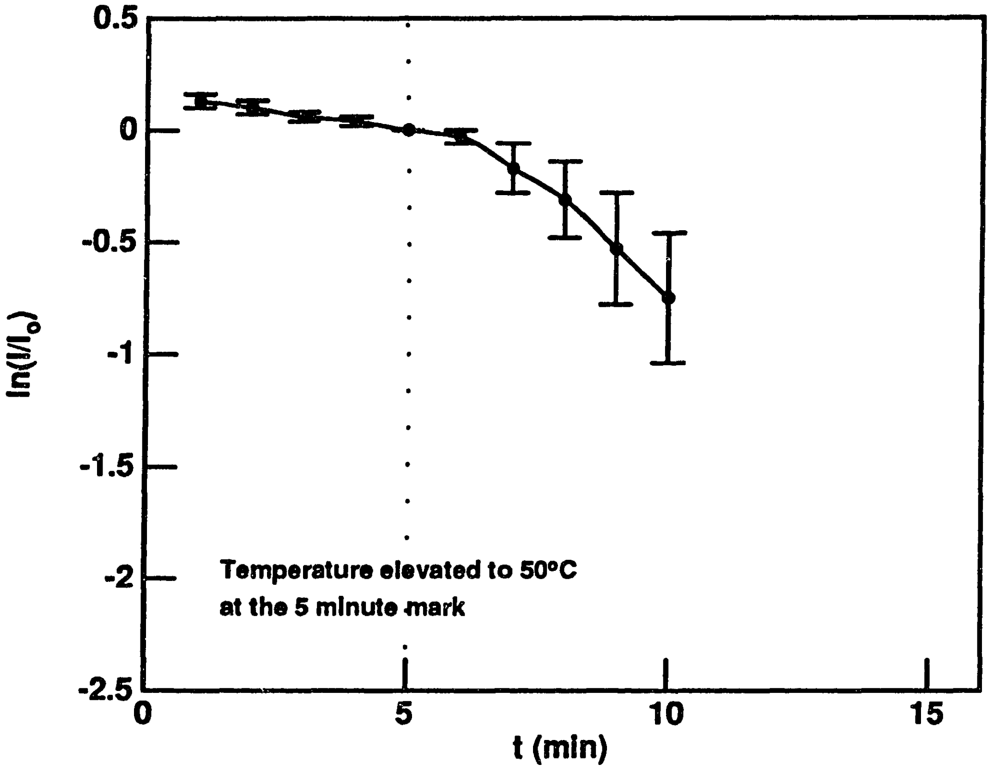

Figure 4.9b: Normalized cell fluorescence intensity as a function of time for cells elevated from room temperature to 50°C in 5 seconds at the 5 minute mark. The averages are computed from 11 trials. The error bars represent the standard error of the mean.

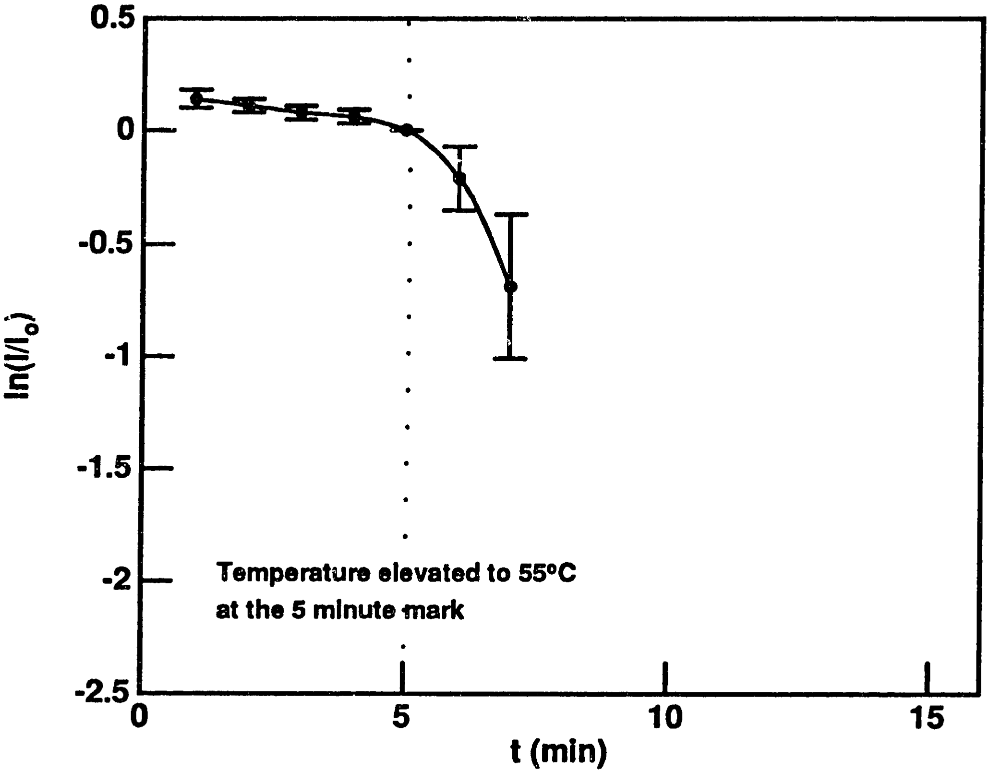

Figure 4.9c: Normalized cell fluorescence intensity as a function of time for cells elevated from room temperature to 55°C in 5 seconds at the 5 minute mark. The averages are computed from 5 trials. The error bars represent the standard error of the mean.

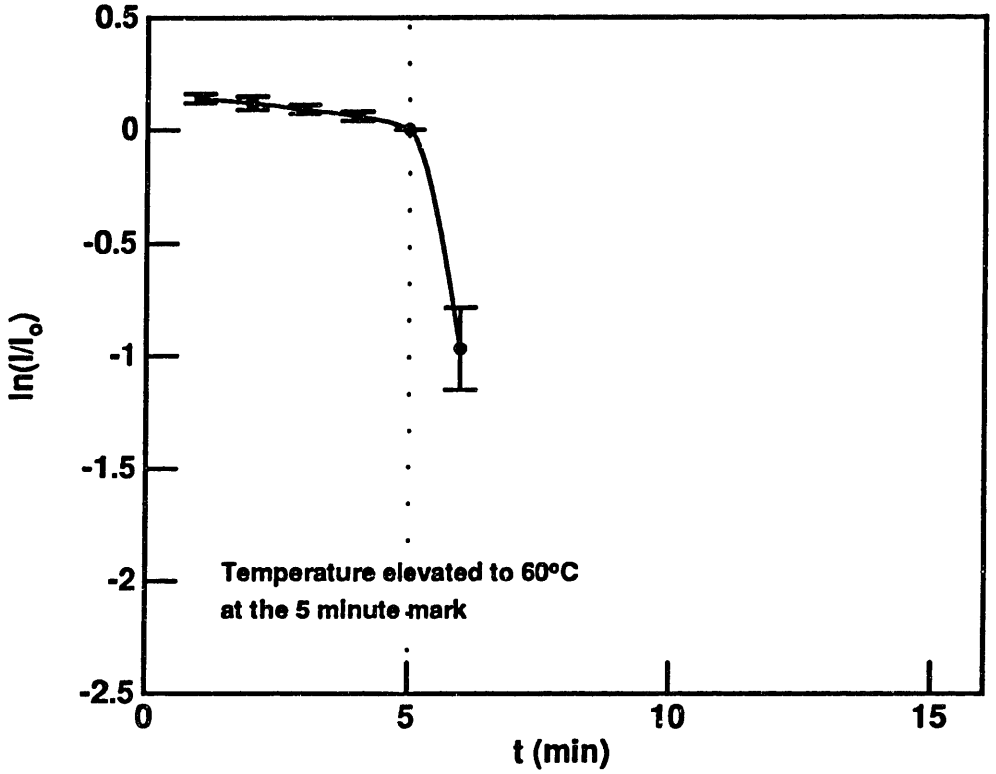

Figure 4.9d: Normalized cell fluorescence intensity as a function of time for cells elevated from room temperature to 60°C in 5 seconds at the 5 minute mark. The averages are computed from 6 trials. The error bars represent the standard error of the mean.

mechanism must have caused this effect. It is possible that the increased temperature led to an increased rate of dye cleavage in the cell, so that if there were any non-cleaved dye molecules in the cell at the start of the experiment, they were quickly cleaved when the temperature was elevated, leading to a small jump in the baseline intensity level.

It was demonstrated that the fluorescence intensity of the dye in healthy cells under observation at 37°C did not generally begin to decrease significantly for at least one-half hour. Since cells at the temperatures of interest began to lose intensity within 10 minutes, it is clear that the responses were not interrupted by the effects of bleaching or harmful effects of the optically-excited dye molecules.

The initial rate of fluorescence intensity loss in cells occurring in the 5 minutes before the temperature elevation was due to the combined effects of natural dye leakage and bleaching. These effects were removed from the data by subtracting the slope obtained from a linear regression of the first 5 points in Figures 4.9a through 4.9d. The results are shown in Figure 4.10.

Since the characteristic response was a clear delay before the onset of dye loss, the time t_d until 5% dye loss was chosen as the criterion of damage. The delay times were obtained from Figure 4.10. Also examined were the times until 10% , 20% and 40% loss. The results are illustrated in Figure 4.11.

In order to model the processes involved in the delay as an Arrhenius process (see Section 1.3.2), the natural logarithm of t_d was plotted against the inverse of T (in degrees Kelvin), as illustrated in Figure 4.12. The points were fitted to a straight line. The slope and intercept of this line provided the relation:

$$\frac{1}{t_d} = 1.6 \times 10^{37} \, e^{-\frac{29{,}000}{T}} \, (\frac{1}{\text{sec}}) \, . \tag{4.4}$$

This can be compared to the Arrhenius relation:

$$\frac{d\Omega}{dt} = F \, e^{-\frac{E}{RT}} \, . \tag{4.5}$$

The activation energy (E) for the process is 58 kcal/mole.

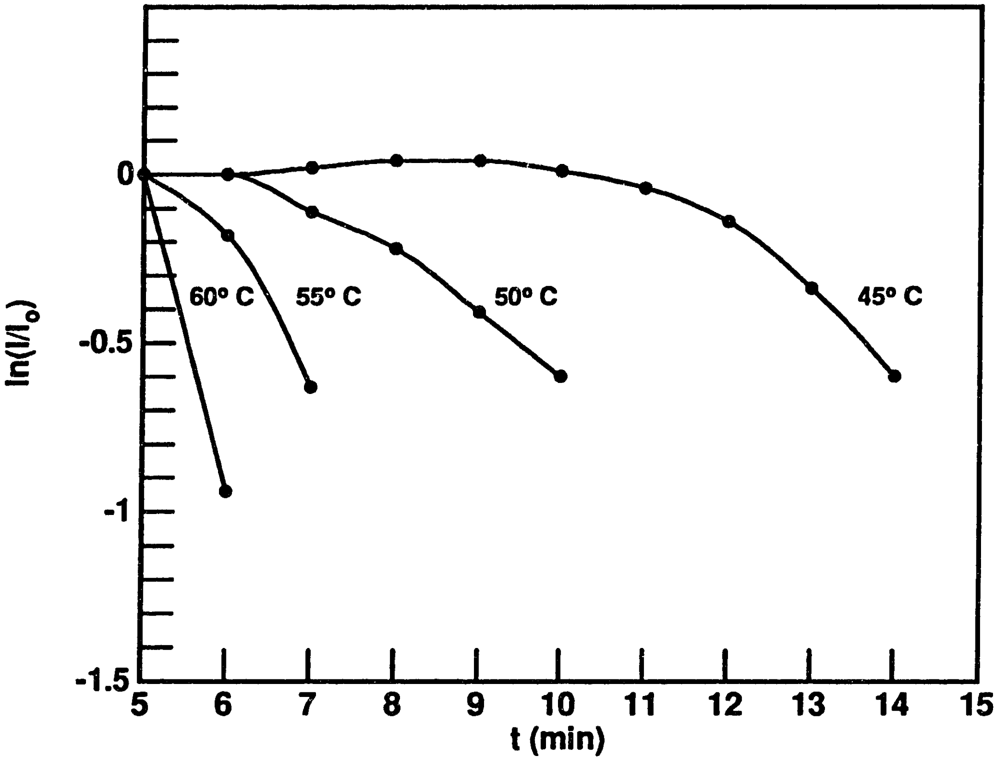

Figure 4.10: Cell fluorescence intensity as a function of time for cells elevated from room temperature to 45, 50, 55, and 60°C in 5 seconds at the 5 minute mark. The effects of natural dye leakage and bleaching have been subtracted off. Thus, a slope of zero indicates the normal membrane permeability.

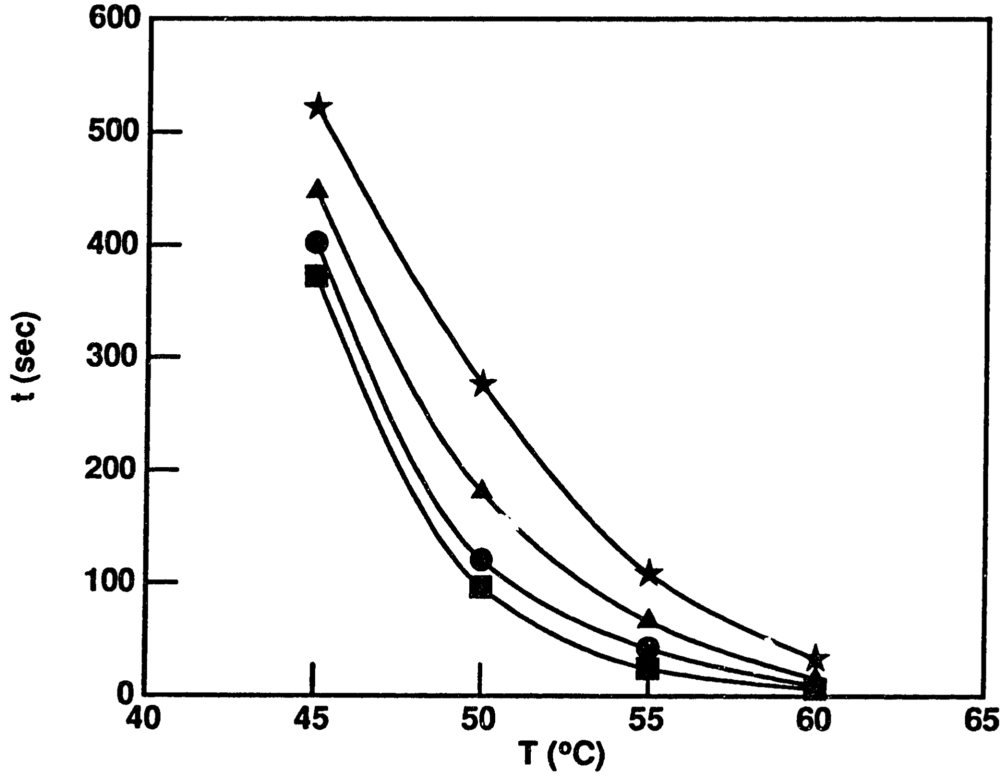

Figure 4.11: Time *t* to 5% (squares), 10% (circles), 20% (triangles), and 40% (stars) cell fluorescence intensity loss as a function of the temperature *T*. The data points were obtained from Figure 4.10.

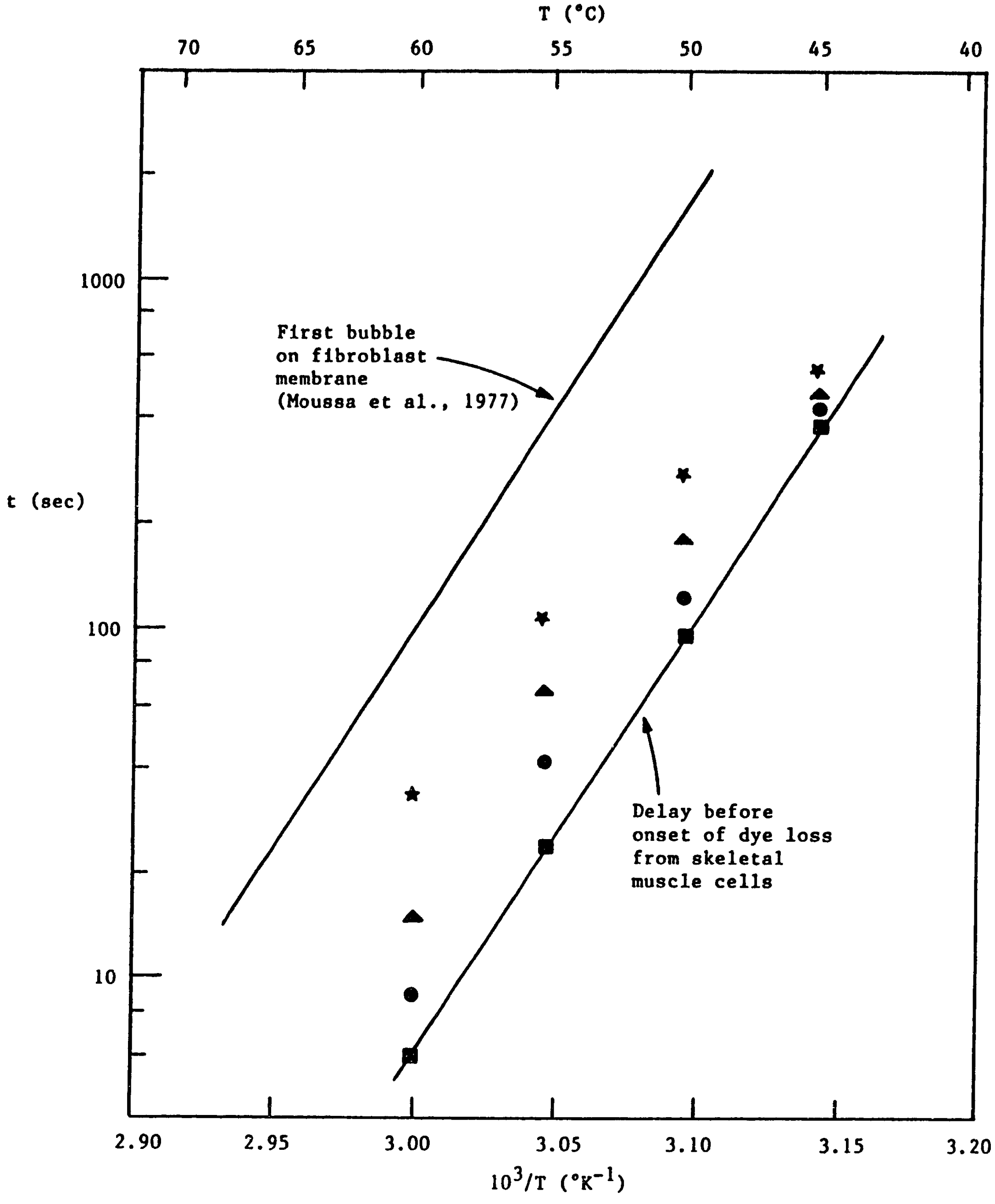

Figure 4.12: Arrhenius plot showing the natural log of the delay before cell fluorescence intensity loss (5%) versus temperature. The slope of the line fitted to the data provides an activation energy for the process of 58 kcal/mole. The data for 10%, 20%, and 40% dye loss are also indicated (as circles, triangles, and stars respectively). The results of Moussa et al. (1977) are shown for comparison.

The fluorescence experiments in hypertonic solutions provided quantification of membrane permeability changes, one manifestation of the membrane alterations induced by heating. The results of similar experiments by Moussa et al. (1977) are also plotted in Figure 4.12. Moussa et al. used the time required at the given temperature until membrane blebs (blisters) were apparent as the criterion of damage. As shown, the formation of these gross membrane defects takes longer than membrane alterations resulting in a permeability increase. The activation energy derived from Moussa et al.'s data is 59.5 kcal/mole, nearly the same value obtained here. Thus, it appears that the process of membrane damage that occurs due to elevated temperatures in the range of 45–60°C has an activation of about 58–59 kcal/mole. The process can first be observed as a membrane permeability increase, and later as the formation of membrane blebs.

As mentioned previously, the rate of dye loss following the delay depended on temperature, as illustrated in Figure 4.10. To analyze this effect, the times until 10%, 20%, and 40% loss of intensities occurred were examined. The time between t_d (5% loss) and 40% loss is over 4 times greater at 45°C than at 60°C. It could be hypothesized that this was purely due to the temperature dependence of the diffusion coefficent for the dye in the system. That is, once the membrane was damaged in the time t_d, the dye leakage proceeded as simple diffusion across the permeabilized membrane and into the surrounding medium. For water molecules, the diffusion coefficient D is proportional to the ratio of the temperature T (in °K) to the viscosity η (Powell et al., 1941). The viscosity of pure water has been shown to have a temperature dependence $\eta = A(T/T_o - 1)^{\mu}$, where $A = 0.139$ cP, $T_o = 225$°K, and $\mu = -1.64$ (Taborek et al., 1986). Thus, is can be calculated that the diffusion coefficient will rise by a factor of only 1.3 when the temperature is raised from 45°C to 60°C. The temperature dependence of the diffusion coefficient for the dye in the system cannot be expected differ significantly from that for water. Therefore the temperature dependence of the diffusion coefficient cannot account for the temperature dependence of the dye leakage following the delay. It appears that the extent of the damage caused in the time t_d is temperature dependent, and/or that the damage continues to accumulate after the delay at a rate that depends on temperature.

Further study is required to characterize the membrane alterations that occur due to elevated temperatures. As already mentioned, structural defects in the bilayer lipid portions of the membrane are expected (Gershfeld & Murayama, 1988). In addition, denaturation of the membrane proteins is expected at temperatures above 45°C. The extent of the contributions of these two mechanisms will be temperature dependent. It is likely that the behavior below 45°C will differ dramatically from that above 45°C.

Chapter 5

Conclusions

This final chapter will examine the relevance of the experimental results to electrical injury. The goal is to determine when each of the two mechanisms of cellular damage explored in this thesis contributes to the damage in the various muscles in typical cases of electrical injury. Guidelines will be established to aid surgeons in locating damage and determining its direct cause. The electric field and temperature exposures in electrical trauma discussed in Section 1.4 will be used in combination with the results presented in Chapter 4 to meet these goals.

In this thesis, electrical breakdown of rat skeletal muscle cell membranes was demonstrated. Increased membrane permeability was observed with the aid of a fluorescent dye when membrane potentials on the order of 400–600 mV were induced. As discussed in Section 1.3.1, this range of induced potentials has been shown to cause membrane electrical breakdown in other membrane systems. At the low end of this range, the permeability increased by factors of at least 2–4, with only a slight reversal over times as long as one hour. At the high end of this range, a greater permeability increase (by factors of at least 7–11) was observed, but at least partial recovery of the membrane integrity appeared to take place. Cells which exhibited an increased permeability state also lost their characteristic striation pattern, indicating a breakdown of the contractile mechanism and loss of function. Thus, even if the membrane defects induced were reversible and membrane integrity was reestablished, damage was caused that was probably irreversible.

The experiments demonstrating electrical breakdown were performed using cells aligned perpendicular to the applied field. Yet in typical cases of electrical injury, the electrical field is predominantly parallel to the skeletal muscle cells in most tissue groups. Unfortunately, experimental conditions prohibited observation of increased permeability states induced in cells aligned parallel to the field. The hypertonic solution used to paralyze the skeletal muscle cells caused the removal of some water from the cells. The water loss appeared to alter the internal structure of the cells, blocking the current flow along the long axes of the cells. This was demonstrated using the potentiometric dye di–4–ANEPPS. Cells in isotonic solution exhibited induced transmembrane potentials roughly as predicted by the cable model analysis of Section 2.1.1. However, this response was nearly entirely suppressed for cells in hypertonic solutions of 3.0–times normal tonicity. The changes in the internal structure of the cells that led to these problems probably have to do with the membranes of the T–tubules and the sarcoplasmic reticulum which exist at each sarcomere. The loss of water may cause some overlap or bunching of the membranes leading to the blockages. One need not assume that this occurs at every sarcomere to explain the observations, but it must occur frequently along the cell. This effect led to further complications by causing diffusion to become inhibited along the long axes of the cells. There was no evidence that diffusion was significantly limited radially. Thus, the dye was compartmentalized, and membrane damage occurring only at the ends could not lead to a significant decrease in cell fluorescence intensity.

It will be assumed that the threshold determined using cells perpendicular to the applied field holds generally. That is, electrical breakdown occurs for the skeletal muscle cell membrane whenever and wherever potentials on the order of 1/2 volt are induced.

In order to determine the applied electric field strength that puts a muscle tissue at risk of membrane electrical breakdown, the induced transmembrane potential as a function of field strength must be known. The cable model analysis of Section 2.1.1 provides this relationship for cells aligned parallel to the applied electric field. The induced potential is largely dependent on the cell length and radius. For the isolated skeletal muscle cells used in the experiments, an applied field of only 10–25 volts/cm can lead to an induced transmembrane potential of 1/2 volt in the ends of cells aligned parallel to the electric field. As illustrated in Figure 2.6, cells in intact muscle experience larger induced transmembrane potentials than isolated cells for a given applied field, so the required applied field for membrane electrical breakdown may be significantly less than this amount. For larger human skeletal muscle cells, which can reach lengths of 10 cm (Mannherz & Holmes, 1982), the value should be lower still. Nevertheless, for the purposes of the following discussion, the critical electric field will be assumed to be 25 volts/cm. As will be seen, the value is low compared to the fields generally required to produce significant heating with contact durations of interest, so a more precise value is not required for the comparison of the two mechanisms.

The determination of a critical temperature required for damage is complicated by the fact that it is the time the cell is held at a specific elevated temperature that determines the extent of damage. In the experiments performed for this thesis, the contractile mechanisms of the cells were destroyed immediately following exposure to temperatures of 45°C and above. However, an increased membrane permeability state at this temperature did not begin to appear for several minutes after the temperature elevation. At higher temperatures, the increased permeability state commenced more rapidly. Thus, if contractile mechanism damage is of interest, the critical temperature appears to be 45°C, but when the issue is membrane integrity, the temperature history of the tissue is important. A tissue which experiences 55°C for a minute or less would exhibit no membrane permeability change, while a tissue exposed to 45° for several minutes would.

As indicated in Figure 1.14, the most common nonfatal high–voltage electrical injury experienced by electrical utility workers results from contact with a 6000–10,000 volt electric powerline. The current entry and exit sites on the body determine the strength of the electric field experienced by the tissues. A hand–to–hand contact between line voltage and ground would lead to an average field in the arms of about 60–100 V/cm, assuming an arm length of 0.5 m. Hand–to–foot contact would lead to a similar average field in the arm, but a lower average field in the leg due to its larger cross-sectional area. Contacts separated by shorter distances can lead to much higher electrical field strengths in the tissue. The resistance of a human limb is approximately 250–500 Ω. Thus, the current expected for hand–to–hand or hand–to–foot contact of 6000–10,000 volts is 6 to 20 amps.

It is interesting to compare these "high–voltage" exposures to the "low–voltage exposure" of a child sucking on a household extension cord. In the latter case, 120 volts is dropped across about 1 cm, setting up an electric field larger than that occurring in many cases of high–voltage electrical injury. Since it is the field strength that determines the extent of heating and membrane electrical breakdown, it is clear that the classification of injuries into high–voltage and low–voltage has little relevance clinically.

The duration of voltage contact in most cases of electrical injury is not known. High–voltage injuries often occur without physical contact with the voltage line since arcing through the air can establish the current flow. In these cases, the victim is quickly thrown away from the line and the contact may last only a fraction of a second. In the other extreme, victims grasping a dead line will usually find themselves unable to let go when the line is energized due to muscular contractions. In this case, the contact may last for a few seconds or longer. Long contacts also can occur when victims fall on a line or a line falls on them and the victim can not easily escape.

The heating expected to occur in muscle tissue experiencing a given field strength

E for a given period of time t can be easily computed using Equation 3.1. Muscle tissue has a conductivity σ of approximately 4×10^{-3} mhos/cm and a specific heat $\rho\theta$ of approximately 4.14 J/gm/°C (Tropea, 1987). Thus, the temperature rise in degrees C is about $E^2t/1000$. This equation is plotted for temperature rises from 37°C to 45°C, 50°C, 55°C, and 60°C in Figure 5.1.

Membrane electrical breakdown is expected to occur significantly above fields of about 25 V/cm for any realistic duration of contact. However, the duration of contact will affect the extent of the damage. For a 60 Hz signal, 120 electric field "pulses" per second will be applied. As shown in Figure 5.1, there is a large range of exposures having short duration and/or low intensity that can lead to membrane electrical breakdown but not to thermally-mediated damage.

With the aid of the computer simulations of electrical trauma developed by Tropea (1987,1989), the results of Chapter 4 can be related to the electrical and thermal exposures in typical cases of electrical injury. Figure 5.2 illustrates the thermal response of muscle tissues in the arm following exposure to 10 amps for 1 second. The time-temperature thresholds for the onset of increased membrane permeability has been taken from Figure 4.12 and added to this figure. The Arrhenius fit of the data has been used to extend the curve down to 40°C. However, the true threshold curve must deviate from the Arrhenius fit as temperatures approach 37°C or else a non-zero rate of damage will be predicted at the physiologic temperature. Thus, it is expected that the extension of the curve provides a lower bound on the time until damage, and does not represent the actual behavior. As shown, it appears that only the distal-forearm reaches a temperature high enough to lead to membrane permeabilization by a thermal mechanism. The mid-forearm and the proximal-elbow may intersect the threshold curve at long times, but as just noted, the curve underestimates the true threshold. In any case, permeability changes induced at temperatures of 40°C and below cannot be expected to be significant, as these temperatures are in the fever range. The mid-

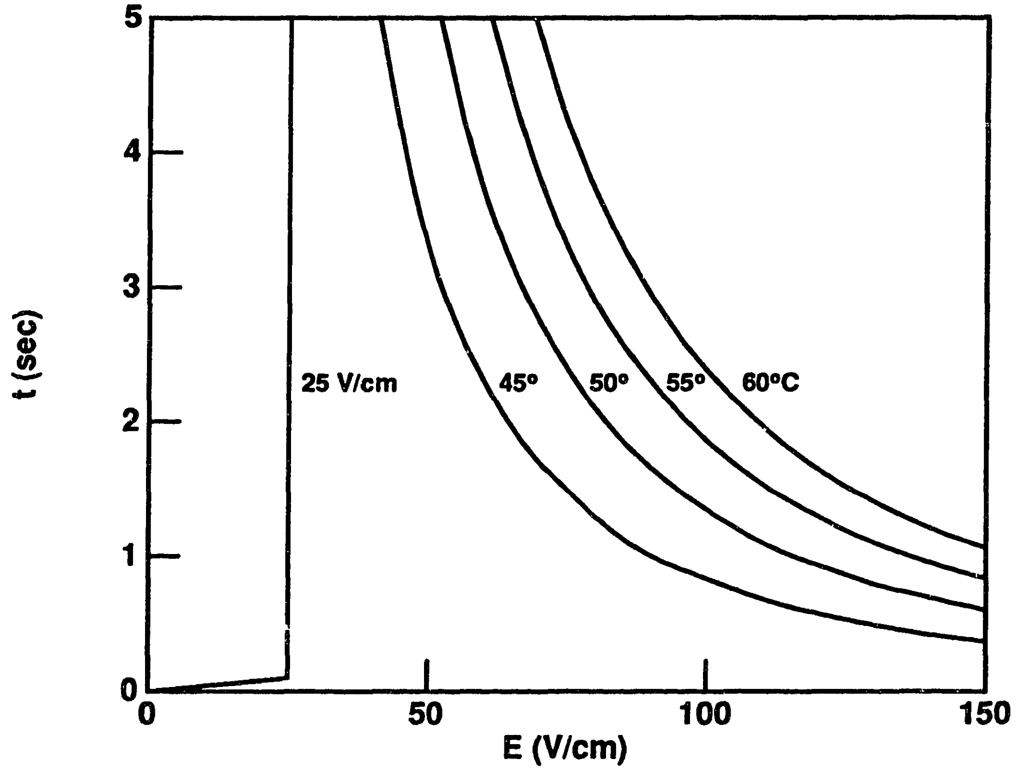

Figure 5.1: Electric field strength and contact duration required for cellular damage by thermal and electrical mechanisms. Membrane electrical breakdown will occur for fields above 25 V/cm for any realistic contact duration. For large fields or long contact durations, thermally-mediated damage will mask this effect, as indicated by the temperature curves. Thus, membrane electrical breakdown is important at low field strengths and short contact durations.

forearm and the proximal–elbow just reach 45°C, and therefore may be susceptible to thermal damage to the contractile mechanism. The mid–arm is not expected to experience thermally–mediated damage in this case. Of course, many accidents involve contact voltages and/or durations greater than those used in this example; and it is expected that in these cases, more tissues will experience thermally–mediated damage.

The importance of the duration of contact is illustrated in Figure 5.3. The electric field in the tissue as a function of the position along the arm is plotted for a 10 amp contact. Horizontal lines mark the minimum field required for heating from 37°C to 45°C during the indicated contact duration. As shown, for a 2.0 second contact, essentially the entire arm will reach temperatures of 45° and above. However, for a 1.0 second contact, only the distal–forearm and the elbow region will reach temperatures of this magnitude. For a 0.5 second contact, only a small section of the distal–forearm will heat to just over 45°C, and no significant amount of thermally–mediated damage can be expected. However, all tissues in the arm will experience electric fields large enough to lead to membrane electrical breakdown. Thus, contact with high–voltage powerlines can lead to predominantly non–thermal injuries if the duration of contact is short enough.

Figure 5.4 again illustrates the electric field induced in tissues of the arm during a 10 amp exposure. This time, the minimum fields required to raise the temperature from 37°C to 45°C, 50°C, and 55°C in one second are marked. During this exposure only a portion of the distal–forearm reaches temperatures as high as 50°C. Only the distal–forearm and the elbow region reach temperatures above 45°C. Yet the electric field strengths in the entire arm are capable of causing significant membrane electrical breakdown. In 1 second, 120 field "pulses" will be applied. This plot graphically illustrates the pattern of damage to be expected in a typical electrical injury. At the distal–forearm, heat damage will occur consisting of membrane permeabilization and destruction of the contractile mechanisms. Farther up the arm and in the elbow

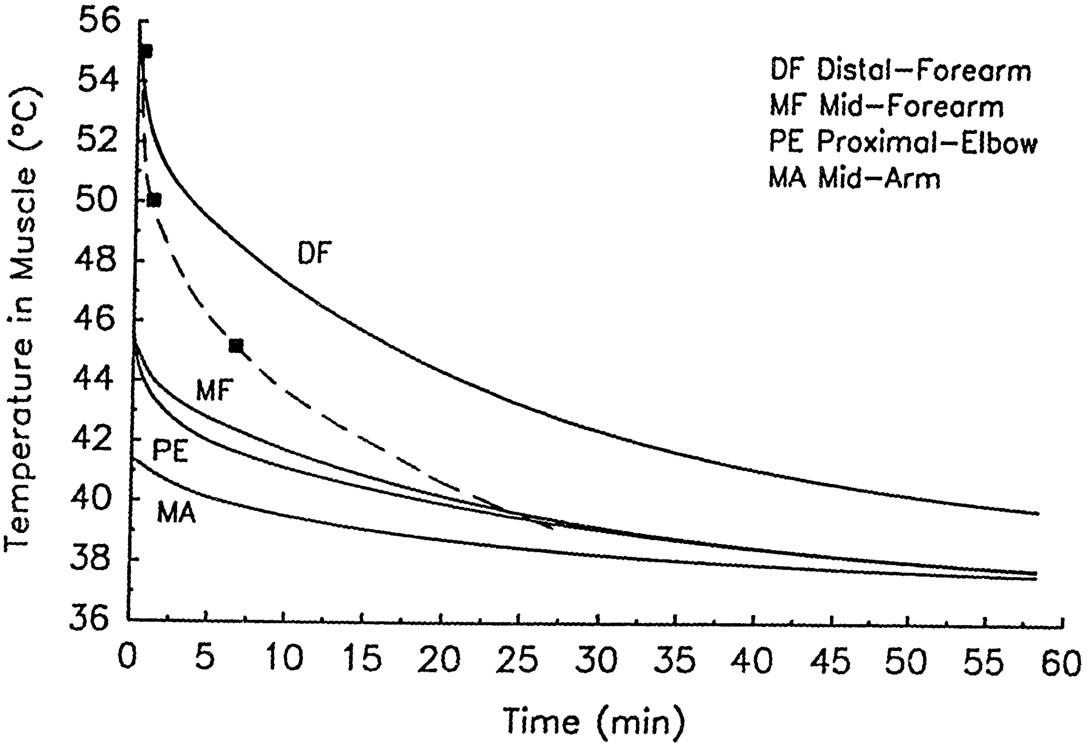

Figure 5.2: Thermal response of muscle regions in the human arm to 10 amps for 1 second (adapted from Tropea, 1989). The time–temperature thresholds for the onset of increased membrane permeability are denoted by squares. The dashed line is the Arrhenius fit of the data (see Figure 4.12). Only the cells in the distal-forearm can be expected to experience increased membrane permeability due to heating. The cells in the mid-forearm and in the proximal-elbow may experience thermally-mediated damage to the contractile mechanism. No thermal damage can be expected in the mid-arm.

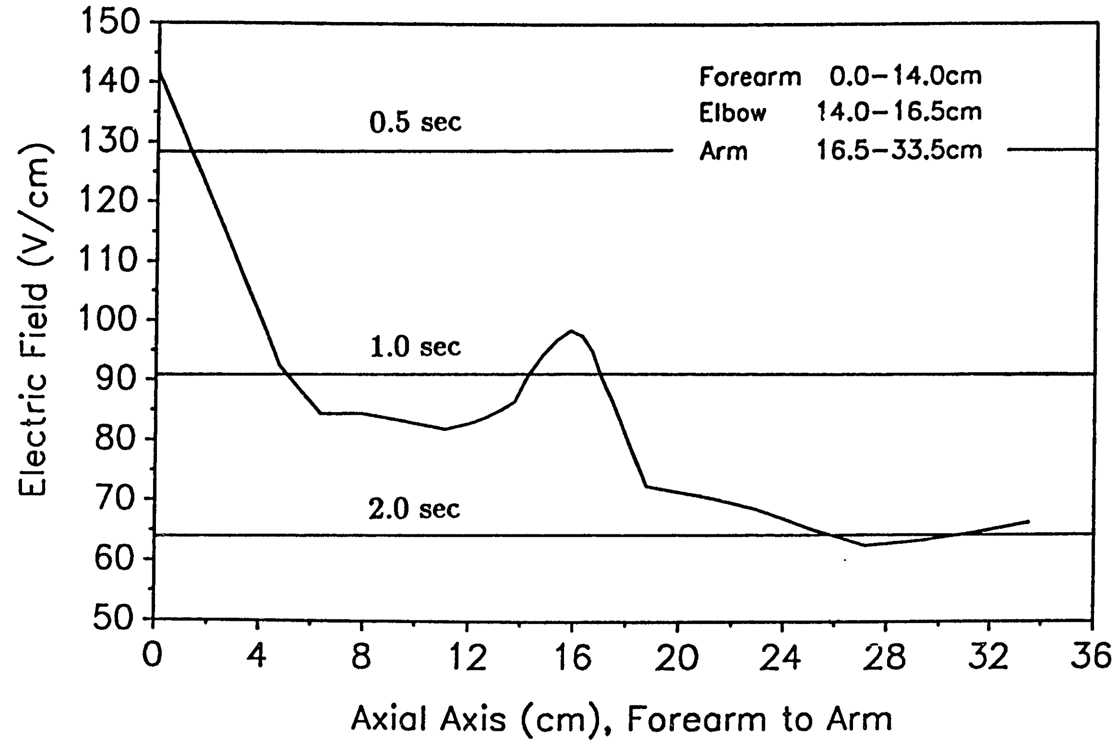

Figure 5.3: Tissue damage as a function of contact duration for a 10 amp current flow in the human arm (adapted from Tropea, 1989). The horizontal lines indicate the minimun electric field strength required for the tissue to reach 45°C in the indicated time. For a 0.5 sec contact, only a small portion of the distal–forearm will reach this temperature. For a 1.0 sec contact, the distal–forearm and the elbow region will reach this temperature. For a 2.0 sec contact, essentially the entire arm will reach temperatures of 45°C and above. However, at the field strengths indicated, all muscle tissues in the arm are suceptible to membrane electrical breakdown. This illustrates the importance of contact duration on the relevant mechanism of damage.

region, no thermally–mediated membrane permeabilization will occur, but thermal damage to the contractile mechanism is possible. Throughout the arm, membrane electrical breakdown is expected to occur, but this will be masked in the regions experiencing thermal damage. Only by considering the effects of the thermal and electrical mechanisms combined can the large myoglobin release (Baxter, 1970) and the arachidonic acid production due to increased intracellular calcium (Robson et al., 1984) observed clinically be explained.

It is important to note that only skeletal muscle cells are susceptible to membrane electrical breakdown in typical cases of electrical injury. Much higher field strengths are required to damage other cells types with much smaller dimensions. For example, fields on the order of kilovolts/cm are required for red blood cell hemolysis (Kinosita & Tsong, 1977). This may be part of the reason that skeletal muscle is particularly susceptible to damage in electrical injury.

The occurrence of membrane electrical breakdown may explain the clinically–observed "progressive" necrosis of muscle tissues. Damage caused by this mechanism may be initially unrecognized since the tissues will not appear to be burned. The chemical imbalances in the cytoplasm which result from the electropermeabilization may lead to a slower rate of cell death than that caused by protein denaturation and other thermal effects, particularly if the permeabilization is reversed following the exposure. By recognizing this, appropriate therapeutic treatments may help salvage tissues which are currently lost.

In summary, this thesis has demonstrated that electrical injury is more complicated than was previously thought. As shown, heating of tissues cannot account for all of the damage observed clinically in typical cases. The patterns of damage that occur can only be explained when the two mechanisms of Joule heating and membrane electrical breakdown are considered.

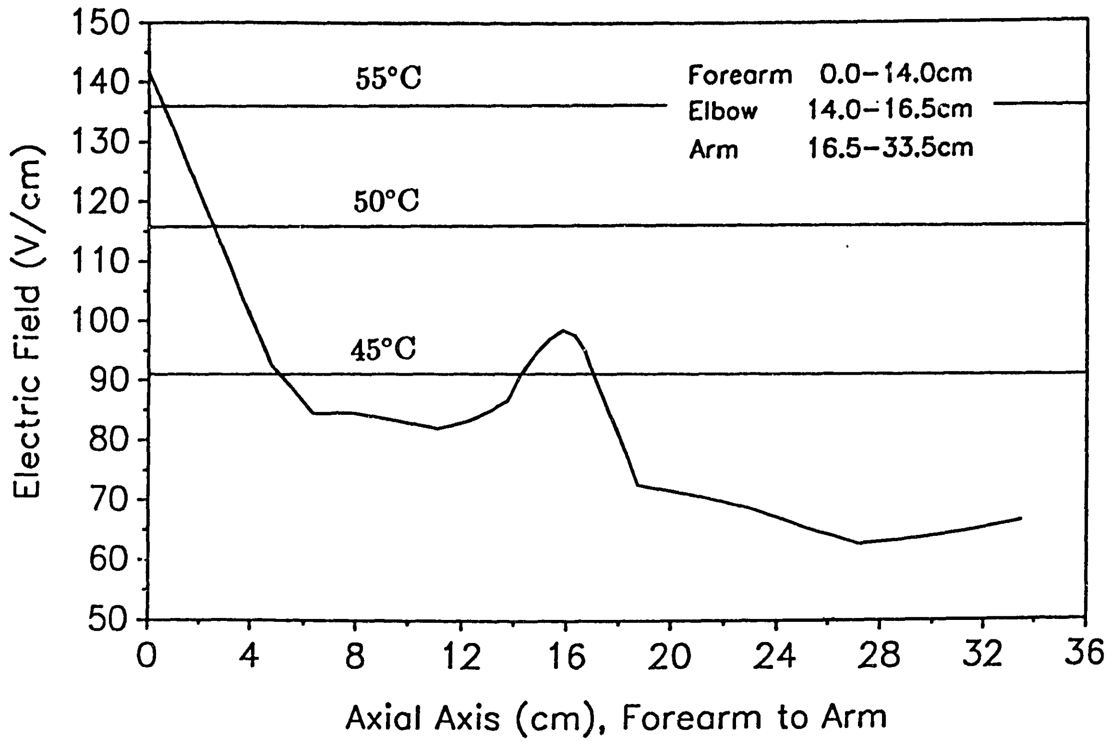

Figure 5.4: Temperature distribution in the human arm due to a 10 amp current flow for 1 second (adapted from Tropea, 1989). As indicated, the distal-forearm and elbow region reach a temperature of at least 45°, and are thus susceptible to thermal injury of the contractile mechanism. Only a small portion of the distal-forearm reaches temperatures of 50-55°C leading to thermally-induced increased membrane permeability. However, at the field strengths indicated, all muscle tissues are susceptible to membrane electrical breakdown. This illustrates how damage of different causes can be scattered along the current path.

Bibliography

I. G. Abidor, V. B. Arakelyan, L. V. Chernomordik, Yu. A. Chizmadzhev, V. F. Pastushenko, and M. R. Tarasevich. Electric breakdown of bilayer lipid membranes I: The main experimental facts and their qualitative discussion. *Bioelectrochem. Bioenerget.*, 6:37–52, 1979.

R. H. Adrian. Electrical properties of striated muscle. In *Handbook of Physiology, Section 10: Skeletal Muscle*, pages 275–300, American Physiological Society, Bethesda, Maryland, 1983.

C. P. Artz. Changing concepts in electrical injury. *Am. J. Surg.*, 128:600–602, 1974.

D. B. Askey. *Automated Image Acquisition and Analysis of the Photobleaching Response.* Bachelor's Thesis, Massachusetts Institute of Technology, 1987.

C. R. Baxter. Present concepts in the management of major electrical injury. *Surg. Clin. North Amer.*, 50:1401–1418, 1970.

A. Bekoff and W. J. Betz. Physiological properties of dissociated muscle fibers obtained from innervate and denervated adult rat muscle. *J. Physiol.*, 271:25–40, 1977.

A. Bekoff and W. J. Betz. Properties of isolated adult rat muscle fibres maintained in tissue culture. *J. Physiol.*, 271:537–547, 1977.

R. Benz, F. Beckers, and U. Zimmerman. Reversible electrical breakdown of lipid bilayer membranes: A charge–pulse relaxation study. *J. Membrane Biol.*, 48:181–204, 1979.

R. Benz and U. Zimmerman. Pulse–length dependence of the electrical breakdown in lipid bilayer membranes. *Biochim. Biophys. Acta*, 597:637–642, 1980.

R. Benz and U. Zimmerman. Relaxation studies on cell membranes and lipid bilayers in the high electric field range. *Bioelectrochem. and Bioenerg.*, 7:723–739, 1980.

D. L. Bhatt. 1988. private communication.

D. L. Bhatt, D. C. Gaylor, and R. C. Lee. Rhabdomyolysis due to pulsed electric fields. *Plast. Recontr. Surg.*, 1990. (to be published).

R. Bischoff. Proliferation of muscle satellie cells on intact myofibers in culture. *Developmental Biol.*, 115:129–139, 1986.

W. Bloom and D. W. Fawcett. *A Textbook of Histology.* W. B. Saunders Company, Philadelphia, 1975.

M. S. Bretscher. *The Molecules of the Cell Membrane*, chapter 5, pages 50–58. W.H. Freeman and Company, New York, 1985.

C. Caputo. Pharmacological investigations of excitation–contraction coupling. In *Handbook of Physiology, Section 10: Skeletal Muscle*, pages 381–415, American Physiological Society, Bethesda, Maryland, 1983.

M. Chilbert, D. Maiman, A. Scances Jr., J. Myklebust, T. E. Prieto, T. Swionek, M. Heckman, and K. Pintar. Measure of tissue resistivity in experimental electrical burns. *J. Trauma*, 25:209–215, 1985.

Yu. A. Chizmadzhev, V. B. Arakelyan, and V. F. Pastushenko. Electric breakdown of bilayer lipid membranes III: Analysis of possible mechanisms of defect origination. *Bioelectrochem. Bioenerget.*, 6:63–70, 1979.

M. S. Cooper. Electrical cable theory, transmembrane ion fluxes, and the motile responses of tissue cells to external electrical fields. In *Bioelectric Interactions Symp. IEEE / Engineering in Medicine and Biology Society, 7th Annual Conference*, Chicago, September 1986.

M. S. Cooper. Gap junctions increase the sensitivity of tissue cells to exogenous electric fields. *J. theor. Biol.*, 111:123–130, 1984.

M. D. Cosman. *Effect of Cooling Rate and Supercooling on the Formation of Ice in a Cell Population.* PhD thesis, Massachusetts Institute of Technology, 1983.

M. D. Cosman, M. Toner, J. Kandel, and E. G. Cravalho. An integrated cryomicroscopy system. *Cryo-Letters*, 10:17–38, 1989.

R. R. Cowden. Fluorescent cytochemistry of living cells. *Amer. Biol. Lab.*, 3:8–15, 1985.

J. M. Crowley. Electrical breakdown of bimolecular lipid membranes as an electromechanical instability. *Biophys. J.*, 13:711–724, 1973.

R. K. Daniel, P. A. Ballard, P. Heroux, R. G. Zelt, and C. R. Howard. High-voltage electrical injury: Acute pathophysiology. *J. Hand Surg.*, 13A:44–49, 1988.

C. L. Davey and R. J. Winger. *The structure of skeletal muscle and meat toughness*, pages 97–132. Academic Press, London, 1979.

R. DeBiasio, G. R. Bright, L. A. Ernst, A. S. Waggoner, and D. L. Taylor. Five–parameter fluorescence imaging: Wound healing of living Swiss 3T3 cells. *J. Cell Biol.*, 105:1613–1622, 1987.

D. S. Dimitrov. Electric field–induced breakdown of lipid bilayers and cell membranes: A thin viscoelastic film model. *J. Membrane Biol.*, 78:53–60, 1984.

A. Dulhunty, G. Carter, and C. Hinrichsen. The membrane capacitance of mammalian skeletal muscle fibers. *J. Muscle Research and Cell Motility*, 5:315–332, 1984.

R. S. Eisenberg. Impedance measurements of the electrical structure of skeletal muscle. In *Handbook of Physiology, Section 10: Skeletal Muscle*, pages 301–323, American Physiological Society, Bethesda, Maryland, 1983.

E. A. Evans and R. Skalak. *Mechanics and Thermodynamics of Biomembranes.* CRC Press, Boca Raton, Florida, 1980.

D. C. Gaylor, K. Prakah–Asante, and R. C. Lee. Significance of cell size and tissue structure in electrical trauma. *J. theor. Biol.*, 133:223–237, 1988.

N. L. Gershfeld and M. Murayama. Thermal instability of red blood cell membrane bilayers: Temperature dependence of hemolysis. *J. Membrane Biol.*, 101:67–72, 1988.

D. Gross and L. L. Loew. *Fluorescent indicators of membrane potential: Microspectrofluorometry and imaging*, chapter 7, pages 193–218. Volume 30, Academic Press, San Diego, 1989.

E. J. Harris. *Transport and Accumulation in Biological Systems.* Butterworths, London, 1972.

R. P. Haugland. *Molecular Probes: Handbook of Fluorescent Probes and Research Chemicals.* Molecular Probes, Inc., Eugene, OR, 1989.

F. C. Henriques. Studies of thermal injury V. The predictability and the significance of thermally induced rate processes leading to irreversible epidermal injury. *Arch. Pathol.*, 43:489–502, 1947.

J. V. Howarth. The behavior of frog muscle in hypertonic solutions. *J. Physiol.*, 144:167–175, 1958.

J. L. Hunt, R. M. Sato, and C. R. Baxter. Acute electric burns: Current diagnostic and therapeutic approaches to management. *Arch. Surg.*, 115:434–438, 1980.

D. Israel. 1988. private communication.

J. J. B. Jack, D. Noble, and R. W. Tsien. *Electric Current Flow in Excitable Cells.* Oxford University Press, London, 1975.

P. C. Jordan. Electrostatic modeling of ion pores: Energy barriers and electric field profiles. *Biophys. J.*, 39:157–164, 1982.

K. Kinosita Jr., I. Ashikawa, N. Saita, H. Yoshimura, H. Itoh, K. Nagayama, and A. Ikegami. Electroporation of cell membrane visualized under a pulsed–laser fluorescence microscope. *Biophys. J.*, 53:1015–1019, 1988.

K. Kinosita Jr. and T. Y. Tsong. Hemolysis of human erythrocytes by a transient field. *Proc. Natl. Acad. Sci.*, 74:1923–1927, 1977.

K. Kinosita Jr. and T. Y. Tsong. Voltage–induced pore formation and hemolysis of human erythrocytes. *Biochim. Biophys. Acta*, 471:227–242, 1977.

T. Kiyohara and M. Sato. Membrane constants of red and white muscle fibers in the rat. *Jap. J. Physiol.*, 17:720–725, 1967.

K. Laki, editor. *Contractile Proteins and Muscle.* Marcel Dekker, Inc., New York, 1971.

S. Lapanje. *Physiochemical Aspects of Protein Denaturation.* John Wiley & Sons, New York, 1978.

R. C. Lee and M. S. Kolodney. Electrical injury mechanisms: Electrical breakdown of cell membranes. *Plast. Reconstr. Surg.*, 80:672–679, 1987.

D. G. Levitt. Strong electrolyte continuum theory solution for equilibrium profiles, diffusion limitation, and conductance in charged ion channels. *Biophys. J.*, 48:19–31, 1985.

J. D. Litster. Stability of lipid bilayers and red blood cell membranes. *Physics Letters*, 53A:193–194, 1975.

C. Maldarelli and R. K. Jain. The linear, hydrodynamic stability of an interfacially perturbed, transversely isotropic, thin, planar viscoelastic film I: General formulation and a derivation of the dispersion equation. *J. Colloid and Interface Sci.*, 90:233–262, 1982.

C. Maldarelli and R. K. Jain. The linear, hydrodynamic stability of an interfacially perturbed, transversely isotropic, thin, planar viscoelastic film II: Extension of the theory to the study of the onset of small–scale cell membrane motions. *J. Colloid and Interface Sci.*, 90:263–276, 1982.

C. Maldarelli, R. K. Jain, I. B. Ivanov, and E. Ruckenstein. Stability of symmetric and unsymmetric thin liquid films to short and long wavelength perturbations. *J. Colloid and Interface Sci.*, 78:118–143, 1980.

H. G. Mannherz and K. C. Holmes. *Biomechanics*, chapter 14, pages 566–640. Springer–Verlag, Berlin, 1982.

A. M. Mastro, M. A. Babich, W. D. Taylor, and A. D. Keith. Diffusion of a small molecule in the cytoplasm of mammalian cells. *Proc. Natl. Acad. Sci.*, 81:3414–3418, 1984.

D. H. Michael and M. E. O'Neill. The breakdown of electrical insulation in a plane layer of insulating fluid by electrocapillary instability. *J. Fluid Mech. pt. 3*, 47:609–623, 1971.

R. L. Milton, R. T. Mathias, and R. S. Eisenberg. Electrical properties of the myotendon region of frog twitch muscle fibers measured in the frequency domain. *Biophys. J.*, 48:253–267, 1985.

G. Mixter Jr., G. P. Delhery, W. L. Derksen, and T. I. Monahan. The influence of time on the death of HeLa cells at elevated temperature. In J. D. Hardy, editor, *Temperature: Its Measurement and Control in Science and Industry*, Reinhold, 1963.

A. R. Moritz and F. C. Henriques. Studies of thermal injury II. The relative importance of time and surface temperature in the causation of cutaneous burns. *Am. J. Path.*, 23:695–720, 1947.

N. A. Moussa, J. J. McGrath, E. G. Cravalho, and P. J. Asimacopoulos. Kinetics of thermal injury in cells. *ASME J. Biomech. Engr.*, 99:155–159, 1977.

N. A. Moussa, E. N. Tell, and E. G. Cravalho. Time progression of hemolysis of erythrocyte populations exposed to supraphysiological temperatures. *ASME J. Biomech. Engr.*, 101:213–217, 1979.

L. Parker and P. H. Zhu. Effects of hypertonic solutions on calcium transients in frog twitch muscle fibres. *J. Physiol.*, 383:615–627, 1987.

K. T. Powell and J. C. Weaver. Transient aqueous pores in bilayer membranes: A statistical theory. *Bioelectrochem. Bioenerget.*, 15:211–227, 1986.

R. E. Powell, W. E. Roseveare, and H. Eyring. Diffusion, thermal conductivity and viscous flow of liquids. *Ind. Engnr. Chem.*, 33:430–435, 1941.

K. Prakah–Asante. *A Continuum Model of the Conductivity and Imposed Transmembrane Potential of Biological Membranes.* S.M. Thesis, Massachusetts Institute of Technology, 1989.

J. B. Ranck. Analysis of specific impedance of rabbit cerebral cortex. *Experimental Neurology*, 7:153–174, 1963.

M. C. Robson, R. C. Murphy, and J. P. Heggers. A new explanation for the progressive tissue loss in electrical injuries. *Plast. Reconstr. Surg.*, 73:431–437, 1984.

A. Sances Jr., J. B. Mykelbust, S. J. Larson, J. C. Darin, T. Swiotek, T. Prieto, M. Chilbert, and J. F. Cusick. Experimental electrical injury studies. *J. Trauma*, 21:589–597, 1981.

A. Sances Jr., J. B. Mykelbust, J. F. Szablya, T. J. Swiontek, S. J. Larson, M. Chilbert, T. Prieto, J. F. Cusick, D. J. Maiman, and K. Pintar. Current pathways in high–voltage injuries. *IEEE Trans. Biomed. Engr.*, 30:118–124, 1983.

A. Sanfeld, A. Steinchen, M. Henneberg, P. M. Bisch, D. Van Lamsweerd–Gallez, and W. Dalle–Vedove. Mechanical, chemical, and electrical constraints and hydrodynamic interfacial instability. In T.S. Sorensen, editor, *Dynamics and Instability of Fluid Interfaces*, pages 168–204, Springer–Verlag, New York, 1979.

O. F. Schanne and E. Ruiz P.–Ceretti. *Impedance Measurements in Biological Cells.* John Wiley & Sons, New York, 1978.

M. Shinitzky, editor. *Physiology of Membrane Fluidity.* CRC Press, Boca Raton, Florida, 1984.

S. J. Singer and G. L. Nicolson. The fluid mosaic model of the structure of cell membranes. *Science*, 175:720–731, 1972.

A. Steinchen, D. Gallez, and A. Sanfeld. A viscoelastic approach to the hydrodynamic stability of membranes. *J. Colloid and Interface Sci.*, 85:5–15, 1982.

O. Sten-Knudsen. Is muscle contraction initiated by internal current flow? *J. Physiol.*, 151:363–384, 1960.

I. P. Sugar and E. Neumann. Stochastic model for electric field–induced membrane pores: Electroporation. *Biophysical Chemistry*, 19:211–225, 1984.

P. Taborek, R. N. Kleiman, and D. J. Bishop. Power–law behavior in the viscosity of supercooled liquids. *Phys. Rev. B*, 34:1835–1840, 1986.

G. I. Taylor and D. H. Michael. On making holes in a sheet of fluid. *J. Fluid Mech. pt. 4*, 58:625–639, 1973.

J. Teissie and T. Y. Tsong. Evidence of voltage–induced channel opening in Na/K ATPase of human erythrocyte membrane. *J. Membrane Biol.*, 55:133–140, 1980.

Y. Tonomura. *Muscle Proteins, Muscle Contraction, and Cation Transport.* University Park Press, Baltimore, 1973.

B. I. Tropea. 1989. manuscript in prepartion.

B. I. Tropea. *A numerical model for determining the human forearm thermal response to high voltage injury.* S.B. Thesis, Massachusetts Institute of Technology, 1987.

R. C. Weast, editor. *Handbook of Chemistry and Physics.* The Chemical Rubber Company, Cleveland, OH, 51 edition, 1971.

J. C. Weaver and R. A. Mintzer. Decreased bilayer stability due to transmembrane potentials. *Physics Letters*, 86A:57–59, 1981.

J. C. Weaver, K. T. Powell, R. A. Mintzer, H. Ling, and S. R. Sloan. The electrical capacitance of bilayer membranes: The contribution of transient aqueous pores. *Bioelectrochem. Bioenerget.*, 12:393–404, 1984.

J. C. Weaver, K. T. Powell, R. A. Mintzer, S. R. Sloan, and H. Ling. The diffusive permeability of bilayer membranes: The contribution of transient aqueous pores. *Bioelectrochem. Bioenerget.*, 12:405–412, 1984.

R. G. Zelt, P. A. Ballard, P. Heroux, and R. K. Daniel. Experimental high voltage electrical burns: The role of progressive necrosis. *Proc. 55th Ann. Scientific Meeting Am. Soc. Plast. Reconstr. Surg.*, 9:222, 1986.

E. Zheng, S. Shao, and J. G. Webster. Impedance of skeletal muscle from 1 Hz to 1 MHz. *IEEE Trans. Biomedical Engineering*, 31:477–481, 1984.

U. Zimmerman. Electrical breakdown: Electropermeabilization & electrofusion. *Rev. Physiol. Biochem. Pharmacol.*, 105:176–256, 1986.

U. Zimmerman, P. Scheurich, G. Pilwat, and R. Benz. Cells with manipulated functions: New perspectives for cell biology, medicine, and technology. *Angew. Chem. Int. Ed. Engl.*, 20:325–344, 1981.

U. Zimmerman, J. Vienken, and G. Pilwat. Development of drug carrier systems: Electrical field induced effects in cell membranes. *Bioelectrochem. Bioenerget.*, 7:553–574, 1980.